GRAPHENE BASED FLEXIBLE HALL SENSORS

A THESIS SUBMITTED TO
THE GRADUATE SCHOOL OF NATURAL AND APPLIED SCIENCES
OF
MIDDLE EAST TECHNICAL UNIVERSITY

BY

UĞUR YİĞİT İNKAYA

IN PARTIAL FULFILLMENT OF THE REQUIREMENTS
FOR
THE DEGREE OF DOCTOR OF PHILOSOPHY
IN
PHYSICS

SEPTEMBER 2021

Approval of the thesis:

GRAPHENE BASED FLEXIBLE HALL SENSORS

submitted by **UĞUR YİĞİT İNKAYA** in partial fulfillment of the requirements for the degree of **Doctor of Philosophy in Physics, Middle East Technical University** by,

Prof. Dr. Halil Kalıpçılar
Dean, Graduate School of **Natural and Applied Sciences** _____

Prof. Dr. Seçkin Kürkcüoğlu
Head of the Department, **Physics** _____

Prof. Dr. Ahmet Oral
Supervisor, **Physics, METU** _____

Examining Committee Members:

Prof. Dr. Tofig Memmedli
Electrical and Electronics Engineering, Ardahan University _____

Prof. Dr. Ahmet Oral
Physics, METU _____

Prof. Dr. Coşkun Kocabaş
Materials, The University of Manchester _____

Assoc. Prof. Dr. Alpan Bek
Physics, METU _____

Assoc. Prof. Dr. Emre Yüce
Physics, METU _____

Date: 09.09.2021

I hereby declare that all information in this document has been obtained and presented in accordance with academic rules and ethical conduct. I also declare that, as required by these rules and conduct, I have fully cited and referenced all material and results that are not original to this work.

Name, Last name: Uğur Yiğit İnkaya

Signature:

ABSTRACT

GRAPHENE BASED FLEXIBLE HALL SENSORS

İnkaya, Uğur Yiğit
Doctor of Philosophy, Physics
Supervisor: Prof. Dr. Ahmet Oral

September 2021, 97 pages

Graphene is a two-dimensional material that has electronic properties such as having low density of charge carriers with high mobility, which are ideal for fabricating Hall sensors. Also considering its elastic properties, it is a promising material for flexible electronics including flexible Hall sensorics.

Graphene was synthesized via atmospheric pressure chemical vapor deposition (CVD) on 20μm-thick copper by using methane as carbon feedstock. CVD-graphene was transferred onto EVA-coated PET film via lamination. By using the resultant graphene/EVA/PET laminate, we manufactured Hall devices. We characterized the devices by measuring their Hall sensitivity. The devices showed mostly linear sensor response with sensitivity of up to 1200 Ω/T. Also we studied graphene-based multilayered conductive films on EVA/PET by using Hall devices for the electronic characterization. The films were made via layer-by-layer transfer-printing graphene onto EVA/PET. Further characterization was performed by van der Pauw measurements. It revealed mobilities around 1000 $cm^2/(Vs)$ and the hole density increasing almost linearly with the number of laminations performed to make the film. The surface topography of the films were studied via atomic force microscopy.

Finally we performed Joule heating experiments that showed the surface temperature of the film can be increased up to ~100°C.

Keywords: Hall sensor, Graphene, Chemical Vapor Deposition, Flexible Substrate

ÖZ

GRAFEN TEMELLİ ESNEK HALL SENSÖRLERİ

İnkaya, Uğur Yiğit
Doktora, Fizik
Tez Yöneticisi: Prof. Dr. Ahmet Oral

Eylül 2021, 97 sayfa

Grafen, düşük yoğunluklu ve yüksek mobiliteli yük taşıyıcılarına sahip olmak gibi, Hall sensör üretimi için ideal özellikleri olan iki boyutlu bir malzemedir. Ayrıca elastik özellikleri dikkate alınırsa, esnek Hall sensöriği dahil olmak üzere, esnek elektronik için umut vadeden bir malzemedir.

Grafen, 20 μm kalınlığındaki bakır üzerinde, atmosferik basınçlı kimyasal buhar biriktirme (KBB) yoluyla, karbon kaynağı olarak metan kullanılıp sentezlendi. KBB grafen, EVA kaplı PET filmin üzerine laminasyon yoluyla aktarıldı. Sonuçtaki grafen/EVA/PET laminantını kullanarak Hall cihazları imal ettik. Cihazları, onların Hall duyarlılıklarını ölçerek karakterize ettik. Cihazlar çoğunlukla, duyarlılığı 1200 Ω/T'ya varabilen, lineer sensör tepkisi gösterdi. Ayrıca, elektronik karakterizasyon için Hall aygıtlarını kullanarak, EVA/PET üzerinde grafen bazlı çok katmanlı iletken filmleri inceledik. Filmler, grafenin EVA/PET üzerine tabaka tabaka aktarılması yoluyla yapıldı. İleri karakterizasyon van der Pauw ölçümleri ile icra edildi. Ölçümler, 1000 $cm^2/(Vs)$ civarında mobiliteler ve filmi üretmek için yapılan laminasyon sayısıyla neredeyse lineer artan deşik yoğunluklarını açığa çıkardı. Filmlerin yüzey topografisi atomik kuvvet mikroskobu ile incelendi. Son olarak,

filmlerin yüzey sıcaklıklarının 100°C'ye kadar çıkarılabileceğini gösteren, Joule ısınması deneyleri icra ettik.

Anahtar Kelimeler: Hall sensörü, Grafen, Kimyasal Buhar Biriktirme, Esnek Alttaş

To my family

ACKNOWLEDGMENTS

First, I would like to express my deepest gratitude to my thesis supervisor Prof. Dr. Ahmet Oral for his support and mentorship throughout my PhD work. Working in his lab was a challenging but fruitful experience for me. I was inspired very much by his perspective and way of thinking in applied physics, which made me change my mentality and adopt a more experiment-based scientific attitude. Many times, his viewpoint and suggestions helped me overcome the problems I encountered during the development of this thesis. He taught me the importance of attacking problems without worrying or hesitation. I feel very lucky to have worked with such a research-minded and inspiring advisor. I believe that I have become a much better researcher thanks to him.

I would like to thank my thesis advisory committee members Prof. Dr. Coşkun Kocabaş and Assoc. Prof. Dr. Alpan Bek for their inspiring questions and suggestions, which helped me develop this thesis. I must also add that I owe Dr. Bek a great debt of gratitude for his help at many critical points.

I would also like to thank Prof. Dr. Coşkun Kocabaş, Assoc. Prof. Dr. Alpan Bek, Assoc. Prof. Dr. Emre Yüce and Prof. Dr. Tofig Memmedli for being on my thesis jury. I am especially grateful to Dr. Memmedli for his support and encouragement. I benefitted a lot from the discussions with him on applied physics. Working with him in the lab showed me the importance of having technical skills.

I am indebted to Dr. Shumaila Karamat for sharing her knowledge and experience on CVD with me, Ekin Özgönül for his friendship and help in technical issues, and Yiğit Uysallı for suggesting me to use permanent marker ink as an etch resist. I am also indebted to the staff of NanoMagnetics Instruments Ltd.

TABLE OF CONTENTS

LIST OF TABLES

TABLES

LIST OF FIGURES

FIGURES

CHAPTER 1

INTRODUCTION

1.1 Motivation and Scope

Graphene is a two-dimensional crystal of sp^2-bonded carbon atoms. First experimentally studied by Novoselov *et al.* [1], it has extraordinary properties. Its band structure allows for the reduction of the density of its charge carriers indefinitely small values through field effect. In addition, its charge carriers have mobilities ~10,000 $cm^2/(Vs)$ in ambient conditions. Therefore, graphene is a perfect material for fabricating extremely sensitive Hall sensors [2].

Hall sensors are Hall devices applied as magnetic sensors. Their principle of operation is based on the Hall effect [2]. Although there are materials such as III-V semiconductors used to fabricate highly sensitive Hall sensors [2], they are not compatible with flexible electronics. However, the mechanical properties of graphene [3] indicate a promise for graphene-based flexible electronics.

This thesis aims to study graphene-based conductive films on flexible substrates by manufacturing devices and to explore the performance of graphene on flexible substrates in Hall devices.

1.2 Outline

Chapter 1 explains our motivation behind this work by relating the properties of graphene with our aim.

Chapter 2 gives a brief account of the Hall effect and its applications and presents practical issues about the Hall devices.

Chapter 3 contains general information about graphene, its methods of production, transfer, characterization, and our graphene synthesis and characterization process.

Chapter 4 presents our manufacture process of graphene-based Hall sensors on flexible polymeric film and their electronic characterization.

Chapter 5 presents our manufacture process for obtaining graphene-based multilayered conducting films on flexible polymeric foil, their electronic and structural characterization, and their application as heaters.

Chapter 6 provides a conclusion and perspective for possible future work.

CHAPTER 2

HALL SENSORS

Hall sensors are electronic transducers that linearly converts magnetic flux density as input into voltage signal. They are magnetic field sensing devices whose principle of operation is based upon the Hall effect.

Although the Hall effect was discovered in 1879, the application of Hall devices as magnetic sensors became feasible only when suitable semiconductor materials were produces in 1950s [2,4]. With the advent of integrated circuits and microelectronics, their production cost was greatly reduced, thereby making them one of the most commonly-used magnetic sensors from computer keyboards to industrial automation [4].

Hall sensors are mainly used for measuring electric current and detecting motion [2]. They enable contactless current measurement and facilitate the integration of control circuitries into systems such as brushless DC electric motors and anti-lock braking systems (ABS) [4]. They are also used as probes for high-resolution magnetic imaging of magnetic storage media [5].

This chapter presents a brief account of the operation principle of Hall devices and their application as magnetic sensors.

2.1 The Hall effect

The Hall effect is observed when a current-carrying plate is exposed throughout to magnetic field. It was discovered in 1879 by Edwin Herbert Hall in testing conflicting ideas about the physics of electrical current in relation to the current-

carrying material and magnetic force: Questioning the hypothesis in Maxwell's Electricity and Magnetism that the mechanical force exerted upon a conductor carrying a current across the magnetic field lines acts upon the conductor, not the current carried by it, he read an article by Erik Edlund, not excluding the possibility of a magnetic action upon the current [6]. Having already realized similarity between the explanation for the interaction of electrically charged bodies and that of current-carrying wires, and contradiction between the Maxwell's statement and the fact that the force exerted upon a current-carrying by a magnet is exactly proportional to the current, the Edlund's article encouraged him to attack the problem [6]. After performing some inconclusive experiments by using a flat spiral of silver wire and a disk of metal with a considerable thickness, Hall decided to perform experiments by using a gold leaf fixed on a glass plate (Figure 2.1). These experiments yielded the observation of the effect named after him [6].

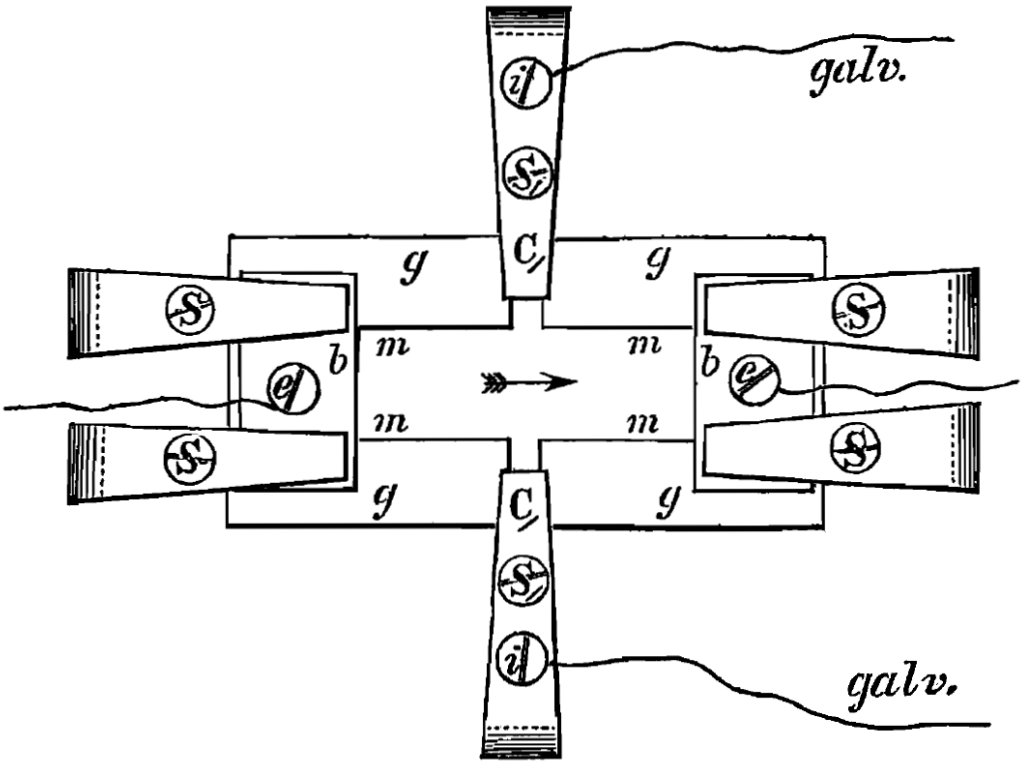

Figure 2.1. Schematic depiction of Hall's original setup [7]. A strip of gold leaf fixed onto a plate of glass. The gold leaf and the glass plate are represented by the letters ***m*** and ***g***, respectively. ***b*** denotes the two slabs of brass in contact with the strip to drive a current through the metal in the direction denoted by an arrow. The screws used for maintaining the electrical contact between the leaf and the slabs are represented by ***S***. ***e*** denotes the screws through which the current was introduced into the strip. There are two projections protruding from the middle of the strip. The projections are in contact with the metal clamps by means of the screws denoted by ***S/***. ***C/*** represents the clamps. Electrical connection to the Thomson galvanometer is supported by the screws represented by ***i***.

By using the setup depicted in Figure 2.1, Hall was able to observe a significant non-inductive deflection of the needle of the Thomson galvanometer connected to the gold strip by means of the screws denoted by ***i***, after applying a steady current to the metal strip through the screws denoted by ***e***, in the presence of magnetic induction [7].

Furthermore, he repeated the experiment after having reversed the current direction and for different orientations of the setup with respect to the uniform magnetic induction, thereby determining the directional dependence of the effect (Figure 2.2).

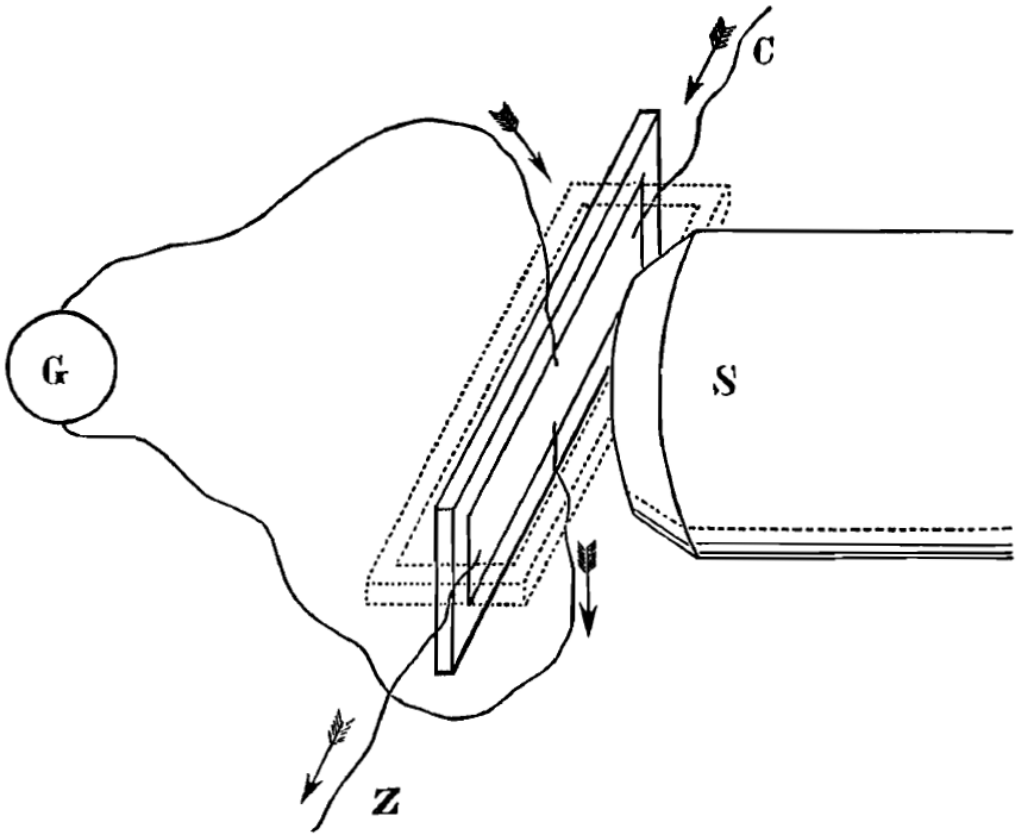

Figure 2.2. Schematic showing Hall's experimental procedure applied to explore the directional dependence of the effect [7].

Hall's meticulous research showed that uniform magnetic field perpendicular to a strip of gold leaf carrying a steady current causes a voltage difference between the projections (Figure 2.1), which had had the same potential without the presence of the magnetic field. In addition to gold, Hall repeated the experiments with silver, iron, platinum, nickel, and tin and showed that the quantity $\frac{M \times V}{E'}$ was constant for each of the metals except for nickel and tin, where M, V, and E' denote the strength

of the magnetic field, the current density, and the difference of potential per unit of length on the transverse axis of the metal strip.

All the results of these experiments can be microscopically explained by using the concept of charge carrier and the Lorentz force (Figure 2.3): the electric field $\boldsymbol{E}_\mathbf{e}$, due to the voltage difference V between the current contacts C_1 and C_2, causes the charge carriers of the conducting body to move longitudinally with the velocity $\boldsymbol{v}_\mathbf{d}$, called the drift velocity. In the presence of magnetic field **B**, the force **F** acted upon the charge carriers is given by the Lorentz force equation $\mathbf{F} = q[\boldsymbol{E}_\mathbf{e} + (\boldsymbol{v}_\mathbf{d} \times \mathbf{B})]$ with $|q| = e$, where e denotes the elementary charge. The magnetic component of the force pushes the charge carriers towards one of the edges of the strip, thereby leads to an increasing gradient of the charge carrier concentration. This gradient results in an electric field in the direction opposite to the magnetic force. This electric field exerts a force on the charge carriers, thereby decreasing the transverse component of the Lorentz force acting upon them. Since the gradient of the charge carrier concentration increases due to the magnetic force, the resultant electric force continues to increase until it balances out the magnetic force. After this transient process, a transverse electric field $\boldsymbol{E}_\mathrm{H}$, called the Hall electric field, is established, thereby resulting in a electric potential difference V_H, called the Hall voltage, between the sense contacts. Therefore, $\boldsymbol{E}_\mathbf{H} = -(\boldsymbol{v}_\mathbf{d} \times \mathbf{B})$ and $V_\mathrm{H} = \pm \int_{S_1}^{S_2} \boldsymbol{E}_\mathbf{H} \cdot d\mathbf{r}$, where the sign is determined by the direction of the current, magnetic field, and the type of the charge carrier. To obtain a more simplified explanation, one can make an approximation by assuming $\boldsymbol{v}_\mathbf{d} = v_\mathrm{d}\,\mathbf{x}$ and $\mathbf{B} = B\,\mathbf{z}$, where $v_\mathrm{d} = |\,\boldsymbol{v}_\mathbf{d}\,|$ and $B = |\mathbf{B}|$. Then $\boldsymbol{E}_\mathbf{H} = -v_\mathrm{d} B\,\mathbf{y}$ (**x**, **y**, **z** represent the unit vectors of the right-handed coordinate system). The accuracy of this approximation increases as the length-to-width ratio of the strip increases and the ratio of the contact area to the strip area decreases, and it becomes exact as the former ratio goes to infinity and the latter goes to zero [2]. Since $\boldsymbol{v}_\mathbf{d} = \mu\,\boldsymbol{E}_\mathbf{e}$, $|\boldsymbol{E}_\mathbf{H}| = \mu B\,|\boldsymbol{E}_\mathbf{e}|$, implying $|\boldsymbol{E}_\mathbf{H}| / |\boldsymbol{E}_\mathbf{e}| = \mu B$, where μ denotes the mobility of the charge carriers. Changing the total electric field in the conducting body from $\boldsymbol{E}_\mathbf{e}$ to $\boldsymbol{E}_\mathbf{e} + \boldsymbol{E}_\mathbf{H}$, the Hall effect forms the angle Θ_H between the current density **J** and the total electric field, which satisfies the equation $\tan\Theta_\mathrm{H} = |\boldsymbol{E}_\mathbf{H}| / |\boldsymbol{E}_\mathbf{e}| = \mu B \Rightarrow \Theta_\mathrm{H} = \arctan(\mu B)$, called

the Hall angle (Figure 2.4). As a result, when B is constant, the Hall angle is also constant for a specific conducting body with mobility μ and can be used to discover alternative equivalent shapes by employing the conformal mapping [2].

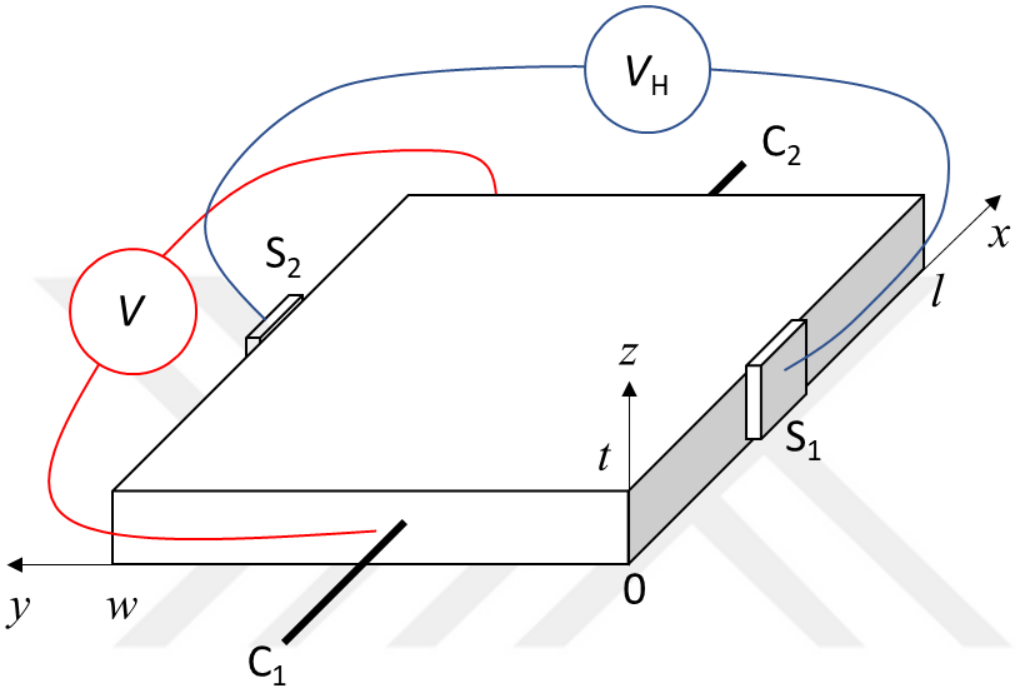

Figure 2.3. Rectangular plate Hall device with length l, width w, and thickness t. S_1 & S_2 and C_1 & C_2 denote sense/sensing and current contacts, respectively. Sense contacts are to be equipotential if there is no magnetic field through the device. When the bias current (I **x**) is applied by creating the potential difference V between the current contacts in the presence of the magnetic field (B **z**), the electric field $\pm E_H$ **y** arises, depending on the charge carrier type (+ for holes and – for electrons), so one can determine the type of the charge carrier by measuring the Hall voltage between the sense contacts.

To extend the analysis, let us consider the Hall effect in a material that can have both electrons and holes as charge carriers. Then, the current densities for electrons and holes are given by $\boldsymbol{J}_\mathbf{n} = -\, e\, n\, \boldsymbol{v}_\mathbf{n}$ and $\boldsymbol{J}_\mathbf{p} = e\, p\, \boldsymbol{v}_\mathbf{p}$, where n and p denote the charge

carrier concentration of electrons and holes, and $\boldsymbol{v}_{\mathbf{n,p}}$ represents the drift velocity of electrons, holes, respectively. Because $\boldsymbol{v}_{\mathbf{n}} = -\ \mu_n \boldsymbol{E}_{\mathbf{e}}$ and $\boldsymbol{v}_{\mathbf{p}} = \mu_p \boldsymbol{E}_{\mathbf{e}}$, $\boldsymbol{J}_{\mathbf{n}} = e\ n\ \mu_n \boldsymbol{E}_{\mathbf{e}}$ and $\boldsymbol{J}_{\mathbf{p}} = e\ p\ \mu_p \boldsymbol{E}_{\mathbf{e}}$, where μ_n and μ_p denote the mobility of electrons and holes, respectively. From $\boldsymbol{E}_{\mathbf{Hn}} = \mu_n (\boldsymbol{E}_{\mathbf{e}} \times \mathbf{B})$ and $\boldsymbol{E}_{\mathbf{Hp}} = -\ \mu_p (\boldsymbol{E}_{\mathbf{e}} \times \mathbf{B})$, one can derive the equations $\boldsymbol{E}_{\mathbf{Hn}} = (en)^{-1} (\boldsymbol{J}_{\mathbf{n}} \times \mathbf{B})$ and $\boldsymbol{E}_{\mathbf{Hp}} = -\ (ep)^{-1} (\boldsymbol{J}_{\mathbf{p}} \times \mathbf{B})$ for electrons and holes, respectively. Writing the equations in the form $\boldsymbol{E}_{\mathbf{H}} = -\ R_H (\mathbf{J} \times \mathbf{B})$, one obtains a coefficient for electrons and holes as $R_{Hn} = -\ (en)^{-1}$ and $R_{Hp} = (ep)^{-1}$, called the Hall coefficient for electrons and holes, respectively. Since the Hall coefficient is a function of the material's charge carrier concentration, it is a property of the material. It is also inversely proportional to the quantity $\frac{M \times V}{E'}$, introduced by Hall [7], which explains why he found the quantity constant for each of the metals. It is convenient to form an equation containing measurable macroscopic quantities the Hall voltage V_H and bias current I. According to the setup illustrated in Figure 2.3 equivalent to that used by Hall, $\mathbf{J} = \frac{I}{w\ t}\mathbf{x}$ and $\mathbf{B} = B\,\mathbf{z}$, implying $\boldsymbol{E}_{\mathbf{H}} = R_H \frac{I}{w\ t} B\,\mathbf{y}$. From the equation $V_H = V(S_1) - V(S_2) = \int_{S_1}^{S_2} \boldsymbol{E}_{\mathbf{H}} \cdot d\mathbf{r}$, one can find $V_H = \frac{R_H}{t} IB$. Therefore, the type of the charge carrier can be ascertained by measuring the polarities of the sense contacts. R_H / t is called the sheet Hall coefficient and denoted by R_{HS}. Note that the approximation enabling the derivations obtained thus far ignores the thermal motion of the charge carriers, and assumes isothermal conditions, the equilibrium charge carrier concentration, very small sense contacts and $l >> w$ [2].

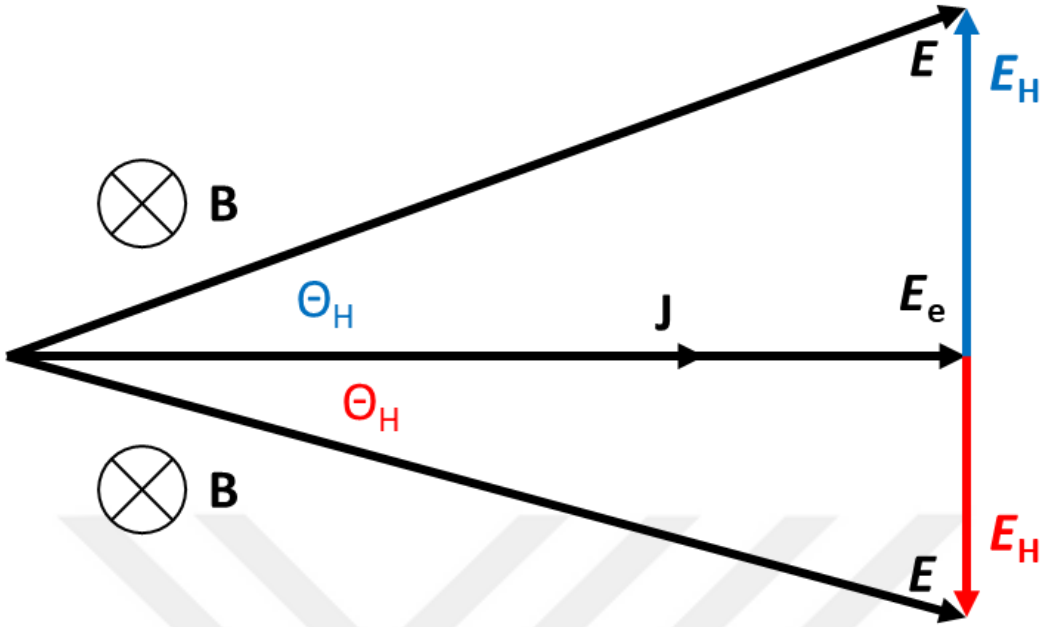

Figure 2.4. Vector diagram illustrating the definition of the Hall angle Θ_H. **J** represents the current density in the presence of the magnetic field **B.** $\boldsymbol{E_e}$ denotes the external electric field driving the current. The total electric field $\boldsymbol{E} = \boldsymbol{E_e} + \boldsymbol{E_H}$, where $\boldsymbol{E_H}$ represents the Hall electric field. The Hall angle and electric field associated with electrons and holes are colored in blue and red, respectively. The Hall angle is measured relative to the total electric field so that its sign coincides with the sign of the charge carrier.

2.2 Hall devices

The devices with four electrical contacts that can generate Hall effect as the device used by Hall are called Hall devices, so they do not necessarily have to be in the form of a rectangular plate. Plates of different shapes can generate the Hall effect as well as a rectangular plate. They are also called Hall elements, Hall generators, and Hall plates.

Since the complete manifestation of the Hall effect is only possible by using a Hall device in the form of an infinitely long strip, it generates the maximum Hall voltage $V_{H\infty}$ [2]. Then $V_{H\infty} > V_H$ for all V_H generated by finite-length Hall plates with arbitrary shapes. By introducing a parameter, one can write $V_H = GV_{H\infty}$, where G represents the parameter called the geometrical correction factor [2]. By the definition of $V_{H\infty}$, it is clear $0 < G < 1$ and $\lim_{w/l\to 0} G = 1$ (Figure 2.3). Consequently, the geometrical correction factor is of paramount importance to design efficient Hall devices. It is also important to position the sense contacts so that they have approximately equal electric potentials without the presence of a magnetic field, thereby making potential difference between the sense contacts equal to the Hall voltage. In addition, the sensing contacts should have the common potential approximately equal to the mid-potential of the current contacts. It is also of practical importance to choose highly symmetric geometry and a plate with both material and thickness uniformity. There are many practical shapes of Hall plates with large values of the geometrical correction factor [2,8], such as rectangular, bridge, square van der Pauw, and cross (Figure 2.5). For the rectangular-shaped plate (*a*) to have the geometrical correction factor $G \approx 1$, its sensing contacts must be very small and the inequality $l/w \geq 3$ should be satisfied [2]. Although the bridge-shaped device (*b*) has comparatively large contacts, it constitutes a good approximation to an infinitely long Hall device [2]. Having two pairs of sensing contacts, it enables the precise measurement of the voltage drop along the sample and the simultaneous magnetoresistance measurement. The square-shaped plate (*c*) is commonly used for both the Hall effect measurement and van der Pauw measurement [8]. Both the devices depicted by (*c*) and (*d*) have four-fold rotational symmetry and hence four equal contacts, thereby making the current and the sensing contacts interchangeable. The calculation of the geometrical correction factor G for the plates having four-fold rotational symmetry shows that G is a function of the parameters m and λ, defined by $m = \frac{\Theta_H}{\pi/2}$ and $\lambda = \frac{c}{b}$, where c and b denote the total length of the contacts and the plate boundary, respectively [2]. Therefore, for the cross-shaped plate, $\lambda = [1 + 2(h/k)]$ and hence the geometrical factor is a function of the charge carrier mobility μ and h/k. As a result,

a geometrical correction factor of $G \approx 1$ can easily attained with a cross-shaped device, despite its large contacts, whereas, for a rectangular device to have $G \approx 1$, the sensing contacts must be unrealistically small [2].

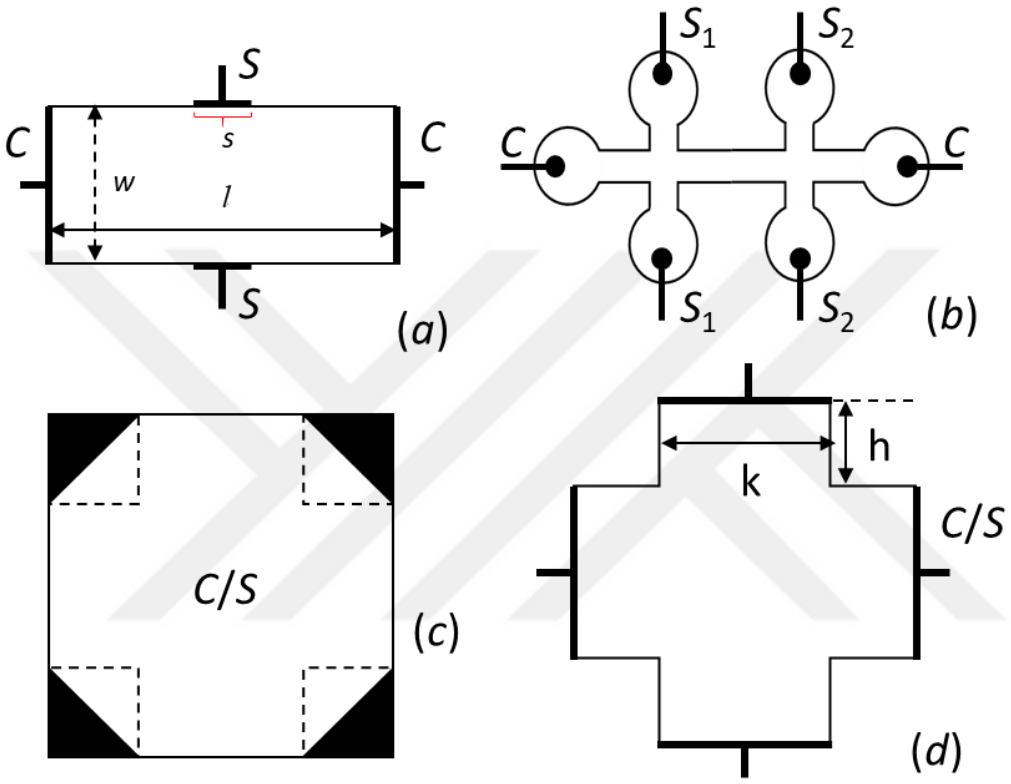

Figure 2.5. Four of the possible Hall plate geometries with which large geometrical correction factor can be easily attained. *C* and *S* denote current contacts and sense contacts, respectively. *C*/*S* designates the interchangeability of the current and sensing contacts.

There are mainly three reasons for fabricating Hall devices: to study charge carrier transport in condensed matter and Hall effect, to characterize semiconductors, and to produce magnetic sensors called Hall magnetic sensors, or Hall sensors.

Application of Hall devices as magnetic sensors is a natural consequence: the Hall voltage can be considered as a response of a Hall device to a magnetic field. Therefore, the principles for designing and fabricating efficient Hall sensors include those associated with Hall devices. So, to fabricate a high-performance Hall sensor, it is of primary importance to choose a Hall plate in a shape that maximizes the geometrical correction factor, thereby maximizing the Hall voltage. As shown above, one can achieve this objective by utilizing a cross-shaped plate without unpractically reducing the sizes of the electrical contacts.

Sensitivity is the principal figure of merit for a Hall sensor. The absolute sensitivity S_A is defined by the equation $S_A = |V_H / B_n|$, where B_n represents the component of the magnetic field normal to the surface of the Hall plate, for determined operating conditions such as bias current/voltage, frequency, and temperature.

The relative sensitivities, current- and voltage-related sensitivities are defined by normalizing the absolute sensitivity with respect to the bias current and voltage, resulting $S_I = S_A / I$ and $S_V = S_A / V$, respectively. Since $V_H = G\,(R_H / t)\,I\,B_n$ for a Hall device, $S_I = G\,R_H / t$. As a result, S_I is inversely proportional to the charge carrier density. As for the voltage-related sensitivity, from the equation $\boldsymbol{E_H} = \mu\,(\boldsymbol{E_e} \times \mathbf{B})$ representing the response of the device, one obtains the approximation $\frac{V_H}{w} = \mu \frac{V}{l} B_n$ for a rectangular Hall plate with very small sense contacts and $l / w >> 1$, implying $V_H = \mu\,(w / l)\,V\,B_n$, where μ denotes the charge carrier mobility. For a general Hall device, $V_H = \mu\,(w / l)\,G\,V\,B_n$, where G represents the geometrical correction factor. In consequence, $S_V = \mu\,(w / l)\,G$. Therefore, materials having charge carriers with low concentration and high mobility are to be chosen for fabricating high performance Hall sensors.

CHAPTER 3

GRAPHENE

3.1 Electronic, Mechanical, and Thermal Properties

Extraordinary properties of graphene stem from its special two-dimensional crystal structure, which is comprised of hexagonally arranged sp^2-hybridized carbon atoms. Each carbon atom forms in-plane covalent bonds with its three nearest neighbor carbon atoms, with its three valence electrons coming from the half-filled sp^2-orbitals. These covalent bonds, called σ bonds, give rise to its extreme tensile strength and thermal conductivity. On the other hand, unhybridized half-filled out-of-plane 2p orbitals of the carbon atoms provide an outstanding electrical conductivity [9]. The nearest-neighbor distance in graphene, which we denote with *a*, is about 1.42 Å. Therefore, the real space basis vectors $\mathbf{a_1}$ and $\mathbf{a_2}$ of the unit cell, which is a rhombus containing two nonequivalent carbon atoms denoted with A and B, can be represented with $(3a/2, \sqrt{3}a/2)$ and $(3a/2, -\sqrt{3}a/2)$ in cartesian coordinates, respectively (Figure 3.1). So the lattice constant of graphene equals $\sqrt{3}a$, and the basis vectors corresponding to $\mathbf{a_1}$ and $\mathbf{a_2}$, for the reciprocal space are given by $\mathbf{b_1} = (2\pi/a)\ (1/3,\ 1/\sqrt{3})$ and $\mathbf{b_2} = (2\pi/a)\ (1/3,\ -1/\sqrt{3})$ in cartesian coordinates, respectively.

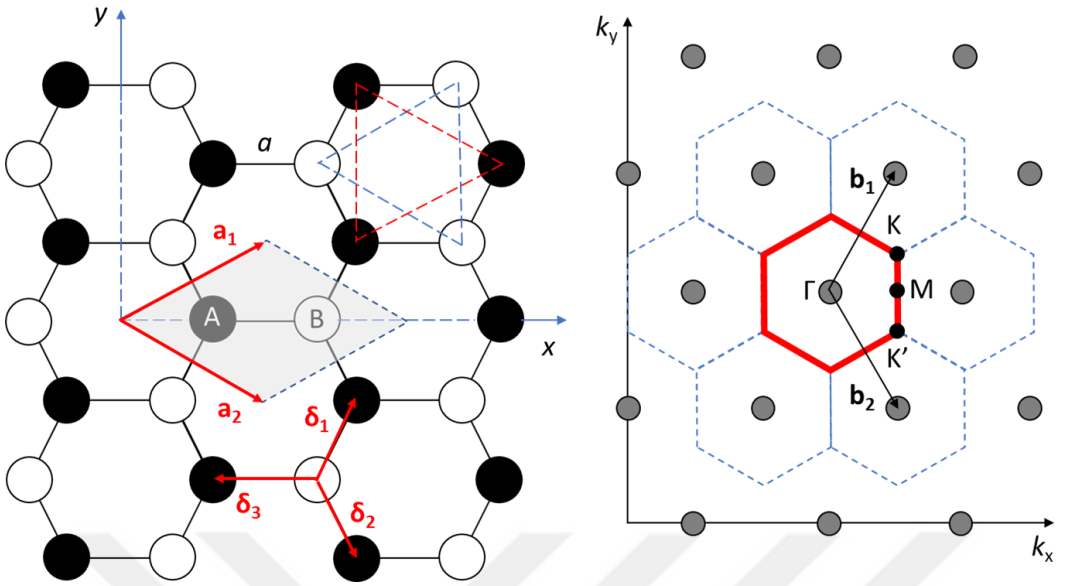

Figure 3.1. Crystal structure of graphene. Left: Two-dimensional hexagonal lattice in real space with the basis of two nonequivalent carbon atoms A and B, each of which belongs to a different triangular sublattice shown in blue and red. The unit cell highlighted in gray is a rhombus with basis vectors highlighted in red. $\boldsymbol{\delta_i}$ represents the nearest-neighbor vector i. The vertical edges are zig-zag and the horizontal edges are armchair. Right: Corresponding reciprocal lattice with basis vectors $\mathbf{b_1}$ and $\mathbf{b_2}$. The boundary of the first Brillouin zone is highlighted in red. The high symmetry points Γ, M, K and K' are marked.

Although the electronic properties of graphene were experimentally revealed by the seminal work of Novoselov *et al.* [1], its electronic structure was already studied about half a century before by Wallace [10] in order to formulate the band theory of graphite by using the tight binding approximation. Graphene manifests ambipolar field effect, so mobile electrons and holes can be induced by the application of an electric field [1]. These charge carriers are truly two-dimensional and have room-temperature mobility of up to 10,000 $cm^2/(Vs)$ in ambient conditions on SiO_2/Si [1] and of up to 200,000 $cm^2/(Vs)$ was manifested by suspended graphene at electron densities of ~2×10^{11} cm^{-2} [11]. In addition, their dispersion relation is linear [12], which can be

theoretically shown by using the tight-binding approximation [9,13]. The concentration of the charge carriers can be finely tuned by the electric-field effect, however, the conductivity of graphene never falls below a mininum value related to the quantum unit of conductance, even if the carrier concentration approaches zero [12]. This manifestation of a minimum conductivity is one of the phenomena indicating that the charge carriers behave like two-dimensional Dirac fermions [12].

Tight-binding approach provides a good approximation to the band structure of graphene [9,13]. By using the sublattice description of graphene lattice, in which the graphene lattice is described as two intertwined triangular sub-lattices pertaining to the two nonequivalent carbon atoms denoted by A and B (Figure 3.1), one can write the tight-binding Hamiltonian as the sum over all the electronic processes in graphene related to electrons hopping to nearest- or next-nearest-neighbor atoms [13]. Thus it has the form

$$H = -t\sum_{\langle i,j\rangle,\sigma}\left(a^{\dagger}_{\sigma,i}b_{\sigma,j} + \text{H.c.}\right) - t'\sum_{\langle\langle i,j\rangle\rangle,\sigma}(a^{\dagger}_{\sigma,i}a_{\sigma,j} + b^{\dagger}_{\sigma,i}b_{\sigma,j} + \text{H.c.}),$$

where $a^{\dagger}_{\sigma,i}$ ($a_{\sigma,j}$) is the operator for creating (annihilating) an electron with spin σ on site $\mathbf{R}_i$ on sublattice A, and H.c. is an abbreviation for "Hermitian conjugate". An equivalent definition for the other sublattice is straightforward by replacing (a,A) with (b,B). t(≈2.8 eV) and t' are nearest- and next-nearest-neighbor hopping energies, which correspond to hopping between different sublattices and in the same sublattice, respectively. This Hamiltonian yields the energy bands of the form $E_{\pm}(\mathbf{k}) = \pm\, t\sqrt{3 + f(\mathbf{k})} - t'f(\mathbf{k})$ with

$$f(\mathbf{k}) = 2\cos(\sqrt{3}k_y a) + 4\cos\left(\frac{\sqrt{3}}{2}k_y a\right)\cos\left(\frac{3}{2}k_x a\right),$$

where the plus sign is for the upper (π^*) and the minus sign for the lower (π) band. π band is formed by overlapping neighboring unhybridized orbitals oriented perpendicular to the graphene lattice. This overlap results in delocalization and hence band formation. In intrinsic (undoped) graphene, π band is filled up to the point where it meets π^* band; each carbon atom contributes one electron completely filling

the valence band and leaving the conduction band empty. π and π^* bands meet at the high symmetry K and K' points of the Brillouin zone (Figure 3.1) and their equivalent points in the reciprocal space (Figure 3.2). These points are also called the charge neutrality points of graphene. So graphene is a gapless semiconductor or a zero-overlap semimetal. Note that the π and π^* bands are asymmetric unless $t' = 0$ (Figure 3.2). However, it is possible to obtain a linear dispersion relation $E_{\pm}(\mathbf{k}) = \hbar v_F |\mathbf{k} - \mathbf{K}|$ for $|\mathbf{k} - \mathbf{K}| << \mathbf{K}$, by expanding the energy bands at the points sufficiently close to the charge neutrality points, where $\mathbf{k} = (k_x,k_y)$ and $v_F = 3ta/(2\hbar) \approx 1\times10^6$ m/s, is the Fermi velocity of the charge carriers of graphene, to exist within this approximation [9,13]. Therefore, the band structure of graphene can be approximated with cones around charge neutrality points (Figure 3.2), where its charge carriers behave like Dirac fermions [12]. For this reason, the charge neutrality points are also called the Dirac points and the conical energy band portion is called the Dirac cone. This approximation also explains the ambipolar field effect in graphene (Figure 3.2).

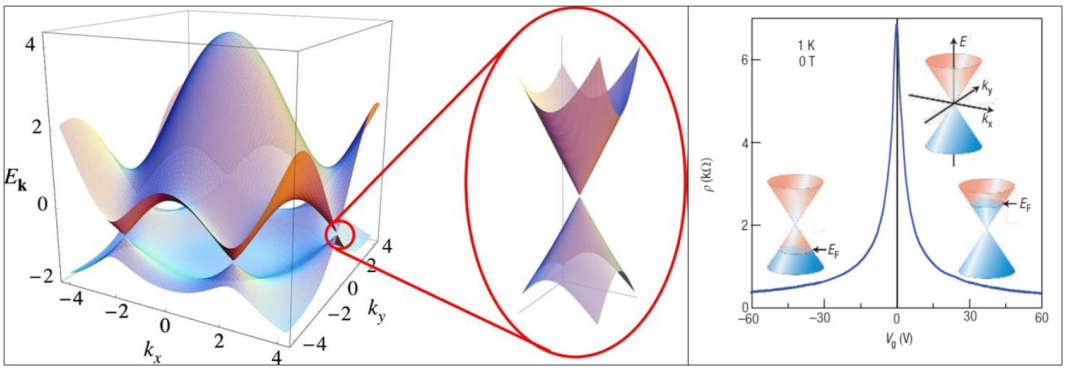

Figure 3.2. Left: Electronic band structure of graphene resulted from tight-binding approximation. Energy is in unit of t, with t = 2.7 eV and t' = -0.2 t. Also shows a conical portion of the band structure close to one of the Dirac points. Reprinted with permission from A. H. Castro Neto, F. Guinea, N. M. R. Peres, K. S. Novoselov, and A. K. Geim, The electronic properties of graphene, Rev. Mod. Phys. 81, 109 – Published 14 January 2009. Copyright 2021 by the American Physical Society. Right: Change in the resistivity of graphene caused by the electric field effect through the application of gate voltage V_g. The insets show change in the Fermi energy level with respect to V_g. Reprinted by permission from Springer Nature, Nature Materials, The Rise of Graphene, A. K. Geim *et al.*, Copyright © 2007.

It is crucial to understand the elastic properties of graphene for its application in flexible eletronics. By applying atomic force microscope nanoindentation to suspended graphene, Lee *et al*. demonstrated that graphene can be considered a two-dimensional membrane with zero bending stiffness and breaking strength of 42 N/m, which required the use of cantilevers with diamond tips for the experiments [3]. Despite its promising results, this research did not completely describe the mechanical behavior of graphene because it only involved suspended graphene. Especially for flexible electronic applications, it is important to know the mechanical behavior of graphene on flexible substrates. Androulidakis *et al*. showed that, depending on the magnitude of adhesion between graphene and the substrate, even small uniaxial strains cause graphene to wrinkle because of its very low bending

stiffness [14]. These wrinkles could adversely affect the performance of a flexible electronic device based on graphene [14].

Thermal conductivity of graphene was measured by Balandin *et al*. via the confocal micro-Raman spectroscopy, yielding the values in the range from ~ 4.84 to 5.30 kW/(mK), which is much larger than copper's and can exceed those of carbon nanotubes [15].

3.2 Production, Transfer, and Characterization

Although the mechanical exfoliation of graphite provided the samples of graphene showing the outstanding properties of graphene [1,11,16–20], it is not a feasible method for the large scale production of graphene because it is a very slow, labor-intensive, and low-yield. It is categorized as one of the top-down production methods.

There are mainly two approaches to the production of graphene: top-down and bottom-up. The former mostly involves the exfoliation of graphite by overcoming the van der Walls force between its layers by mechanical, chemical, electrical, and electrochemical means [21]. In addition, graphene nanoribbons can be produced by unzipping carbon nanotubes (CNT) [21]. On the other hand, the bottom-up approach aims to transform carbon-containing molecules/materials into graphene on substrates [21].

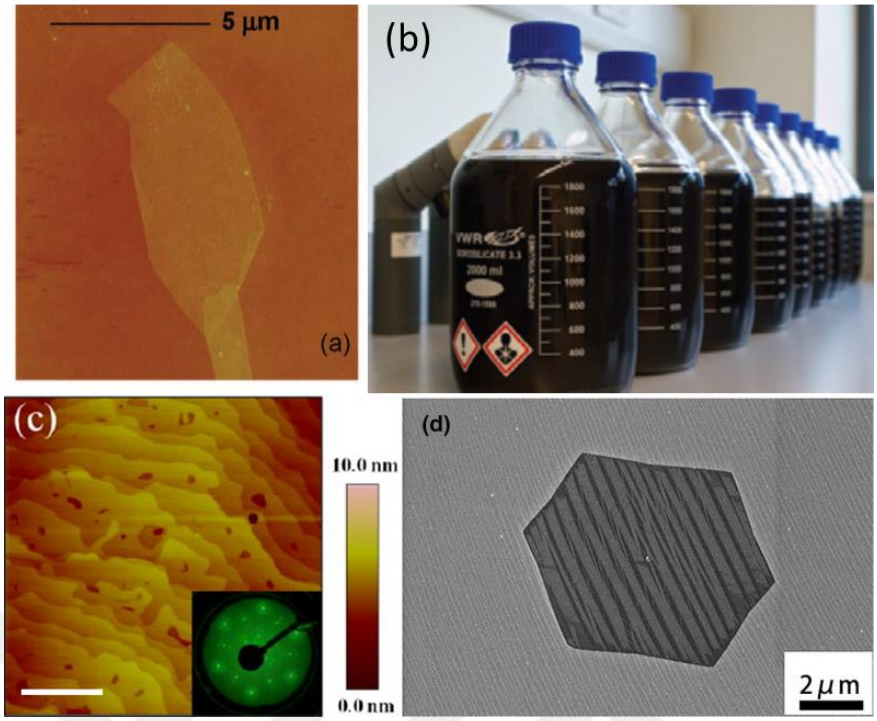

Figure 3.3. Outputs of four prominent graphene production methods. (a) Atomic force microscopy image of graphene obtained by micro-mechanical exfoliation or microcleavage of graphite transferred onto SiO_2/Si substrate. Reprinted with permission from Balandin *et al.*, Nano Lett. 2008, 8, 3, 902–907, Copyright © 2008 American Chemical Society. (b) Graphene-N-methyl-2-pyrrolidone dispersions produced via shear exfoliation. Adapted by permission from Nature, Nature Materials, Scalable production of large quantities of defect-free few-layer graphene by shear exfoliation in liquids, Paton *et al.* Copyright © 2014. (c) Atomic force microscopy image of the graphene grown on SiC surface after annealing at 1530°C for 20 min. The inset shows corresponding low energy electron diffraction patterns obtained at room temperature (Scale bar: 2.5 μm). Adapted from Journal of Electron Spectroscopy and Related Phenomena Volume 184, Issues 3–6, Yu *et al.*, New synthesis method for the growth of epitaxial graphene, Pages 100-106, Copyright (2021) with permission from Elsevier. (d) Graphene grain produced on copper by chemical vapor deposition. Reprinted by permission from Springer, Journal of Electronic Materials, Re-nucleation and Etching of Graphene During the Cooling Stage of Chemical Vapor Deposition, Liang *et al.* Copyright © 2019.

The top-down approach includes the production by the reduction of graphene oxide, the arc-discharge method, liquid-phase exfoliation (LPE), solid-state or mechanical exfoliation, and unzipping CNTs [21]. Except for unzipping CNTs, this approach is essentially the upscaling of what was done by Novoselov *et al*. to obtain graphene [1,21]. Among the methods listed above, LPE is the most promising, yields colloidal suspensions of high-quality graphene flakes [21]. Although the approach addresses the upscaling problem, it still results in graphene flakes having sizes of the order of 100 μm at most [21]. Therefore, it is not suitable for applying the superior properties of graphene in large-area electronics.

The bottom-up approach primarily entails the growth of graphene on a substrate by controlling the flux of carbon atoms from within the substrate or an external source. Two prominent methods included in this category are epitaxial growth of graphene on silicon carbide (SiC) and chemical vapor deposition (CVD) of graphene.

Epitaxial growth of graphene on commercial single-crystal SiC is mainly based on the evaporation of silicon atoms in SiC in ultra-high vacuum (UHV) to facilitate the formation of a carbon-rich surface via the segregation of carbon atoms in SiC, followed by the reconstruction of the carbon-rich surface [22]. Alternatively, the process can be done in atmospheric pressure by increasing the annealing temperature, which can result in graphene of higher quality [22]. Also, because of the high cost of single-crystal SiC, single-crystal SiC thin films and polycrystalline SiC need to be considered as alternative growth substrates [22]. Although this method does not require graphene transfer and provides graphene on insulating substrate, which can be readily processed by the state-of-the-art lithographical techniques, some technical issues need to be resolved to render the method feasible for commercial applications [22]: (i) the high cost of single-crystal SiC, which requires the search for low-cost substitutes, (ii) the necessity of high temperatures usually above 1200°C, which considerably increases the necessary energy input, thereby increasing the cost of the method, (iii) the defects in the epitaxial graphene that make it inferior to the mechanically-exfoliated graphene in terms of the electronic properties, (iv) the coupling between the epitaxial graphene (EG) and the substrate (SiC) that causes the

electronic properties of EG to deviate from those of the mechanically exfoliated graphene, which necessitates a method to decouple EG from SiC.

First demonstrated by Li *et al.* [23] by using copper foils, chemical vapor deposition (CVD) of graphene has proven to be the most promising bottom-up method for the synthesis of large-area graphene. The method basically involves the formation of graphene on a substrate from the carbon atoms provided by decomposition of carbon-containing molecules, called carbon precursors, at high temperatures usually ≥ 1000°C.

After the successful demonstration of the method on copper by Li *et al.* [23], many metals have been experimented upon to obtain graphene via CVD, including iron, ruthenium, cobalt, rhodium, iridium, nickel, platinum, gold, and stainless steel [24]. All these metals manifest catalytic activity during the CVD process, thereby reducing the temperature required for the dissociation of the carbon precursors, e.g. methane [23], methanol, ethanol, and propanol [25]. Hence graphene is formed on their surface as a result of the process. Despite all these experiments with different metals, copper remained to be the most favorable catalyst for the CVD of graphene, because of its abundance, processability, and low carbon solubility [24]. The CVD of graphene on catalytic metals essentially results from two processes: precipitation/segregation and surface-mediated diffusion of carbon atoms, explaining the graphene growth on nickel and copper, respectively [24,26]. Because of the low carbon solubility in copper, the graphene growth on copper is expected to be self-limited, thereby resulting in a monolayer of graphene throughout its surface [26]. However, small percentage of multilayer patches are commonly found on copper resulted from the CVD of graphene on copper [24]. This is possibly because of the roughness of the polycrystalline copper surface, which allows carbon atoms to cluster at the grain boundaries. This explanation was supported by the decrease in multilayer percentage obtained by polishing the copper surface [24].

With respect to the heat generation approach, CVD systems are divided into two categories: hot-wall and cold-wall. In hot-wall systems, the whole reaction chamber

is heated radiatively, whereas only the substrate on which the reaction should occur is heated in cold-wall systems. Various cold-wall systems have been used for the CVD of graphene by direct conduction heating [27], Joule heating [28], or by heating with laser [29] on nickel, and by inductive heating on copper and platinum [30]. Variation in hot-wall systems is also possible, such as using halogen lamps in order to obtain very high heating and cooling rates [31]. Moreover, CVD systems should be considered in two groups regarding to the pressure inside the reaction chamber: low-pressure chemical vapor deposition (LPCVD) and ambient/atmospheric-pressure chemical vapor deposition (APCVD).

Since the work of Li *et al.* [23], the CVD of graphene on copper and on copper-nickel alloys has proven to be the most promising method to obtain large-area graphene with properties comparable to those of the mechanically exfoliated graphene. In an endeavor to synthesize large-area graphene physically equivalent to the mechanically exfoliated graphene, researchers have made important discoveries. It is known that polycrystalline metals result in polycrystalline graphene because graphene grains with random orientations nucleate on many sites on the surface of catalyst surface. As a result, one must decrease the nucleation density of the grains to increase the crystallinity of graphene. So, there are two routes to follow to obtain large area single crystal graphene: reducing the nucleation to a limit that will allow a single crystal graphene grain to grow a large-area single-crystal graphene sheet or controlling the nucleation so that the single-crystal graphene grains with almost the same orientation will coalesce into a large-area single-crystal graphene sheet.

The former usually involves finding ways to remove possible nucleation agents [32–34] from the catalyst surface and reducing the roughness of the surface, thereby making the surface as uniform as possible. Zeng *et al.* showed that using liquid metal as catalyst substrate could resolve the uniformity issue [35]. Although Cu(111) is the most favorable [36] for the graphene growth because of the smallest lattice mismatch with graphene and the largest carbon diffusion rate compared with the other crystal surfaces of copper, it was demonstrated that a growing graphene grain could become insensitive to the crystal orientation of the copper grain surface and grows with its

original orientation across the copper grain boundaries [37–39]. Based upon this fact, one can grow a single-crystal graphene grain indefinitely by locally feeding it with optimized local precursor flow, which was shown by Wu *et al.* [40]. This approach was further developed by Vlassiouk *et al.* and they obtained a foot-long virtually single-crystal graphene film on polycrystalline copper and copper-nickel alloy foils [41].

For the latter route to obtain a large-area single-crystal graphene, employing single-crystal copper could be solution. Nevertheless, it would be very costly. Xu *et al.* demonstrated [42] that polycrystalline copper surface could be transformed into Cu(111) by using a temperature-gradient-driven annealing based upon the copper surface melting [43] below its bulk melting point and the fact that (111) surface of copper has the lowest formation energy [42]. As a result, they produced a meter-sized single-crystal graphene [42].

Since the electronic and optic applications requires graphene to be situated on an insulating or a semiconductor substrate, in order to avoid the damage possibly caused by the transfer of graphene from the catalytic substrate, there has been a concerted effort to synthesize graphene directly on insulating materials including silicon [44], SiO_x/Si [45], SiO_2 [46,47], glass [48], and sapphire [49]. Also, plasma-enhanced chemical vapor deposition (PECVD) was used for directly growing graphene on SiO_2/Si [50].

Although the ultimate goal of the CVD of graphene may appear to be the production of large-area single-crystal graphene, some polycrystalline graphene samples have already been reported to show unexpectedly high quality with regard to the electronic [51], mechanical [52], and thermal [53] properties. Therefore, it is possible to fabricate high-performance devices out of polycrystalline graphene, particularly by using a proper encapsulation [51] and by grain boundary engineering [52] for the electronic and mechanical applications, respectively.

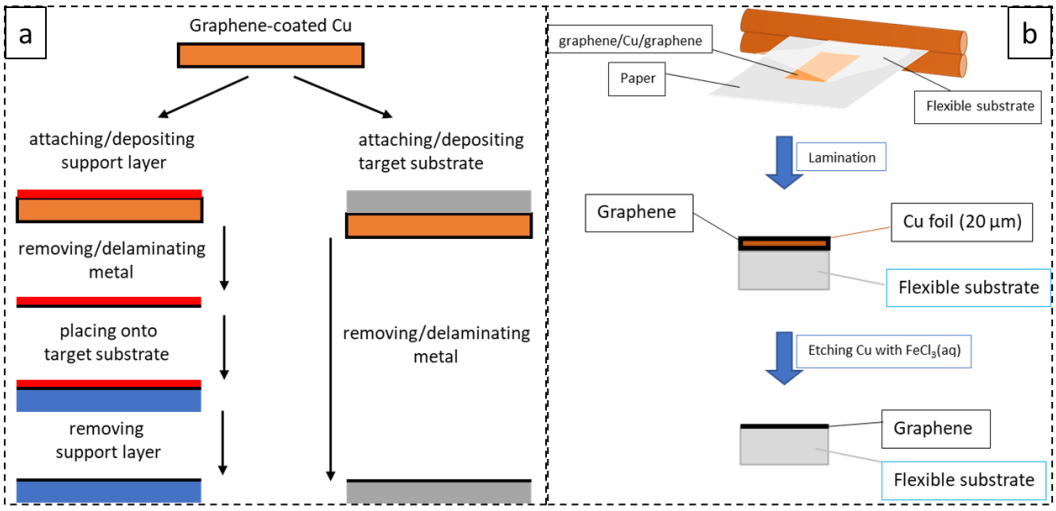

Figure 3.4. (a) Schematics illustrating temporary-support-layer-assisted transfer (left) and direct transfer (right) of graphene from metal growth-substrate to target substrate. Orange rectangle with black frame represents graphene-coated metal growth-substrate. Red rectangle represents temporary support layer. Blue and gray rectangles represent target substrates. Metal substrate is removed by peeling or chemical etching. Support layer is removed by peeling, dissolving, or thermal annealing. (b) Schematic depiction of direct transfer of graphene from copper onto flexible substrate via lamination.

As mentioned above, graphene grown on metal substrates needs to be transferred onto insulating substrates, particularly for electronic and optic applications. There are mainly two types of methods for the transfer: direct transfer and transfer by employing a temporary support layer, onto the target substrate (Figure 3.4).

Transfer by a temporary support layer begins with the deposition or attachment of the support layer onto the graphene-coated metal growth-substrate. Usually, resins used in lithography are deposited onto the growth substrate. Polymethylmethacrylate (PMMA) is one of the most common resins used as the temporary support layer [54,55]. However, since it can cause stubborn organic residues on the transferred graphene, researchers are in search of alternative organic materials, including paraffin [56] and

wax [57]. Atomic layer deposition (ALD) of oxide layers [58] and gold [59,60] were also used for cleaner transfer of graphene and as oxide and contact materials readily available for electronic applications after the transfer, respectively. In addition, adhesive tapes could be used as temporary support layer. Especially, thermal release tapes (TRT) can be used for the transfer by using a hot press or laminator [61].

Direct transfer entails the deposition or attachment of the target substrate onto the growth substrate. Usually, a curable polymer solution is deposited on to or a film is attached to the growth substrate [62]. The attachment of the target substrate is facilitated by applying pressure and/or heat to the stack formed by the film and the growth substrate. The target substrate either has an adhesive layer [63] or a property that causes a viscoelastic transition [64]. Both possibilities result in close contact between the surface of the substrate and graphene. Polyethylene (PET) films coated with ethyl vinyl acetate (EVA) are one of those films that can be attached to the graphene-bearing metal foils [65,66]. The attachment of the PET film to the graphene is provided by the EVA coating, which softens during the hot lamination. Upon removal of the metal foil, graphene is transferred onto the PET film [65,66]. In order for a target substrate to be suitable for the direct transfer, it must be hydrophobic [64,67,68]. It is even possible to directly transfer graphene without a support layer onto SiO_2/Si wafer if its target surface is coated with a highly hydrophobic self-assembled monolayer [69]. Furthermore, Lin *et al.*[70] demonstrated that it is possible to directly transfer graphene on copper without using a polymer support that is to prevent folding and/or tearing graphene by adjusting the surface tension of the copper etchant.

Regardless of the method, whether direct or not, transferring graphene from a metal growth substrate involves the removal of the metal. Usually, it is removed by chemical etching with aqueous solution, thereby dissolving the metal into the solution. However, the etching solutions, or etchants, can have undesirable effects upon graphene, causing unintentional doping and residues, which can degrade its electronic properties [71]. Therefore, the usage of etchants for the graphene transfer needs optimization so that it gives consistent and reproducible results without

causing any degradation [72]. Alternatively, it is possible to totally abandon the etching and delaminate the metal from the stack by electrochemical means [73,74] or by using hot deionized (DI) water [75], thereby providing the recyclable use of the metal.

As used by Novoselov *et al.* [1], optical microscopy (OM), atomic force microscopy (AFM), and Raman spectroscopy are indispensable tools for the identification of graphene on SiO_2/Si among the flakes resulted from the mechanical exfoliation of graphite. The CVD of graphene requires additional tools, including scanning tunneling microscopy (STM) and electron microscopy (EM), and X-ray photoelectron spectroscopy (XPS).

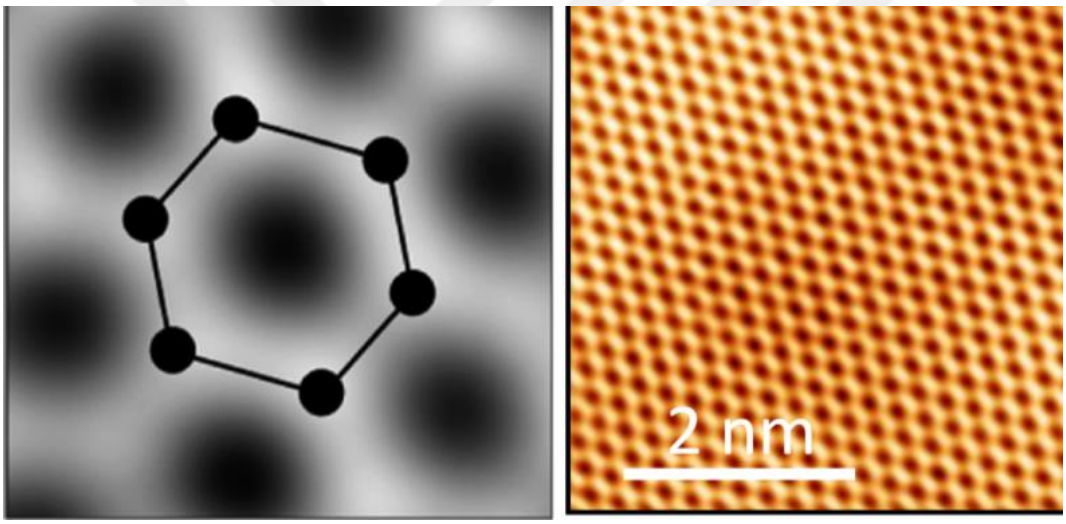

Figure 3.5. Left: Atomic resolution image of graphene by transmission electron microscopy. Adapted with permission from Nano Lett. 2010, 10, 11, 4328–4334. Copyright © 2010 American Chemical Society. Right: Atomic resolution image of graphene on copper via Scanning Tunneling Microscopy. Reprinted from Science Bulletin, Volume 62, Issue 15, Xu *et al.*, Ultrafast epitaxial growth of metre-sized single-crystal graphene on industrial Cu foil, Pages 1074-1080, Copyright 2021, with permission from Elsevier.

To optimize the CVD process, one must be able to consistently assess the quality of the output, i.e., graphene. Firstly, since CVD mostly results in polycrystalline graphene, it is desirable to image the grain boundaries of graphene and thus calculate the average grain size. Although STM [76] and EM [77] are capable of providing atomic-resolution images (Figure 3.5), using these tools to study grains of large-area graphene would be very time-consuming. This problem can be resolved by using nematic crystals, based upon the fact that nematic crystals become oriented in accordance with the orientation of the copper grain on which they are deposited [78]. Moreover, a more facile method was developed. Since the grain boundaries are not as effective as the graphene grains in protecting the metal from oxidation, the oxidation of the metal begins along with the grain boundaries. This fact implies that the grain boundaries can be imaged via selective oxidation of the graphene-carrying metal substrate. The feasibility of the method was demonstrated via photocatalytic oxidation [79]. Exploiting the higher reactivity of the grain boundaries, Lee *et al.* obtained a clearer image by exposing graphene-bearing metal to oxygen plasma, followed by heating in air [80]. In addition, Fan *et al*. were able to image the grain boundaries of graphene transferred onto SiO_2 through vapor hydrofluoric acid exposure [81].

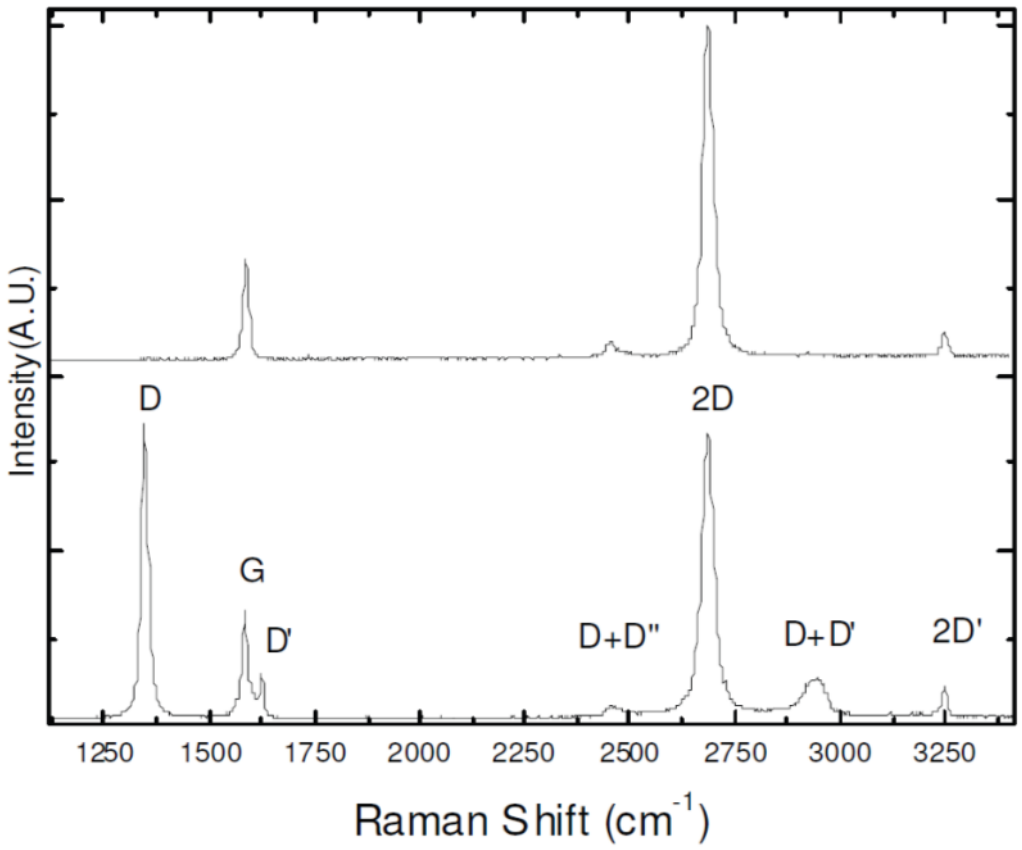

Figure 3.6. Two Raman spectra representative of pristine (top) and defective (bottom) graphene. Reprinted by permission from Nature, Nature Nanotechnology, Raman spectroscopy as a versatile tool for studying the properties of graphene, Andrea C. Ferrari & Denis M. Basko, Copyright © 2013.

Raman spectroscopy is one of the most important characterization tools in graphene research. It could reveal the number of graphene layers in a sample [82,83], give information about charged impurities [84], the doping type and level [85–88]. It could also be used to study the defects and strain in graphene [89]. All incident wavelengths are resonant because of the absence of a band gap in graphene [90]. As a result, Raman spectrum of graphene could have many peaks (Figure 3.6). Nevertheless, D, G and 2D peaks are mostly used for the characterization; they are observed at ~1350, ~1550 and ~2700 cm^{-1} (Figure 3.6). The position, height, area, full width at half maximum

(FWHM) of a peak are all characteristic quantities to be accurately measured for the characterization of graphene. For instance, the ratio of the height of the D peak to that of the G peak is considered a measure of the defectiveness of graphene because it is activated by defects [82,90]. In addition to the above-mentioned characteristic quantities of the peaks, the shape of a peak could facilitate the characterization. For example, one can distinguish single-layer graphene from multilayer graphene by just looking at the shapes of the D+D'' (~2450 cm^{-1}), also denoted G^*, and 2D peaks [82,83]: in the Raman spectrum of single-layer graphene, the G^* peak is relatively much sharper and the 2D peak can be fitted with a single Lorentzian curve. Sometimes called the G' peak, as a relic of erroneous nomenclature, because it is the second most prominent peak observed in graphite samples at all times, the 2D peak/band has nothing to do with the G peak: the 2D peak is due to a double resonance process and hence it is affected by the change in the number of graphene layers [82]. On the contrary, the shape of the G peak does not change in relation to the number of layers [83]. Although the D, G and 2D peaks are all caused by in-plane vibrations, this contrast is because the 2D peak is due to the double resonance Raman process sensitive to the band structure of graphene; the uniqueness of the electronic band structure of single-layer graphene results in this difference [82,90]. Since the π and π^* bands of bilayer graphene are divided into four bands because of the interaction between the graphene layers, there is a large difference even between the shape of the 2D peak of single- and bi-layer graphene and the difference continues to increase with the number of layers [83]. In addition to the shape, the height of the peaks could show variation with respect to the number of layers [82,83]. It was demonstrated that the height of the G peak monotonically increases with the number of layers up to about 10 layers and decreases beyond that, and that of 2D peak tends to decrease as the number of layers increases [83]. Prompted by this fact, Yoon *et al.* showed that the ratio of the height of the 2D peak to that of the G peak could be used to determine the number of layers by Raman mapping [83]. Although this ratio is frequently found to be larger than 2 for single-layer graphene and thus appears to provide a dependable method for determining the number of layers, solely relying upon it without

considering the shape of the 2D peak could be misleading. This is because the doping causes large variations in the height as well [84–86]. Casiraghi *et al.* demonstrated the existence of an order of magnitude variation and very high doping level of up to ~10^{13} cm^{-2} in graphene flakes obtained by microcleavage of graphite without exposing to any intentional doping, thereby showing the level of doping that can be caused by the transfer process [84]. Doping increases the height of the G peak and decreases its FWHM [78,86,90]. Both these phenomena can be explained in terms of the Raman processes in graphene (Figure 3.7). Decrease in the FWHM is caused by the blockage of the decay channels of phonons into electron-hole pairs due to the Pauli exclusion principle: as doping increases the energy needed to create electron-hole pairs, the electron-hole gap becomes larger than the energy of some phonons [85]. Increase in the height can also be explained with the Pauli blockage [90]: since there is quantum interference between the electronic states corresponding to the electronic wavevectors and destructive interference plays an important role in determining the G peak, doping causes the cancellation of some of the destructive interference by blocking some of the interband transitions and thus increases the total contribution to the G peak, thereby increasing the height of the G peak (Figure 3.7 top). In spite of these complications, being fast and nondestructive, Raman spectroscopy is still a very valuable characterization method for the graphene research.

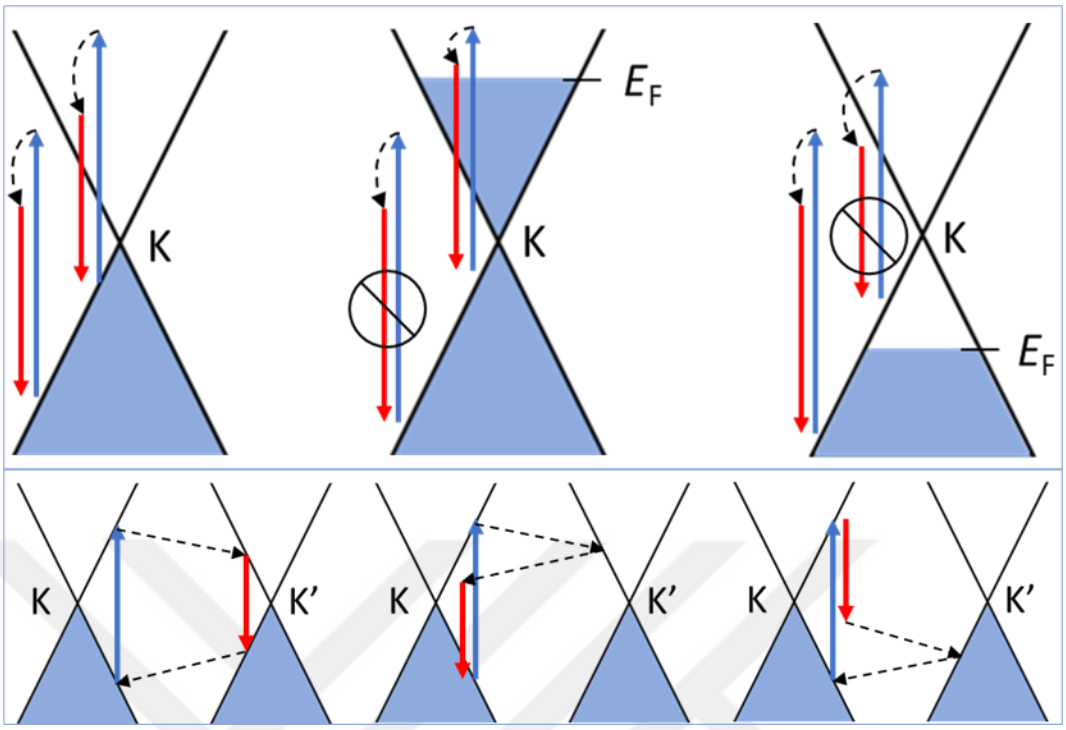

Figure 3.7. Schematic description of the Raman processes that give rise to the G and 2D peaks in graphene. Blue arrow represents photon absorption, red arrow represents photon emission, and dashed curvy arrow represents electron-phonon scattering. Top: The intrinsic case in which the Fermi level is at the Dirac point and thus all interband transitions allowed (left). The Fermi level is increased by n-type doping and thus some of the interband transitions are blocked due to the Pauli exclusion principle, i.e., transition to an occupied state is impossible (middle). The Fermi level is lowered by p-type doping and hence some interband transitions are blocked by the Pauli exclusion principle, i.e., transition from an unoccupied state is impossible (right). Bottom: Schematics for the double resonance Raman processes that give rise to the 2D peak involving two-phonon intervalley scattering. Illustrations in the middle and on the right are of small contribution. Solid arrows denote photon absorption (blue) and emission (red), and dashed arrows denote phonon emission.

XPS is another very important characterization tool to study CVD-graphene. It is particularly important for assessing the graphene transfer. Since grain boundaries of

polycrystalline CVD-graphene has higher reactivity, they could react with materials used for the transfer. Such reactions could severely degrade the electronic properties of graphene. XPS provides information about the bonding in graphene, thereby helping choose or develop the most suitable transfer process.

Electronic characterization of graphene usually entails the microfabrication of a Hall bar device, which enables measurements of Hall voltage, magnetoresistance, and sheet resistance for different charge carrier densities corresponding to different gate voltages [1]. Then the field-effect mobility can be found. However, for large-area applications, it is possible to obtain sheet resistance, mobility and conductivity mapping by using THz radiation without contacting graphene [91,92].

We synthesized graphene on 20μm-thick polycrystalline copper foil by using our hot-wall atmospheric pressure chemical vapor deposition (APCVD) system (Figure 3.8). The system mainly consisted of a split furnace (PROTHERM), a mechanical vacuum pump providing a base pressure of 40 mTorr, a pressure gauge controller, an electrical power module with a PID temperature controller, an open-ended quartz tube, vacuum flanges, electronic mass flow controllers (AALBORG), needle valves connected to the flow controllers at their inlets, a stainless-steel chamber for mixing the gases before directing into the reaction chamber, a gas leak detector for flammable gases, and gas cylinders for argon, hydrogen, and methane, connected via stainless-steel piping.

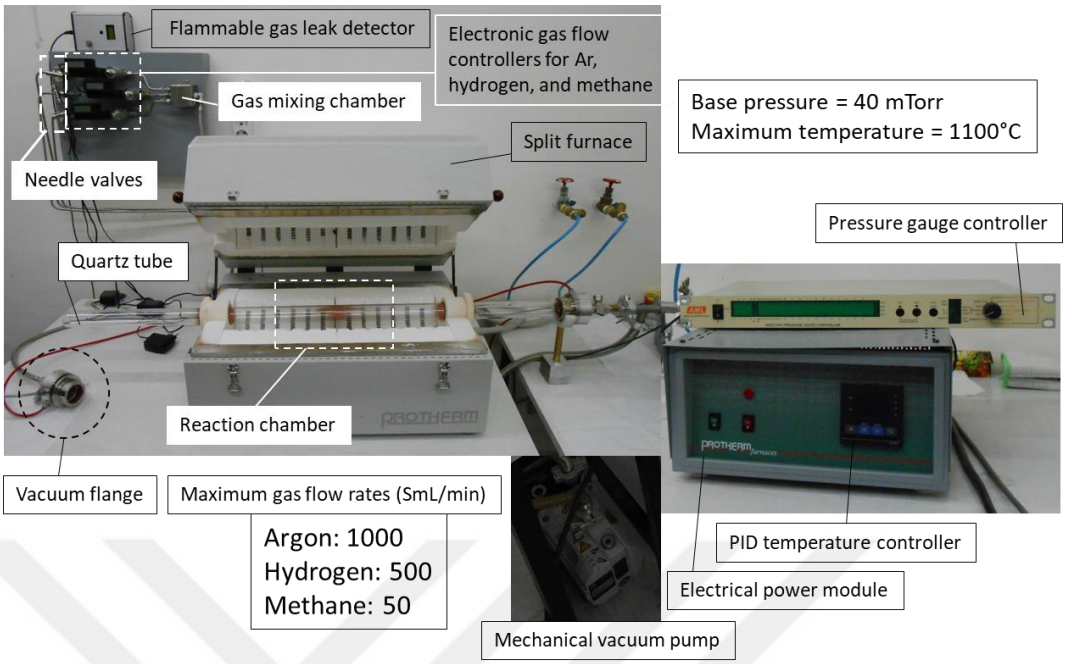

Figure 3.8. Hot-wall CVD system used for graphene growth. Gas cylinders are behind the wall. Vacuum flanges are cooled with chiller.

Before using the copper foil as a catalyst to synthesize graphene via APCVD, it must be cleaned. To this end, first, two strips of foil were flushed with acetone and then immediately dried with flow of nitrogen gas, thereby removing organic contaminants with acetone from the surface of the foil without any residual acetone, which could be a source of organic contamination per se. Thereafter, the foil strips were placed into the quartz tube of the CVD system by employing two flat quartz boats (the strips are of about the same sizes as those of boats). After the tube was sealed with vacuum flanges, the pressure inside the tube was reduced to $4x10^{-2}$ Torr, followed by the introduction of a large argon gas flow into the tube. Then hydrogen gas flow of 10 sccm was introduced and the regulator valve of the argon gas cylinder was closed. Next, the heating program of the split furnace was initiated after the argon gas flow ceased and the needle valve between the argon gas cylinder and flow controller was closed. The program, which is controlled by the PID controller of the furnace, sequentially consists of the following steps (Figure 3.9): ramping the temperature

around the boats up to 1000˚C in the presence of the hydrogen flow. During this step, hydrogen flow removes the native oxide layer on both surfaces of the foil and possible organic contamination, which can become additional nucleation sites, decreasing the average grain size of the graphene. Graphene growth for 35 min was provided by the inclusion of methane gas flow of 15 sccm while the temperature was maintained at 1000 °C by the PID controller. At the end of the growth step, the lid of the furnace is immediately opened for starting fast cooling. The methane flow was stopped when the temperature decreases to 650˚C and the hydrogen flow was sustained until it went down to 150˚C to prevent the oxidation of graphene [93] and to etch small multi-layered regions. During the growth, the hydrogen flow is important for controlling the nucleation rate and graphene grain growth rate, which are both crucial for maximizing the uniformity, average grain size and surface coverage of graphene.

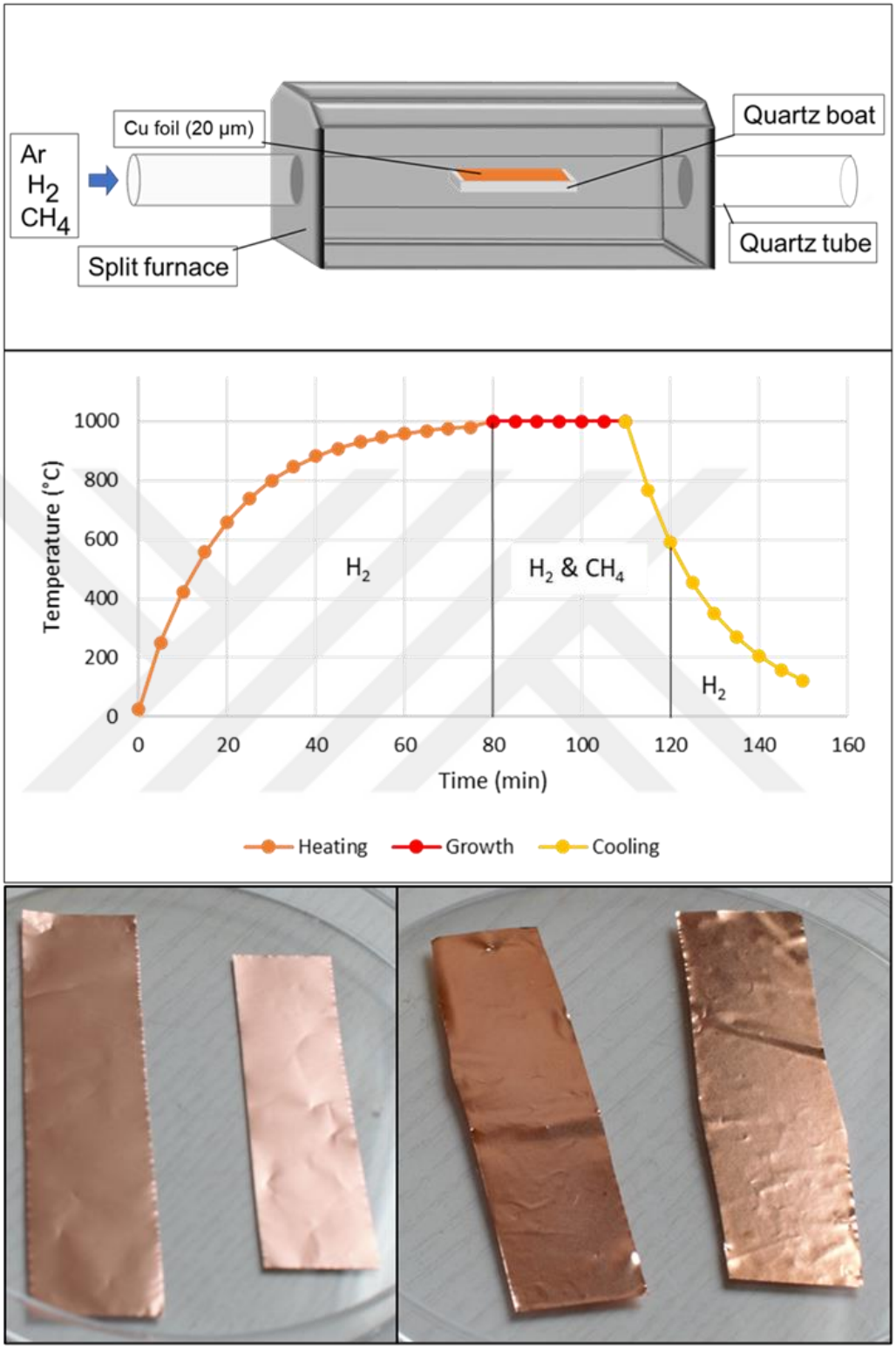

Figure 3.9. Top: Schematic for the CVD system. Middle: Graphical representation of the CVD process. Bottom: Cu strips before (left) and after (right) CVD.

Ideally, CVD growth of graphene on copper is a self-limiting process due to low solubility of carbon in copper, i.e., the growth is expected to stop after the full coverage of the copper surface by a layer of graphene, which prevents further catalytic action of copper. However, since copper foil is polycrystalline, carbon atoms could accumulate at the grain boundaries and form multilayer patches. Therefore, we should say that the outcome of the process is mostly composed of single layer graphene. For this work, we used only the graphene grown on the smooth side of the foil.

Before transferring the graphene, we characterized it on the copper foil via Raman spectroscopy (Laser wavelength = 532 nm). Despite the low signal-to-noise ratio due to the high reflectance and roughness of the copper surface, characteristic peaks D, G, and 2D of graphene can be discerned in the spectrum (Figure 3.10). Nevertheless, one needs to transfer graphene from copper to SiO_2/Si for determining the peak positions, intensities, and widths more accurately.

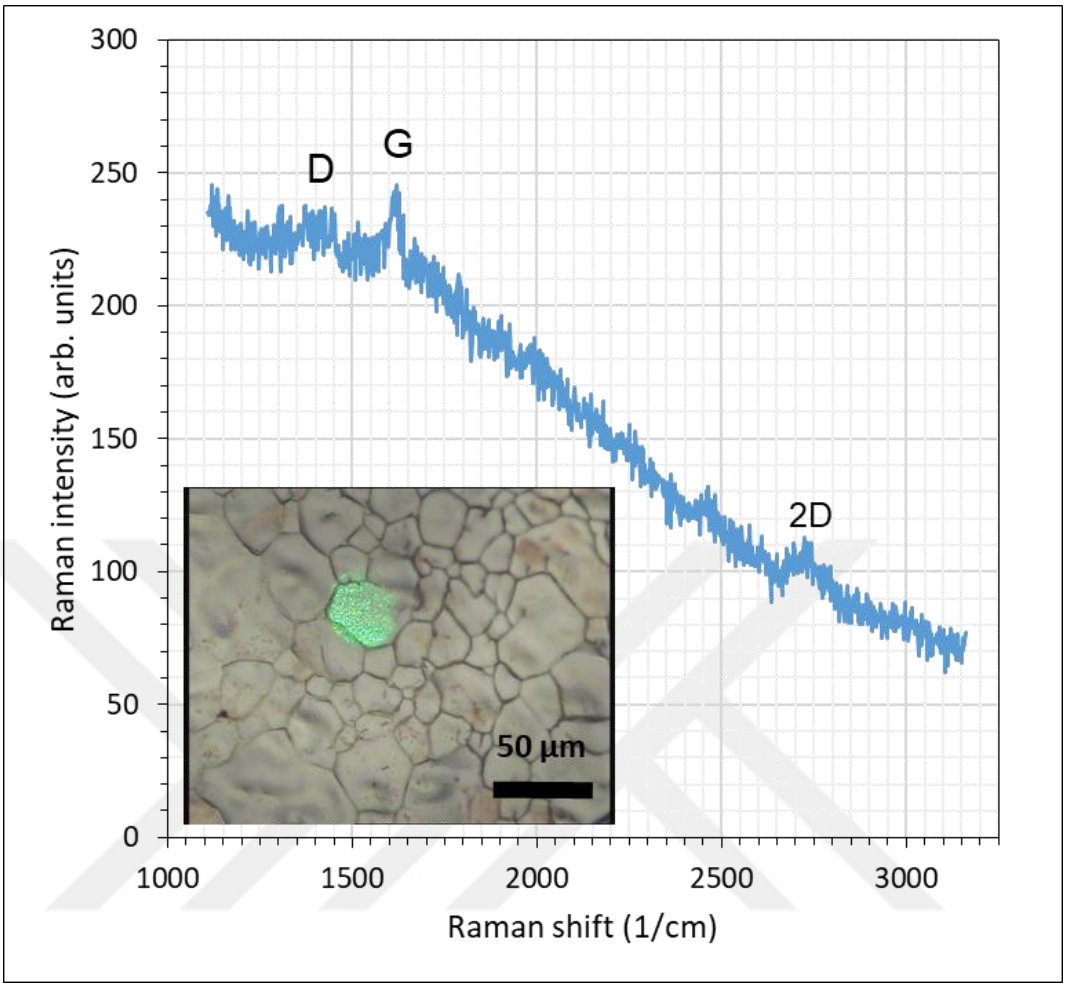

Figure 3.10. Raman spectrum of the CVD-graphene on the copper foil. Three characteristic peaks are discernable. Inset shows the optical microscope image of the graphene-coated surface of the copper foil with the laser spot of the Raman system. Copper grains can be seen. Laser wavelength = 532 nm.

The CVD-graphene was characterized with Raman spectroscopy after having been transferred onto 300nm-thick-SiO_2/Si by performing the process, originally developed by Polat and Kocabas [94], that involves the following steps (Figure 3.11):

1. Drop-coating a thick layer of photoresist (AZ5124 or S1813) on the surface of the copper bearing graphene to be transfer-printed.
2. Soft baking the photoresist in a preheated oven at 70°C for 12 hours.

3. Placing the sample on an aqueous ferric chloride [$FeCl_3$(aq)] solution for entirely etching the copper.
4. Cleansing the graphene-bearing side of the photoresist layer with DI water.
5. Fishing the graphene-bearing photoresist out of the water with a piece of the Si wafer.
6. Drying the photoresist/graphene/SiO_2/Si sample with N_2 gas flow.
7. Baking the sample at 80°C on hot plate for 2 minutes.
8. Baking the sample at 120°C on hot plate for 2 minutes.
9. Immersing the sample in acetone for removing the photoresist.
10. Rinsing the sample sequentially with acetone, IPA, and DI water.
11. Drying the sample with N_2 gas flow.

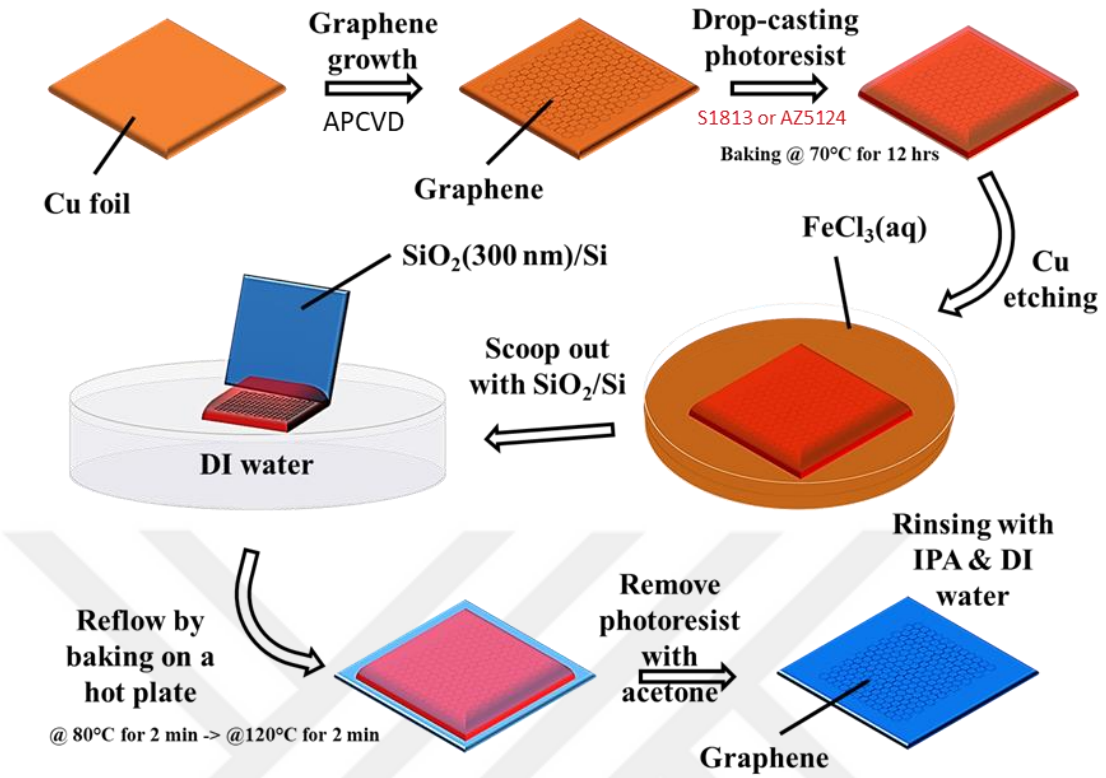

Figure 3.11. Schematic description of process for transfer-printing graphene onto SiO_2/Si wafer.

The Raman spectroscopy of the graphene transferred onto the SiO_2/Si wafer enabled us to perform a detailed analysis of the characteristic peaks of the Raman spectrum of graphene (Figure 3.12), thereby facilitating the characterization of the output of our CVD process.

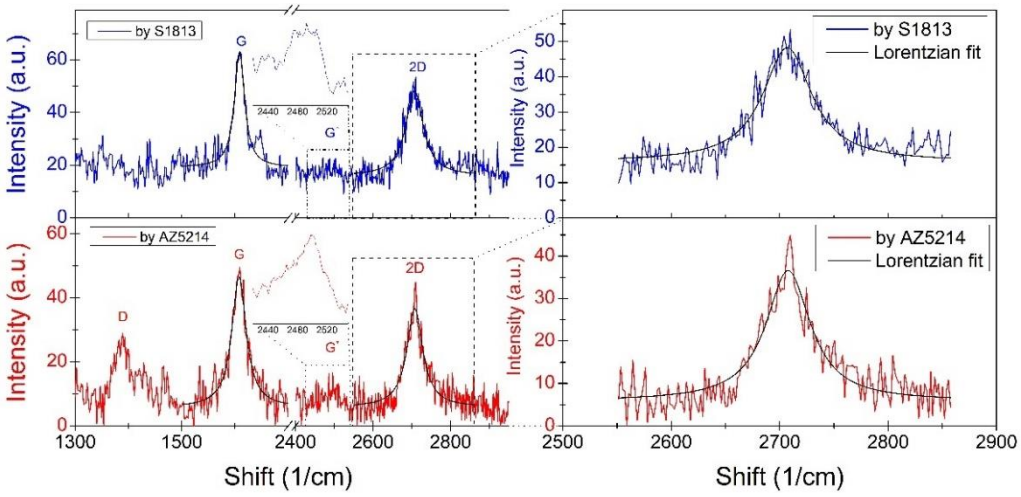

Figure 3.12. Raman spectra of the CVD graphene transferred onto 300nm-thick-SiO2/Si wafer with superposed Lorentzian fits on G and 2D peaks. Insets show smoothed G* peaks. The graphene sample transferred by AZ5214 is much more defective than that transferred by S1813, according to the heights of the D peaks [83,89]. In the right side, the magnified 2D peaks are shown with the superposed Lorentzian fits. That the 2D peaks can be fitted well with single Lorentzians indicates the existence of single-layer graphene although $I_{2D} / I_G < 1$, where 'I' denotes the intensity [1,20]. However, it was shown that I_{2D} / I_G depends on the doping level of graphene [85]. $I_{2D} / I_G \approx 0.76$ and 0.75 for the graphene transferred by using AZ5214 and S1813, respectively (Table 3.1), which could be resulted from water- and photoresist-induced hole doping levels of ~$3x10^{13}$ cm^{-2} [1,85,87]. This hole concentration also could yield Raman shifts of ~1610 and > 2700 cm^{-1} [85], thereby explain the G and 2D peaks except for the full width at half maximum (FWHM) of the G peaks (Table 3.1), which, contrary to the FWHM of the 2D peak, decrease with increase in the doping concentration [85]. Additional increase in the FWHM of the G peak could be attributed to the strain induced by the photoresist-assisted transfer process (Figure 3.11). Insets show G* peaks smoothed by using the Savitzky-Golay filter with 20 points of window. The sharpness of the G* peak of the sample transferred by AZ5214 indicates the existence of single-layer graphene, while the shape of the other suggests the possibility for the existence of few-layer graphene [83].

Table 3.1 G and 2D peak positions, heights and FWHMs for the graphene samples transferred by using AZ5214 (red) and S1813 (blue).

Peak	*Shift (1/cm)*	*Intensity (a.u.)*	*FWHM (1/cm)*
G	1608	41	33
G	1609	44	23
2D	2708	31	50
2D	2707	32	55

Except for the Raman study, we focused on transferring graphene onto flexible substrates. We chose standard commercially-available lamination film, which is basically EVA-coated PET film, as the target substrate. By using a laminator, we directly transferred graphene from the copper foil onto EVA layer of the lamination film, as described in Figure 3.4. During the lamination, EVA layer softens and thus conformally contacts with the graphene on the copper foil, thereby giving rise to adhesion between graphene and EVA and making the transfer possible after dissolving the copper layer of the resultant laminate. Optical microscopy showed that the topography of the surface of the copper foil was imprinted in the EVA layer (Figure 3.13). After transferring CVD-graphene onto this flexible substrate, we made devices out of the resultant structure and characterized graphene on the flexible substrate. The following two chapters are to present the experimental process in detail.

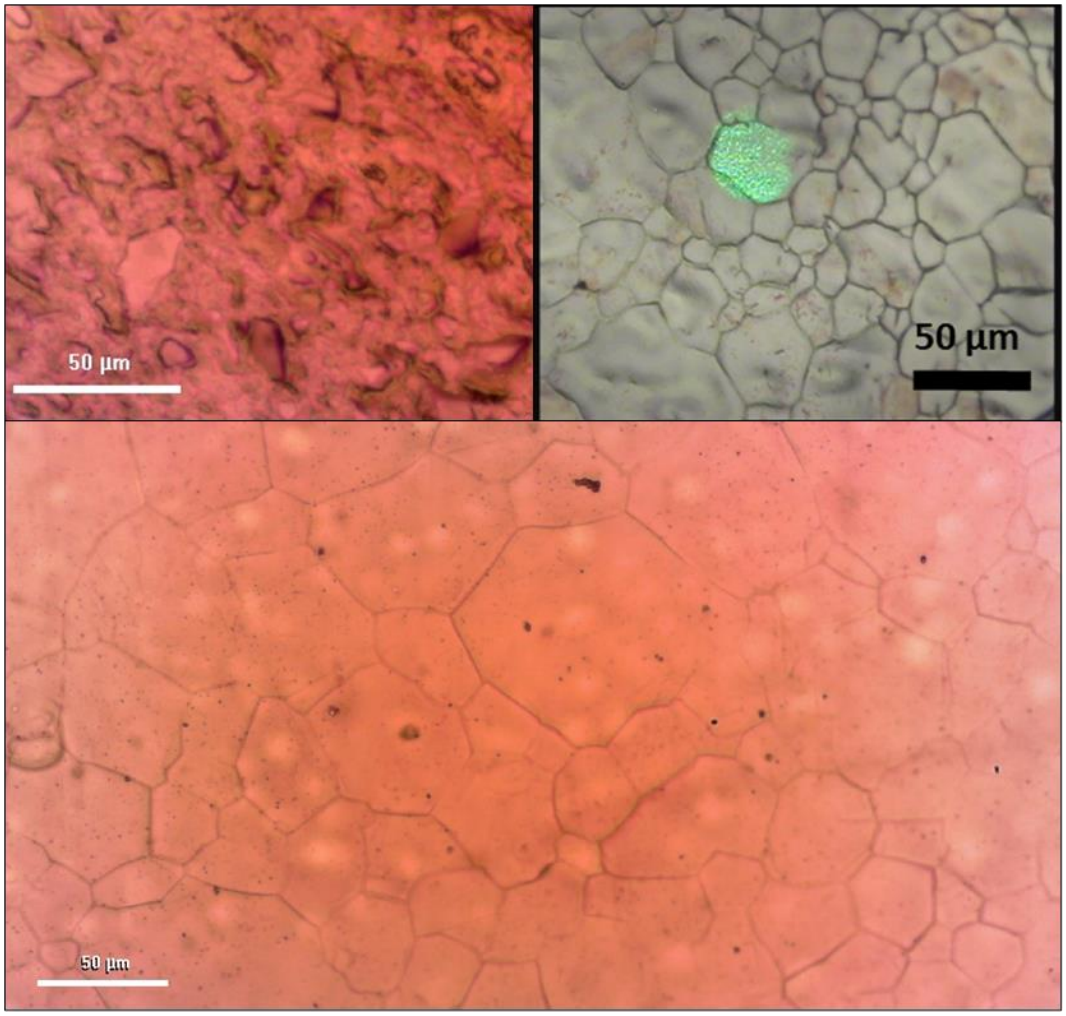

Figure 3.13. Top: Optical microscopy images the surface of the EVA layer of the lamination film before the lamination with graphene-carrying copper foil (left) and of the surface of the copper foil after the CVD process (right). Bottom: Optical image of the surface of the EVA layer after the lamination.

CHAPTER 4

GRAPHENE-BASED HALL-EFFECT DEVICES ON FLEXIBLE SUBSTRATE

Since graphene's isolation and electronic characterization by Novoselov *et al.* [1], it has been evident that it is an ideal material for the fabrication of ulta-high-performance Hall-effect devices. Graphene features excellent properties for a material to be utilized for fabricating a Hall-effect device. Being a zero-overlap semimetal or a gapless semiconductor with a conical band structure around the charge neutrality point and having charge carriers with ultra-high mobility [11], its electrical conductance does not vanish even if the density of its charge carriers becomes vanishingly small [1]. Therefore, it is possible to make Hall sensors with ultra-high sensitivities based on graphene [2]. Its great potential in this application area has already been experimentally realized. In 2011, Tang *et al*. published a work involving the characterization of a micro-Hall probe fabricated based on CVD-graphene over the temperature range from liquid Helium to room temperature, yielding Hall sensitivities ~310-1200 Ω/T, and suggesting applications in scanning Hall-probe microscopy (SHPM) [95], which was realized afterwards by Sonuşen *et al*. [96]. Graphene-based Hall probes (GHP) not only has the potential to surpass the conventional Hall probes in Hall sensitivity and signal-to-noise ratio, but also in nanolithographical processability: etching graphene is much easier, and it is possible to fabricate graphene Hall elements much smaller than those based on the conventional materials and thereby increasing spatial resolution of the Hall probe further, without decreasing its figures of merit [95–97]. Moreover, the vertical distance between the probe and the object to be probed could be reduced more than it is possible with the conventional probes since graphene is a two-dimensional material, bearing naturally-occuring two-dimensional electron gas (2DEG) [98]. Before its application in SHPM, Xu *et al*. had already published their work on the batch-fabrication of high-performance CVD-graphene-based Hall elements with current-

related sensitivities exceeding 550 Ω/T [99]. Also, Panchal *et al*. fabricated Hall sensors out of graphene epitaxially grown on SiC and obtained current-related sensitivities reaching 790 Ω/T [98]. In search of the performance limit of the Hall elements fabricated out of CVD-graphene, Huang *et al*. [100] and Chen *et al*. [97] obtained the current related sensivities of up to 2093 and 2745 Ω/T, respectively, approaching that of the devices based on the state-of-the-art III-V semiconductor heterostructures, although the graphene-based Hall element (GHE) was not encapsulated. Encapsulation is crucial for making use of the full potential of graphene in electronics because the adsorption of ambient molecules could reduce the mobility, increase the noise, undermines the stability, and shorten the lifetime of the device [101–103]. Dauber *et al*. showed the full potential of graphene in this area of application by sandwiching graphene, which was obtained by mechanical exfoliation, between two-dimensional hexagonal Boron Nitride (hBN) sheets and managed to achieve current-related sensitivity of up to 5700 Ω/T, outperforming the state-of-the-art Hall sensor devices based on III-V semiconductor heterostructures [104]. Although graphene's sensitivity of ambient adsorbants appears disadvantageous up to this point, it can be utilized to detect particles in a controlled environment with a proper surface functionalization: since the current-related Hall sensitivity is inversely proportional to the sheet charge density ^{2}, graphene-based Hall-effect devices provides a platform for fabricating highly sensitive particle detectors [105,106]. Motivated by the above-mentioned properties and superior mechanical [107] properties of graphene, we aimed to discover its potential for fabricating flexible Hall-effect devices by manufacturing cross-shaped Hall-effect devices with CVD-graphene transferred onto PET film.

4.1 Manufacture

We manufactured the devices by transfer-printing graphene grown via APCVD described in Section 3.2 as in the following process flow (Figure 4.1):

1. A graphene-bearing copper strip is placed on a sheet of paper. The graphene on the upper side of the strip is to be transfer-printed.
2. A piece of EVA/PET is cleaned by flushing with isopropyl alcohol followed by an immediate fast drying with nitrogen blow.
3. The piece of EVA/PET sheet is laid over the strip so that the graphene layer and EVA layer will be on contact with each other.
4. The PET/EVA/graphene/copper/graphene/paper stack formed at the previous step is laminated at the temperature of ~125°C.
5. The graphene/copper/graphene/EVA/PET laminate produced at the previous step is cut into the device shapes, including their Hall crosses and copper contact pads to be formed at the end.
6. Parts of the copper layers of the piece cut out of the laminate are painted with a permanent marker having a waterproof ink to form electrical contact pads of the device.
7. The painted piece is placed on the surface of an aqueous ferric chloride ($FeCl_3$) solution in order that the unpainted part of the piece is dissolved into the solution. The parts of the copper layer painted in the previous step will be protected by the waterproof ink during the dissolution.
8. The product obtained at the previous step is gently dried with nitrogen blow.
9. By gently scratching the dried ink layers with a scalpel, the cross-shaped Hall-effect device has been manufactured and made ready for electronic characterization.

By applying the process flow explained above, we manufactured two sets of cross-shaped Hall-effect devices with two different Hall-cross dimensions (Figure 4.1).

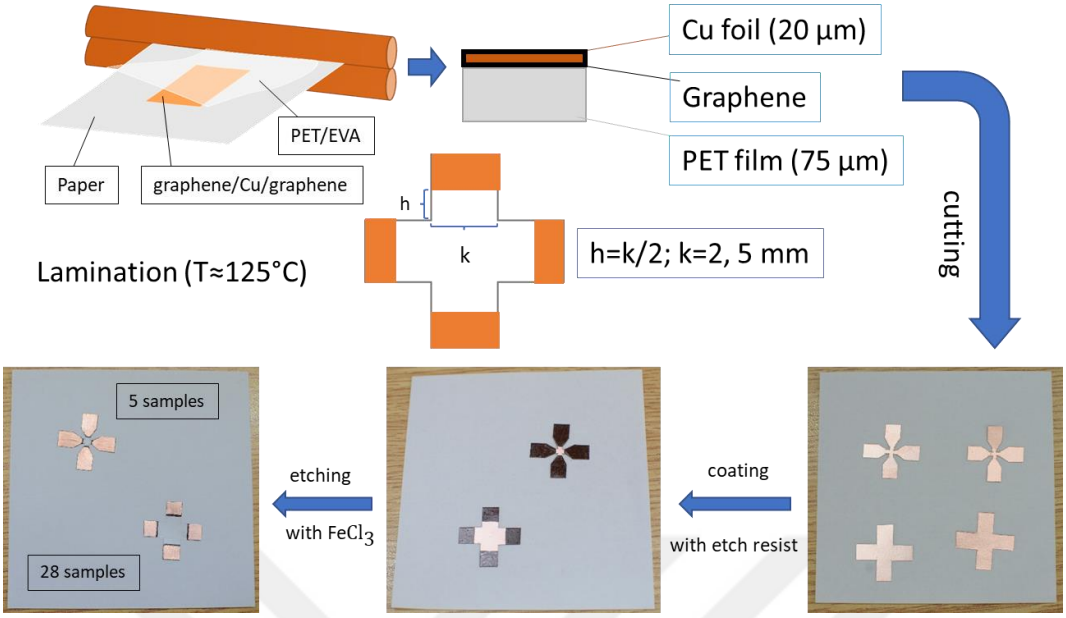

Figure 4.1. Schematics for the process flow of the manufacture. Black parts are the parts of the copper layer covered with waterproof ink, which acts as an etch resist during the wet etching with $FeCl_3$(aq). Two sets of devices with different Hall-cross sizes manufactured. 5 devices with smaller Hall-cross were manufactured. The other set contains 28 devices.

4.2 Characterization

Firstly, the series resistances of the devices were measured. Characterization of Hall-effect devices as magnetic sensors requires the measurement of the voltage between the sense contacts (Hall voltage), as sensor output, with respect to the intensity of the magnetic induction perpendicular to the surface of the conducting layer of the device, sensor input, after maintaining a constant bias current through the other arms of the device [2]. To this end, we used a Hall-effect measurement system (NanoMagnetics HEMS) equipped with an electromagnet capable of creating uniform magnetic induction with intensities of up to 8000 G, between its poles (Figure 4.2). By employing a specially made sample holder, the device was inserted

between the poles in order that the magnetic induction would be perpendicular throughout to the graphene-based conducting layer of the device. After maintaining a bias current, the Hall voltage V_H was measured for each magnetic induction B value resulted from sweeping the magnetic induction from one direction to the other along its axis. In addition, the series resistances of the devices were measured after removing the sample holder from the magnetic field.

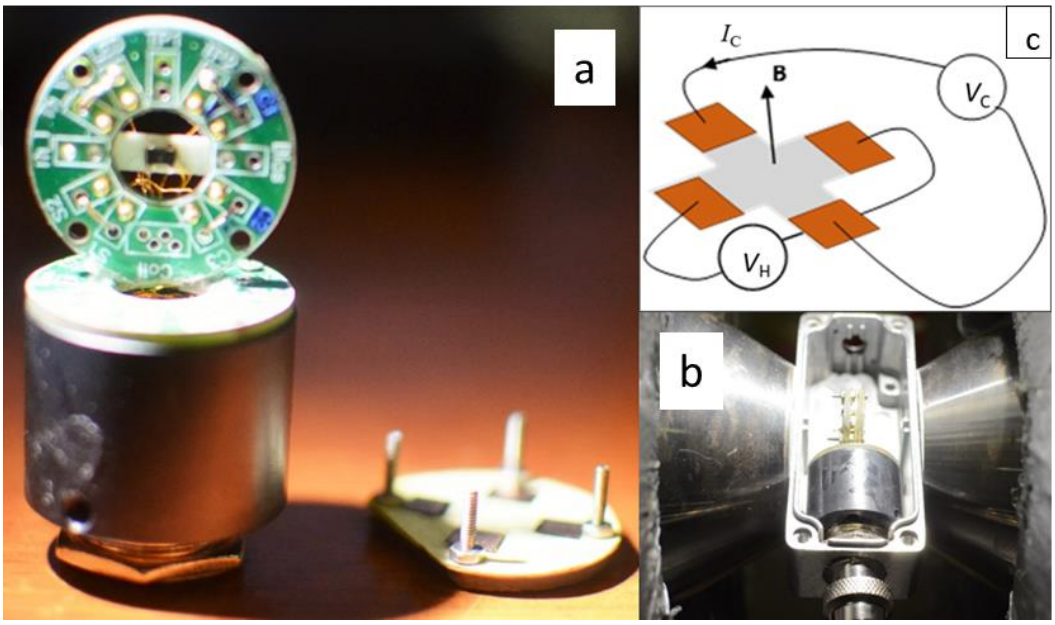

Figure 4.2. (a) Sample holder. (b) Sample holder with a device inserted into its case, fixed between the poles of the electromagnet, and connected to the electronics of the HEMS. (c) Schematics of the four-probe Hall-effect measurement. The magnetic induction is to be perpendicular throughout the graphene layer.

The series resistance measurements showed ohmic behavior and Hall-effect measurements showed the linear sensor response of the devices with respect to the magnetic induction (Figure 4.3). The absolute sensitivity of the Hall sensor is given by the slope of the linear fit to the data points of the V_H-vs-B graph, and the current-related sensitivity of the Hall sensor equals the absolute sensitivity divided by the

bias current [2]. It was measured for the bias currents of 100 μA, 300 μA, and 500 μA (Figure 4.4).

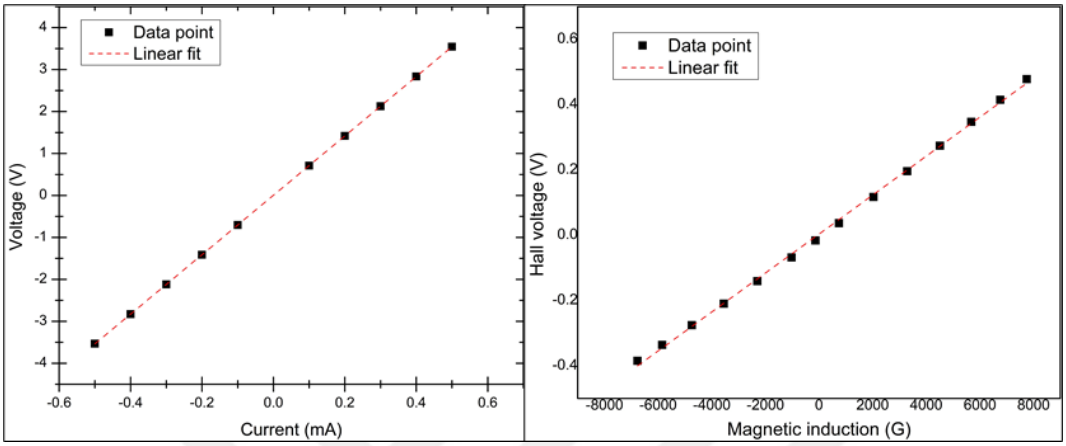

Figure 4.3. Exemplary graphs stemmed from the I-V and Hall effect measurements of one of the devices, corresponding to the series resistance of ~7 kΩ and current-related Hall sensitivity of ~1000 Ω/T. A bias current of 0.1 mA was applied for the Hall-effect measurement.

Owing to its four-fold symmetry, cross-shaped Hall-effect devices, sense contacts and current contacts are interchangeable. The series resistance measurements of the devices involved measuring resistances between possible current contacts. The measurements resulted in a distribution between extreme values 3.8 and 27.2 kΩ, with mean value 8.4 kΩ and standard deviation 6.4 kΩ, which was fitted with a gaussian (Figure 4.5).

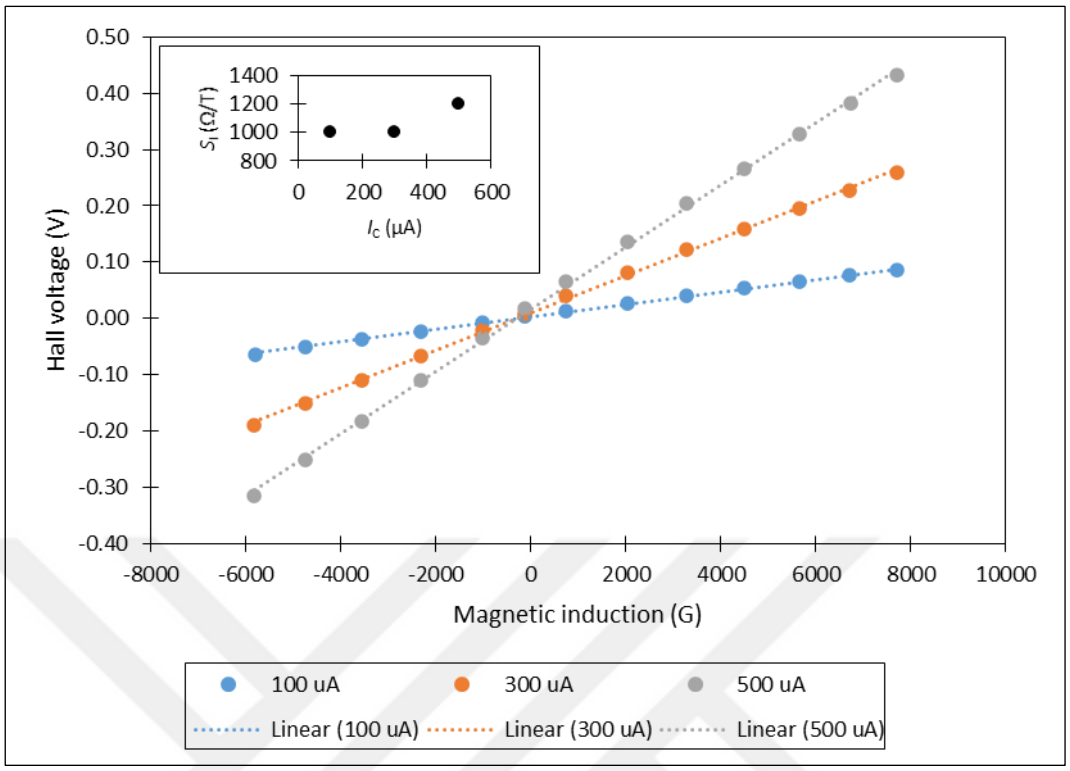

Figure 4.4. Plotted data resulted from the Hall-effect measurement of the device mentioned in Figure 4.3, for the bias currents of 100, 300, and 500 μA. Absolute sensitivity of the device is given by the slope of the linear fit. Inset shows the current-related sensitivity S_I for the bias currents.

Current-related sensitivities of the devices were obtained from the Hall-effect measurements. Furthermore, the charge carrier type was found as holes by checking the relative directions of the Hall electric field, indicated by the polarity of the sense contacts, bias current, and magnetic induction, as explained in Section 2.2. The hole density is given by the equation $n = G\,(S_I\,e)^{-1}$, where n, S_I, e, and G represent two-dimensional charge carrier density, current-related Hall sensitivity, elementary charge, and the geometrical correction factor, respectively [2]. Because of the geometry of the device (h = k/2) (Figure 4.1) and the graphene's high mobility (μ ≈ 1000 $cm^2/(Vs)$), which makes the Hall angle $\Theta_H \approx \arctan(\mu B) \approx \pi/2$, G ≈ 1 and thus

$n \approx (S_I e)^{-1}$ [2]. Figure 4.6 shows histograms of the results with corresponding Gaussian fits.

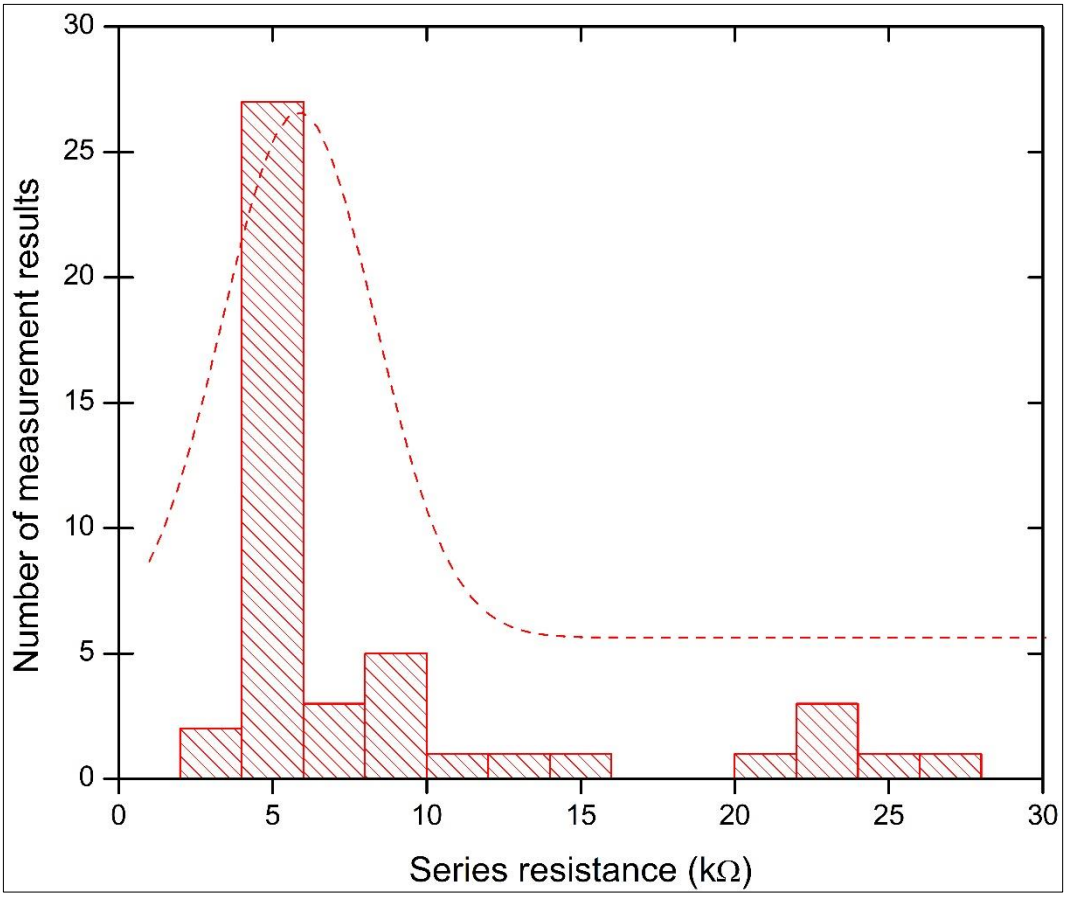

Figure 4.5. The histogram of the series resistance measurements of the devices with larger Hall cross. Dashed curve is a gaussian fit. The minimum and maximum values, mean value and standard deviation are 3.8 and 27.2, 8.4 and 6.4 kΩ, respectively.

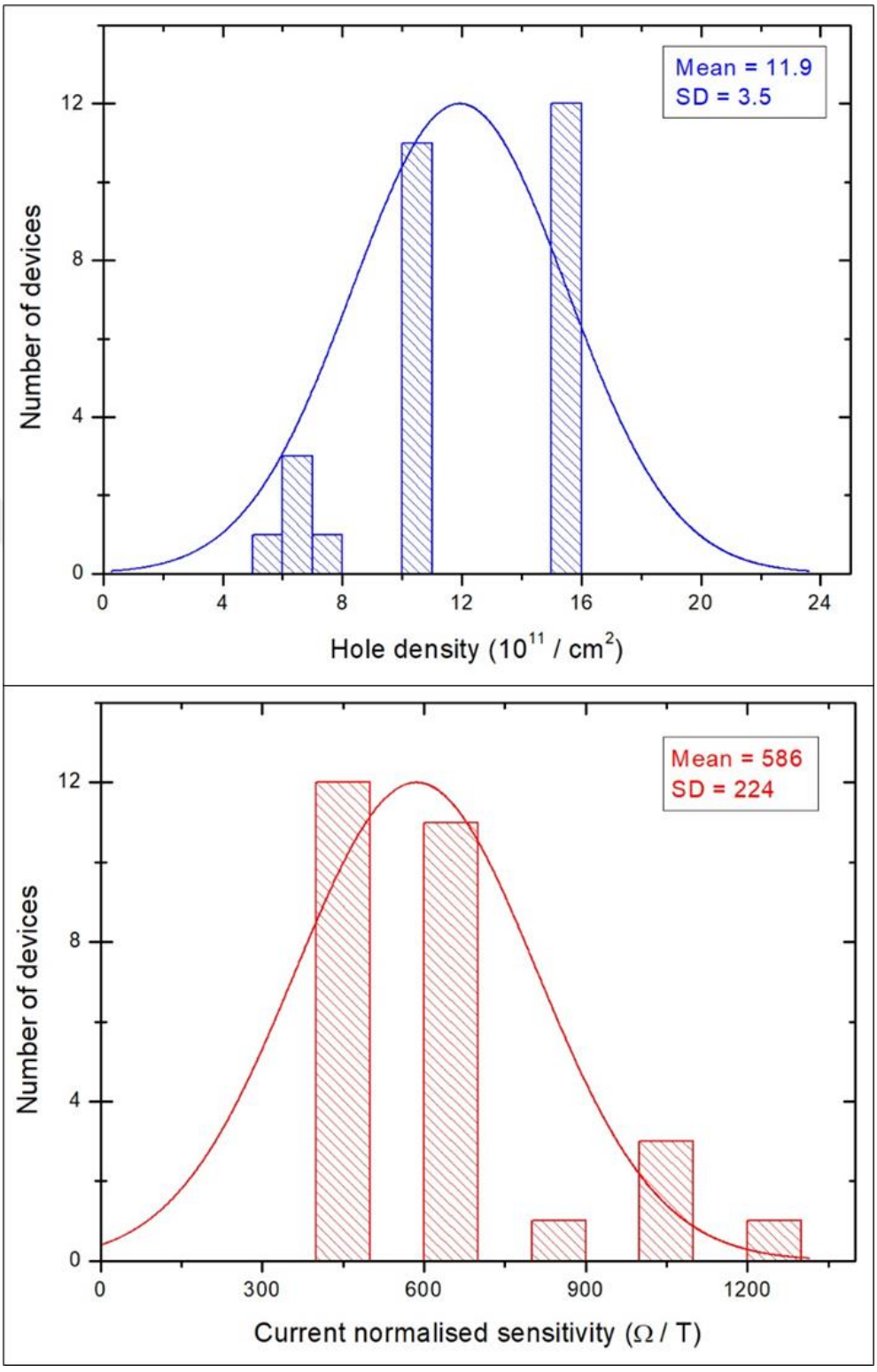

Figure 4.6. Histograms of the Hall-effect measurement results pertaining to the devices with the larger active area. Curves are gaussian fits.

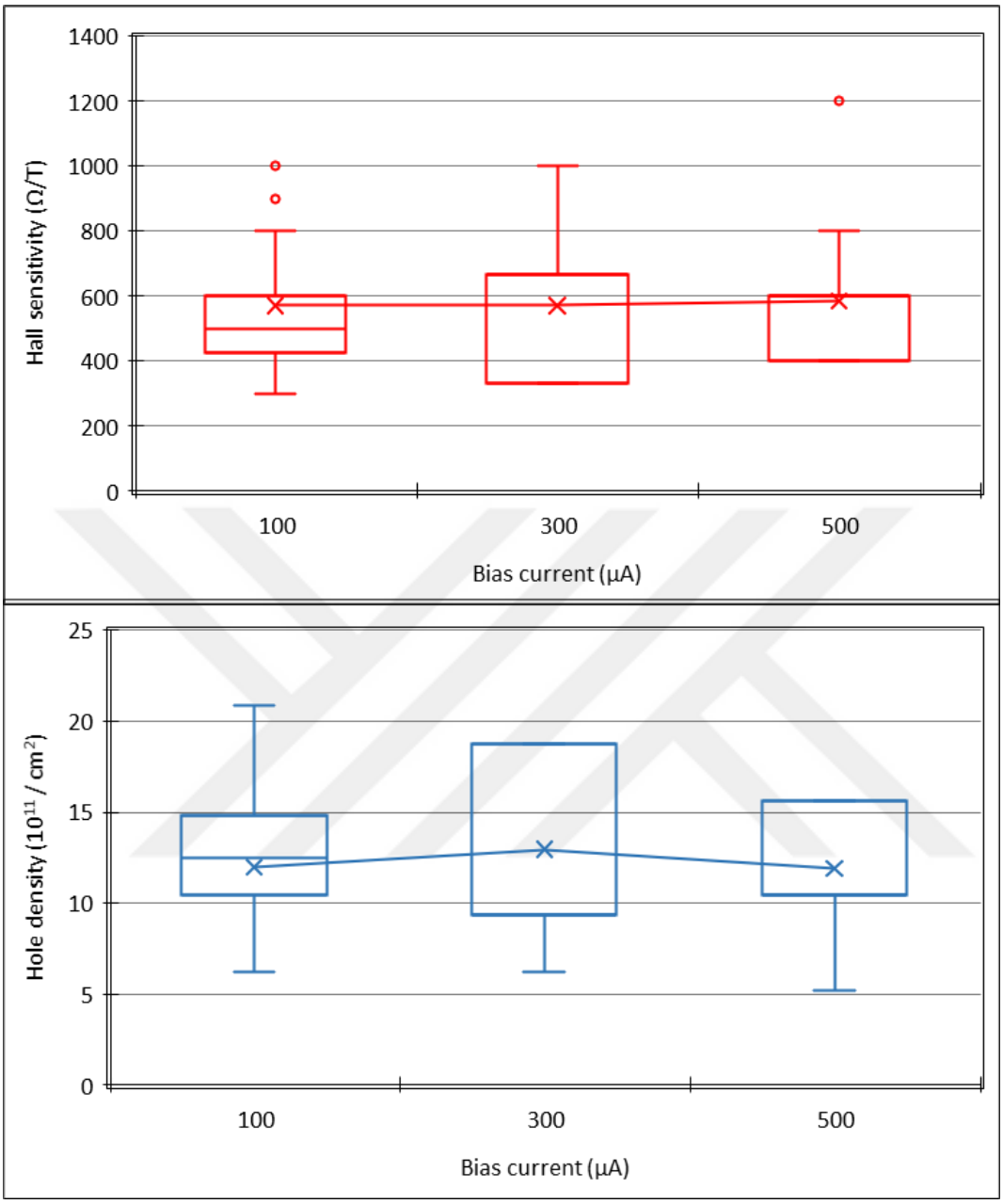

Figure 4.7. Box plots of the Hall sensitivity (top) and hole density (bottom) of the devices with the larger active area.

For an applied bias-current I and environmental conditions specified by parameters such as temperature, humidity, and pressure, to apply Hall-effect devices as magnetic sensors, it could be useful to assess the proportionality between the Hall voltage V_H

and the component of the magnetic induction perpendicular to the device, *B*. To that end, the degree of the proportionality can be quantified by defining a figure of merit called non-linearity (NL), which is a function of *I* and *B*, with the following equation:

$$NL = \frac{V_{\mathrm{H}} - V_{\mathrm{HL}}}{V_{\mathrm{HL}}} \qquad \text{(Equation 4.1)}$$

where V_{HL} represents the best linear fit to the data points resulted from the Hall-effect measurements [2]. By definition, $V_{\mathrm{H}}(0) = 0$ [2].

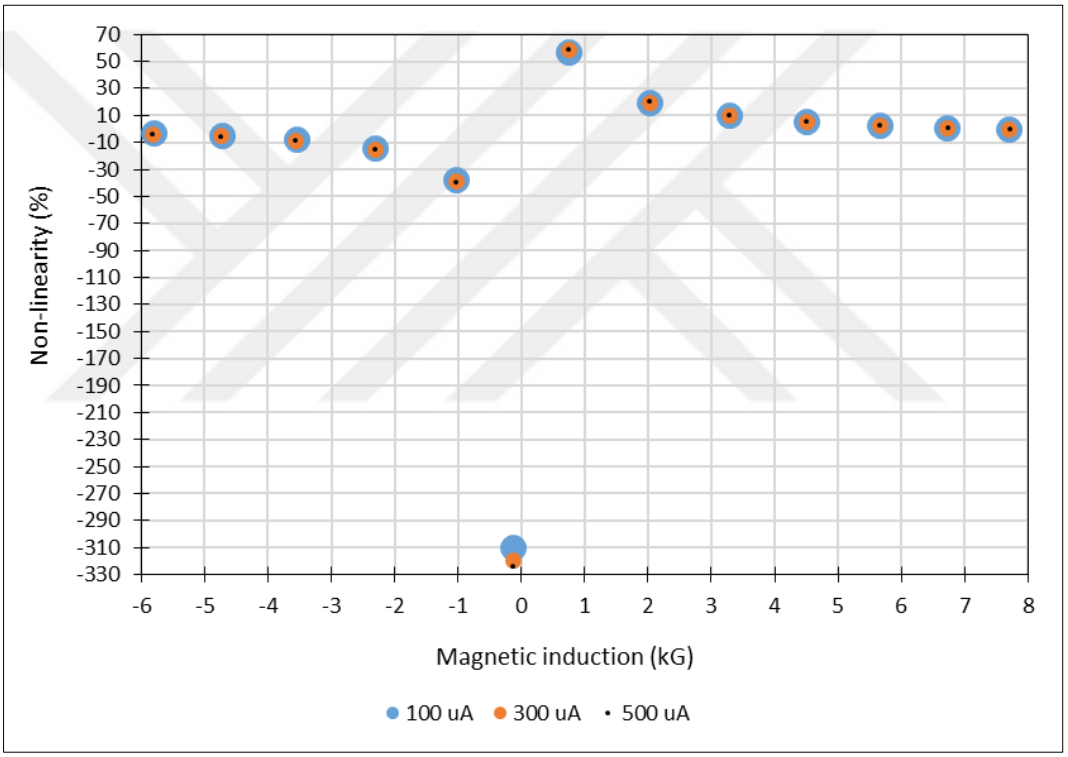

Figure 4.8. Non-linearity extracted from the data plotted in Figure 4.4, with respect to magnetic induction, for bias currents 100, 300, and 500 μA.

The device with plotted Hall-effect measurement data in Figures 4.3 & 4.4 was found to have non-linearity between -30% and +30% for magnetic induction values larger than 2 kG and between -10% and +10% for magnetic induction values larger than 3

kG, for bias currents 100, 300, and 500 μA (Figure 4.8). Large nonlinearities of up to 324% for magnetic induction less than 1 kG must have caused by the off-set voltage, which is due to the misalignment of the sense contacts, resulting in a voltage difference between them as a bias current is applied. This is evidenced by the data: for the bias currents of 100, 300, and 500 μA, the magnetic induction of -0.133 kG resulted in the voltages of 3.1, 9.8, and 16.7 mV between the sense contacts. This consistent reversal of the sign of the voltage clearly indicates an off-set voltage.

The Hall-effect measurements of the devices with the smaller active area (Figure 4.1) resulted in the current-related sensitivities varying between 400 and 700 Ω/T, implying two-dimensional hole concentrations ranging from 8.92×10^{11} to 15.6×10^{11} cm^{-2} (Figure 4.9). The average values for the sensitivity and hole density are 540 Ω/T and 11.5×10^{11} cm^{-2}, which are close to and approximately equal to those of the other set of devices, respectively (Table 4.1).

Table 4.1 Average values and standard deviations for the two-dimensional hole densities (p) and current-related sensitivities (S_I) pertaining to the two sets of Hall-effect devices with active areas of 2x2 and 5x5 mm^2. The average value and standard deviation are denoted by an overbar and σ, respectively.

Active Area (mm^2)	$\overline{p}$ ($10^{11}/cm^2$)	$\overline{S_I}$ (Ω/T)	σ(p) ($10^{11}/cm^2$)	σ(S_I) (Ω/T)
2x2	11.5	540	3.0	136
5x5	11.9	585	3.5	224

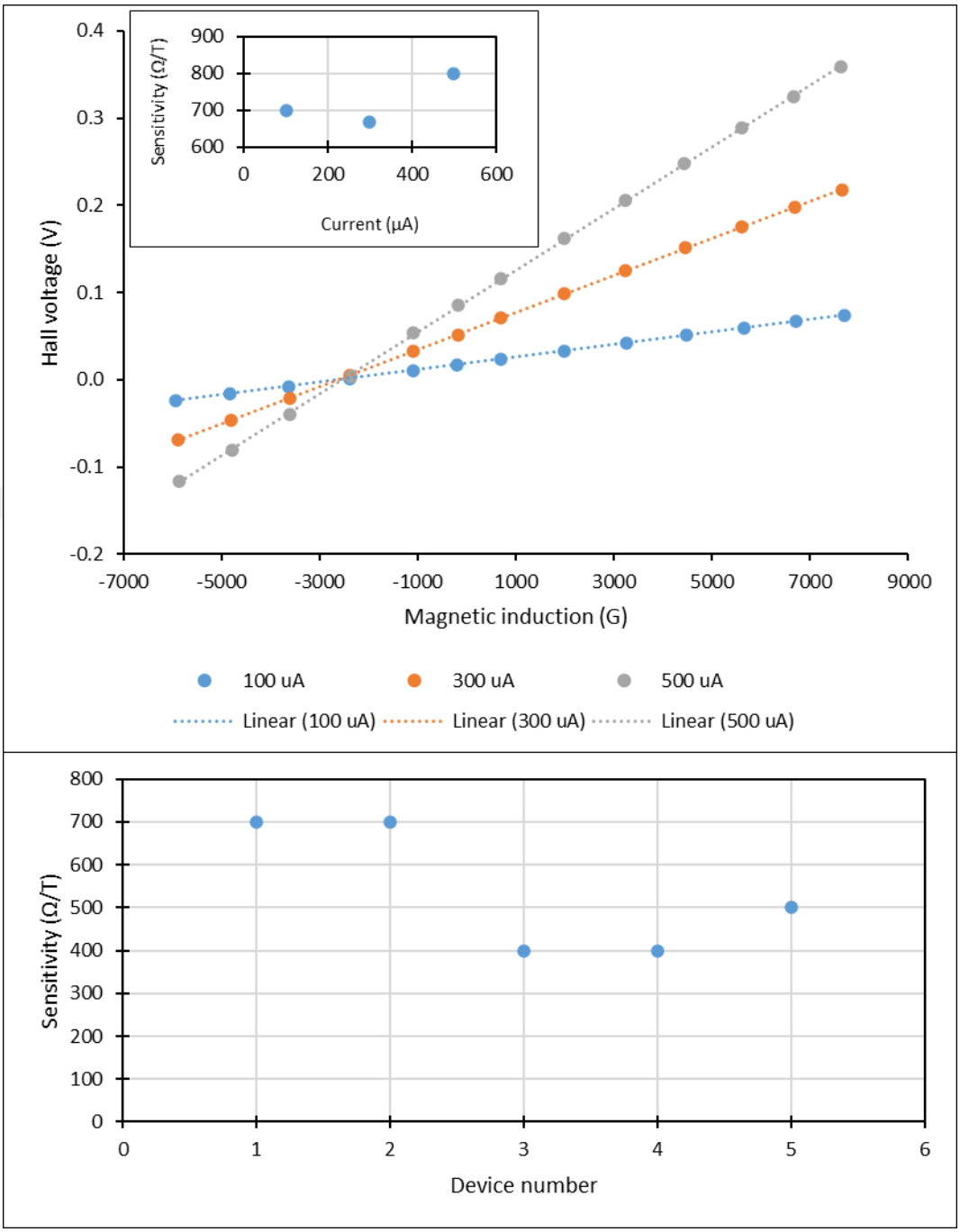

Figure 4.9. Upper: Hall-effect measurement results of one of the devices with smaller active area, for bias currents 100, 300, 500 μA (Inset shows change in the current-related sensitivity of the device with respect to the bias current.). Lower: Current-related sensitivities of all 5 of the devices with smaller active area.

CHAPTER 5

GRAPHENE-BASED MULTILAYERED CONDUCTIVE FILMS ON FLEXIBLE SUBSTRATE

Among all the metals hitherto used as catalysts for the synthesis of uniform graphene films via chemical vapor deposition (CVD), copper is the most promising: graphene growth on a polycrystalline copper foil is mostly self-limiting, i.e. stops after its surface is fully covered with graphene because of low carbon solubility in copper [108]. Because of the low carbon solubility, graphene growth on copper neither depends on the thickness of the copper foil nor requires any special consideration of the cooling rate of the CVD process, thereby making the process optimization considerably less complicated [108]. In addition, by employing the pretreatment to reduce the roughness of the copper foil and the annealing step, CVD of graphene on copper could be optimized to yield highly uniform, even large single crystal graphene [108,109]. However, CVD of single crystal multi-layer graphene on metal is a much more complicated process [108,109]. Therefore, considering the efficiency and reliability of the CVD of graphene on copper, artificially stacked graphene grown on copper could be an alternative route for fabricating devices based on multilayer graphene.

This chapter presents the manufacture process and characterization of the artificially stacked multi-layer graphene that we obtained via layer-by-layer lamination on EVA-coated polyethylene terephthalate (PET) film.

5.1 Manufacture

After synthesizing graphene via APCVD on the copper foil and cleaning the EVA/PET sheet as described in Section 4.1, our manufacture scheme basically consists of 5 steps, except for the step involving the fabrication of electrical contact pads: (i) a PET/EVA/graphene/Cu/graphene/paper stack is formed, (ii) this stack

passes between the hot rollers of the laminator after the temperature reaches 125°C, (iii) a sample in square or cross shape is cut out of the resulting PET/EVA/graphene/Cu/graphene laminate for van der Pauw or Hall sensitivity measurements, respectively, (iv) the copper layer is dissolved in an aqueous $FeCl_3$ solution, (v) the resultant graphene/EVA/PET laminate is placed on a larger piece of graphene-bearing copper foil in order to form a paper/PET/EVA/graphene/graphene/Cu/graphene/paper stack. The resulting stack is laminated as in step ii. A new sheet of graphene is transfer-printed onto the existing graphene layer in the graphene/EVA/PET laminate by etching the copper layer with an aqueous $FeCl_3$ solution. By iterating this cyclic process up to 10 times, we manufactured graphene-based conducting thin films on the EVA/PET and devices out of this structure. In order to obtain contact pads to be used in the electronic characterizations/applications of the thin films formed by iterating the process n times, the copper layer is selectively etched as described in Section 4.1 (Figure 5.1). By employing this scheme, we manufactured square-shaped van der Pauw samples and two sets of 4-contact cross-shaped Hall-effect devices. First set of the cross-shaped devices (Set 1) was resulted from transfer-printing graphene 1, 2, 4, 6, 8, and 10 times, and the second set of the devices (Set 2) obtained by additionally performing all the odd number of laminations skipped in preparing Set 1. The dimensions of the cross-shaped devices are the same as those presented in Figure 4.1. The triangular contact pads of the square-shaped van der Pauw samples at their corners were made as small as possible to obtain electronic characterization results as accurate as possible [8]. The edge length of the van der Pauw samples is 1 cm.

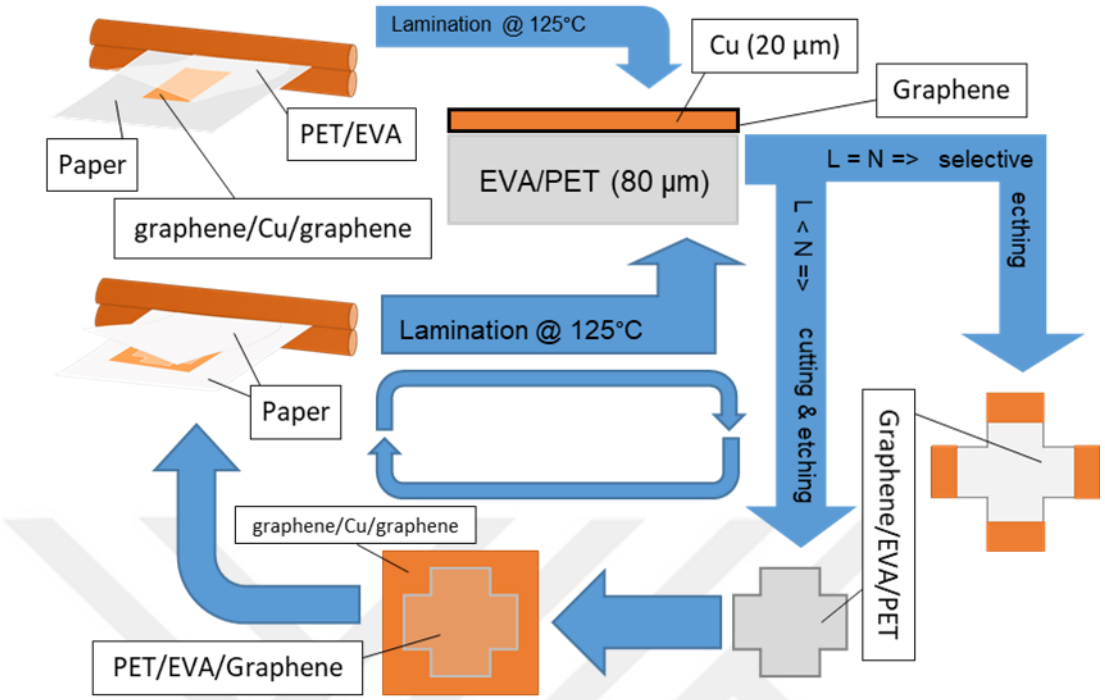

Figure 5.1. Schematics for the manufacturing process yielding conductive thin films on the EVA/PET via layer-by-layer transfer-printing graphene. Only the fabrication of the cross-shaped device shown, but we also manufactured square shaped samples with triangular copper contact pads at their corners. L and N denote the iteration number for the lamination and the desired number of laminations, respectively.

5.2 Characterization

Structural and electronic properties of the graphene-based conductive thin films were studied by using AFM and performing 4-probe van der Pauw and Hall-effect measurements. In addition, the Hall sensitivities of the Hall-effect devices made from the thin films were measured. AFM revealed both qualitative and quantitative changes in the surface of the thin film after each transfer-printing of graphene and van der Pauw and Hall-effect measurements showed the dependence of the mobility, sheet charge carrier density, and sheet resistance upon the number of graphene

transfer-printings performed to manufacture the thin film. Moreover, the charge carrier type and the sheet charge carrier densities were calculated by studying the directions of the bias current, magnetic induction, and the Hall electric field, and by using the Hall sensitivities, respectively [2]. Based upon the results of these characterizations, important information can be extracted considering possible applications of the conductive thin films.

5.2.1 Characterization with AFM

For this microscopic examination, special samples; with the size of 5x5 mm^2 were manufactured by transfer-printing graphene onto the EVA/PET from 1 to 10 times, and the surfaces of the resultant thin films were scanned at the rate of 10 μm/s with ezAFM of NanoMagnetics Instruments in dynamic mode using the PPP-NCLR cantilever of NANOSENSORS, whose free and set RMS values of oscillation were 100 nm and 50 nm, respectively. Scan areas were 2x2, 5x5, 10 x10 μm^2; PID parameters were 51-1-45 for the samples resulted from transfer-printing graphene 3, 5, 7, and 9 times, and 38-1-27 for the others, including the EVA/PET cleaned with IPA as described in Section 4.1 and the EVA/PET extracted by totally etching the copper layer after laminating the EVA/PET with the copper foil, denoted by P and P', respectively. As a result, we obtained the topographical images of the surfaces of the thin films as well as roughness values associated with each image (Figure 5.2).

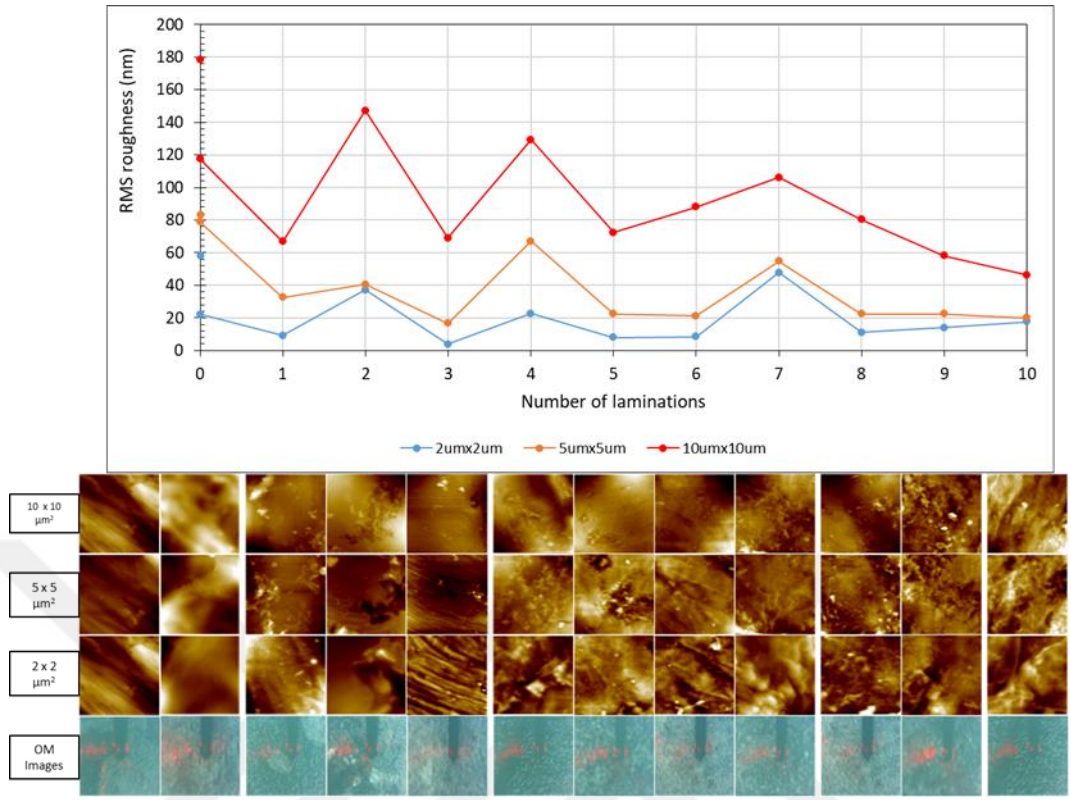

Figure 5.2. A mapping from an array of the AFM topographical images of the graphene-based thin film surfaces and EVA-coated surface of the lamination film to the RMS roughness, which appears to converge some value below 50 nm. Isolated points on the vertical axis represent the EVA-coated surface of the lamination film after laminating with the cleaned copper foil followed by wet etching the copper layer with aqueous $FeCl_3$ solution. They indicate ~50% decrease in the roughness of the copper foil as a result of the CVD process.

5.2.2 Electronic characterization

The cross-shaped Hall-effect devices in Set 1 and Set 2 were characterized via Hall sensitivity measurements by using NanoMagnetics Instruments' HEMS and ezHEMS, which were equipped with an electromagnet and permanent magnet, respectively.

For Set 1, first, a bias current was applied through the current contacts of the device after the sample holder of the HEMS had been placed between the poles of the electromagnet so that the surface carrying the bias current and the uniform magnetic induction **B** to be produced by the electromagnet would be perpendicular throughout to each other. Then, while the bias current was maintained, the voltage V_H between the sense contacts was measured for each magnetic field intensity value, determined by stepwise symmetrical sweep thereof from one direction of the magnetic field axis to the other, where $|\mathbf{B}| \leq 8000$ G (Figure 5.3). As a result, the current-related Hall sensitivity was calculated by dividing the slope of the linear fit, to the data points of the V_H-vs-**B** graph, by the bias current value, and also the non-linearity of the sensor response of the device, which was defined by (Equation 4.1, (Figure 5.4). The Hall sensitivity was calculated for the bias current values of 0.1, 0.3, 0.5, 0.7, 0.9, 1.0, 3.0, 5.0, 7.0, 9.0 mA. The computation resulted in the graph showing the dependence of the Hall sensitivity upon the bias current (Figure 5.5).

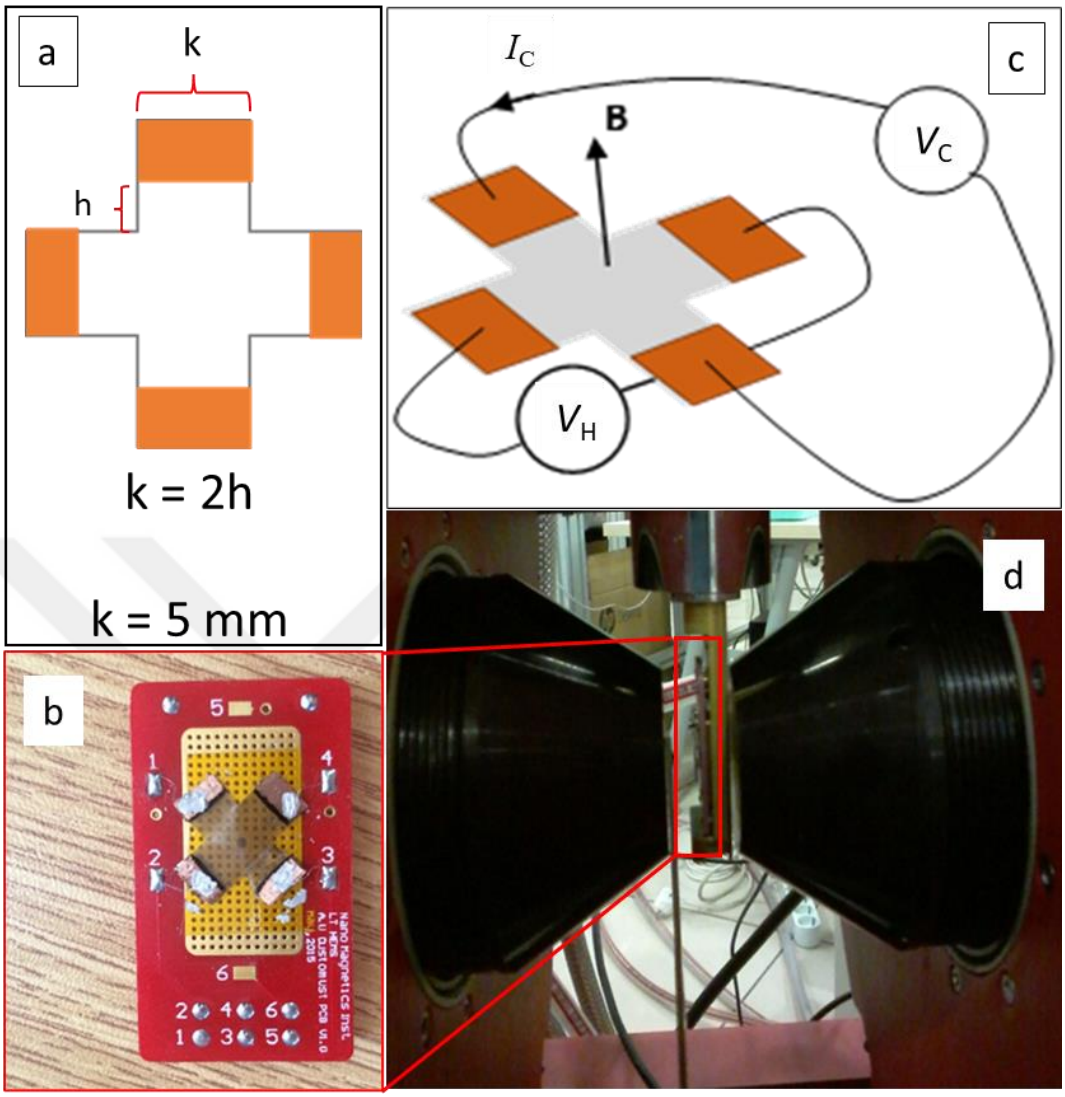

Figure 5.3. Setup for the electronic characterization of the cross-shaped Hall-effect devices Set 1. (a) Dimensions of the cross-shaped Hall-effect device. (b) the sample holder loaded with one of the devices connected to the electronics of the HEMS and placed between the poles of the electromagnet of the HEMS. (c) Schematics for the Hall-sensitivity measurements: the magnetic induction **B** created by the electromagnet is to be perpendicular throughout the surface of the device. After maintaining the bias current I_C is by applying the voltage V_C between the current contacts of the device, the Hall voltage V_H between the sense contacts is measured for each value of **B**. (d) The sample holder inserted between the poles.

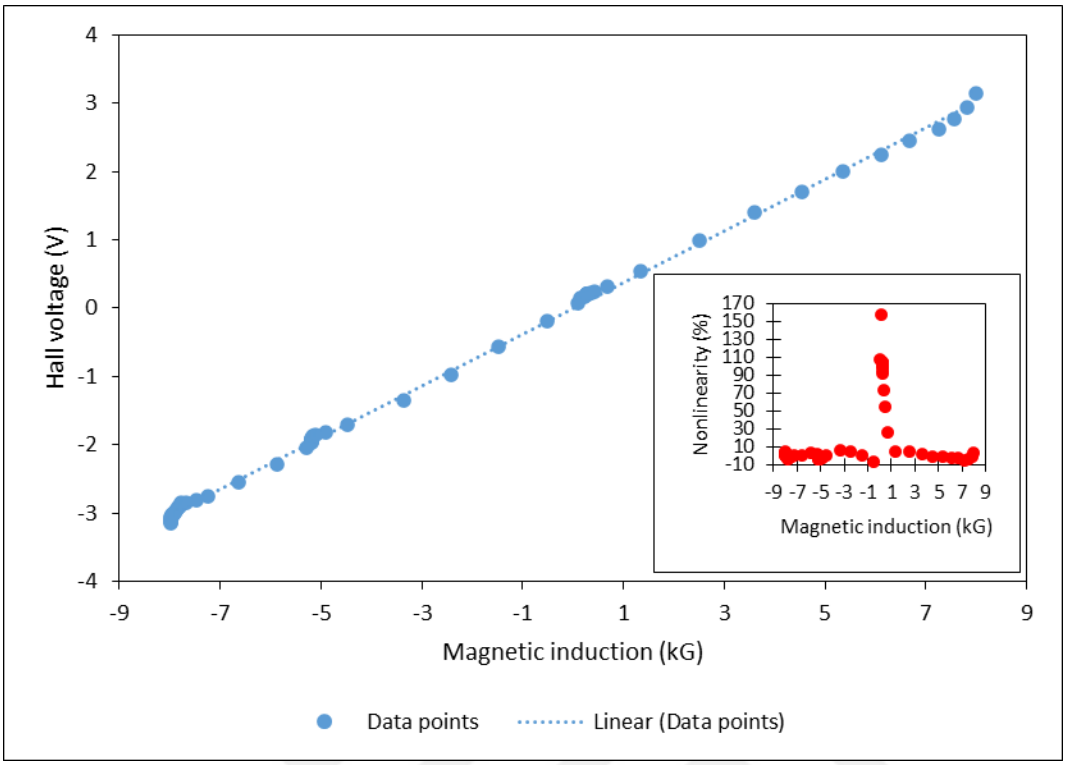

Figure 5.4. Plotted data obtained from the Hall-sensitivity measurement of one of the cross-shaped devices in Set 1, where the bias current I_C = 20 mA. Linear fit can be approximately represented by the equation V_H = (0.3807 mV/G) B with R^2 value of 0.9988. Dividing the slope of the equation, 0.3807 mV/G, by the bias current approximately gives the current-related Hall sensitivity of the device S_I = 190 Ω/T. Inset shows the non-linearity of the sensor response of the device, which was manufactured by transfer-printing graphene twice. (Equation 4.1 was used for the calculation of the non-linearity. Similar to the nonlinearity results presented in Figure 4.8, the device manifested very large nonlinearity for |Magnetic induction| < 1 kG, but |Nonlinearity| < 10% for |Magnetic induction| > 1 kG.

In addition to the current-related Hall sensitivity (S_I) with respect to the bias current (Figure 5.5), we also determined that the charge carrier type of all the devices in Set 1 were holes and calculated the sheet hole concentration p by checking the orientation of the orthogonal triplet formed by the bias current, magnetic field and

Hall electric field and applying the equation $n = (S_I\, e)^{-1}$, where n and e denote the charge carrier concentration and the elementary charge, respectively [2]. As a result, it turned out that there is an almost linear trend in the hole density with respect to the number of laminations (N) up to $N = 8$ (Figure 5.6). Furthermore, for Set 1, we determined the maximum current applicable for the device operation by increasing the bias current in increment of 0.1 mA between 0 and 1 mA, and 1.0 mA after reaching 1.0 mA. The maximum bias current could be of great importance for sensor applications. Change in the maximum current with respect to the number of laminations show two linear regimes up to $N = 8$, after which it vanishes (Figure 5.7). Beyond the maximum bias current, the device failed to operate properly.

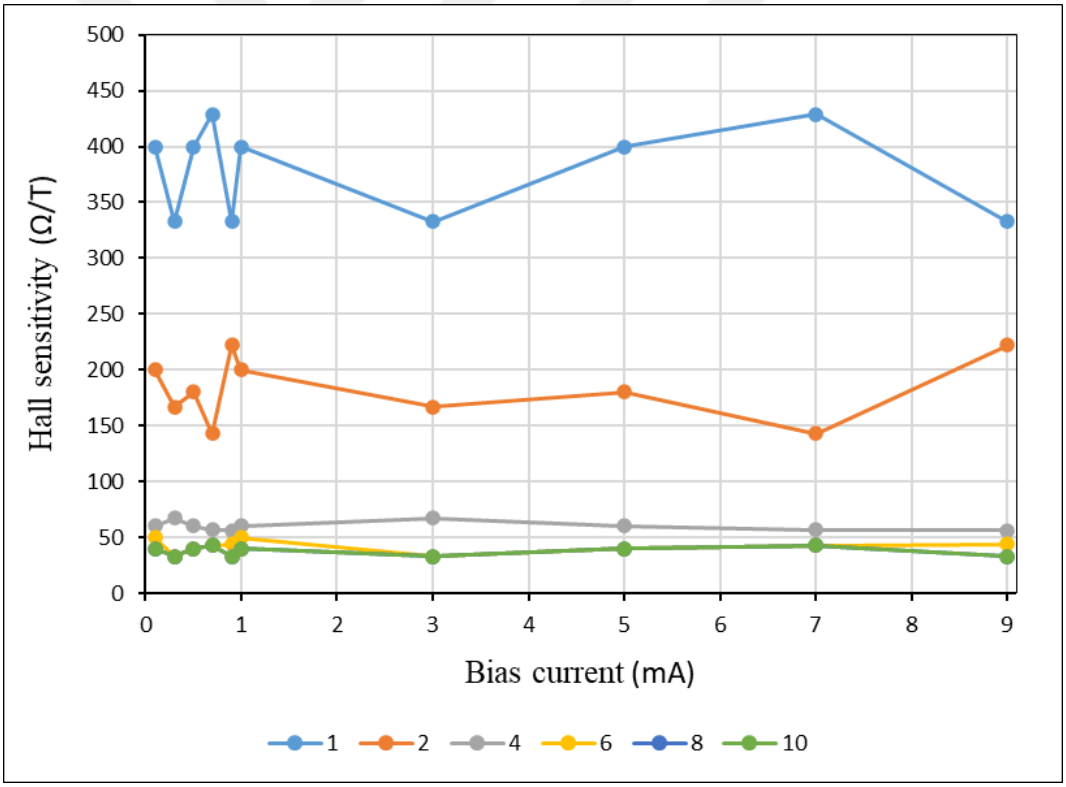

Figure 5.5. Plotted data extracted from the Hall-effect measurements of the devices in Set 1. The numbers in the legend below the graph represent the number of laminations done for making the devices. The Hall sensitivity was calculated for the bias currents of 0.1, 0.3, 0.5, 0.7, 0.9, 1.0, 3.0, 5.0, 7.0, 9.0 mA.

To obtain a more detailed electronic characterization of the thin films, van der Pauw and Hall-effect measurements of the devices in Set 2 and the square-shaped samples were performed by using NanoMagnetics Instruments ezHEMS, which is a tabletop HEMS equipped with a pair of permanent magnets creating a uniform magnetic field, with the intensity of ~5000 G, between their poles. After having been placed on the sample holder in ezHEMS head, the device was electrically connected to ezHEMS by using the copper probes of ezHEMS head and the copper contact pads of the sample (Figure 5.8).

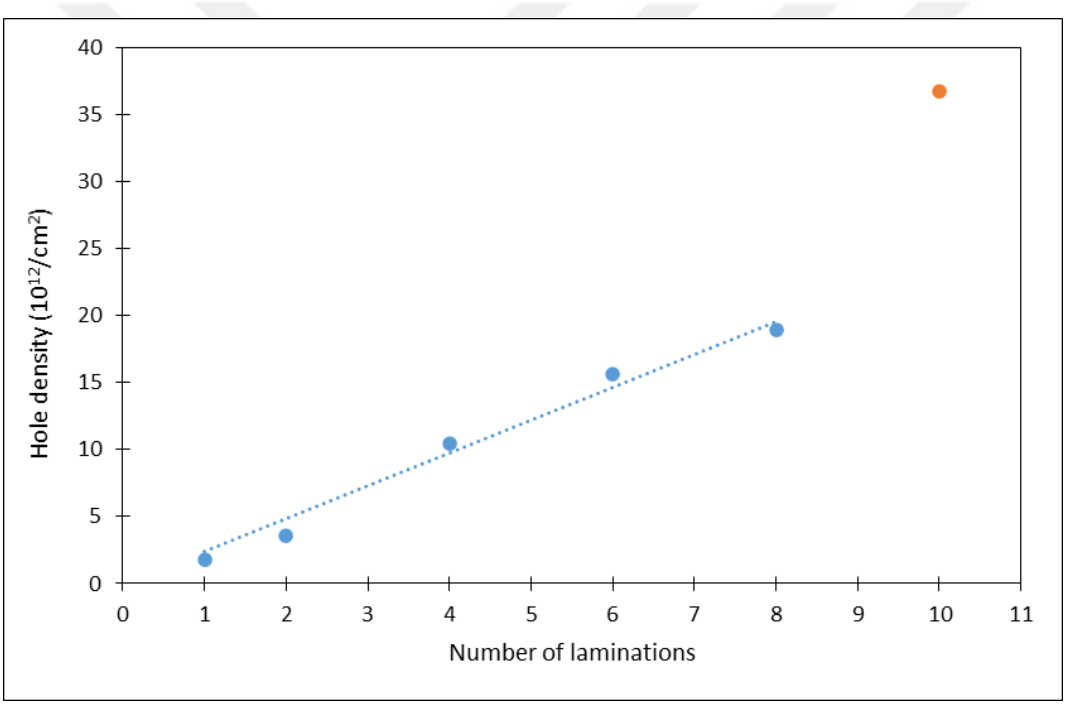

Figure 5.6. Plotted data produced by calculating hole density of each device in Set 1. Except for the (red) data point corresponding to N = 10, the (blue) data points could be well fitted with the line represented by the equation $p = (2.4\text{x}10^{12}\ \text{cm}^{-2})\ N$, with R^2 value of 0.9947, where p and N denote the hole density and the number of laminations.

Hall-sensitivities of the devices in Set 2 were obtained by measuring the Hall voltage V_H with respect to the bias current I_C after positioning the sample holder of ezHEMS between the poles of one of its magnets in order that the uniform magnetic field between the poles could be throughout perpendicular to the active surface of the device (Figure 5.8). The bias-current values were determined by symmetrically sweeping with constant step size of 0.1 mA and maximum absolute value of 0.5 mA. The measurement of the voltage V_S between the sense contacts contains off-set and noise voltages as additive terms; in order to subtract the off-set voltage from the result, first the measurements were carried out for both directions of magnetic field **B**, with the same set of bias currents. Then the subtraction of the offset voltage could be given by the operation V_S (+**B**) - V_S (-**B**) and thus $V_H = V_S$ (+**B**) - V_S (-**B**), where V_S (**B**) represents V_S measured for a bias current under the influence of the uniform magnetic field **B** [2]. Using this method, we collected data consisting of a set of (V_H, I_C) pairs, which can be well fitted with a line (Figure 5.9). The Hall sensitivity S_I can be found by dividing the slope of the line by the intensity of the uniform magnetic field between the poles and the sheet charge carrier density n is given by the equation $n = (S_I e)^{-1}$, where e represents the elementary charge [2]. As a result, we calculated the Hall sensitivity and charge carrier concentration with respect to the number of laminations (Figure 5.10).

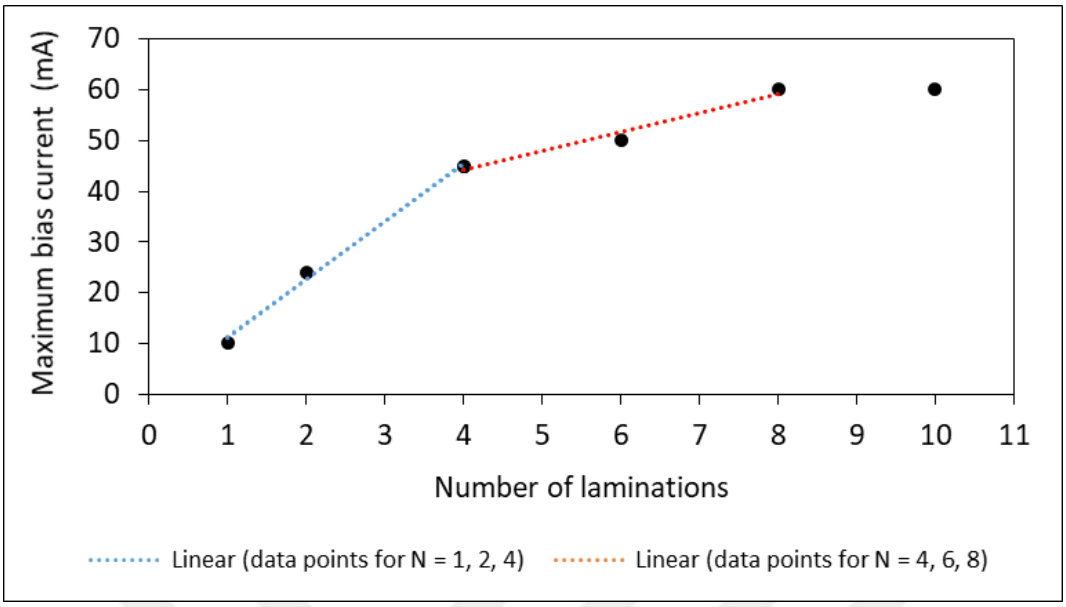

Figure 5.7. Variation of the maximum bias current (I_{max}) with respect to the number of laminations (N). Blue line and red line are linear fits representing two linear trends in the data, expressed by the equations I_{max} = (11.3 mA) N and [I_{max} = (3.8 N + 29.2) mA], with R^2 values 0.9986 and 0.9643, respectively. The former suggests that the maximum current density that the thin film could withstand remained constant up to N = 4.

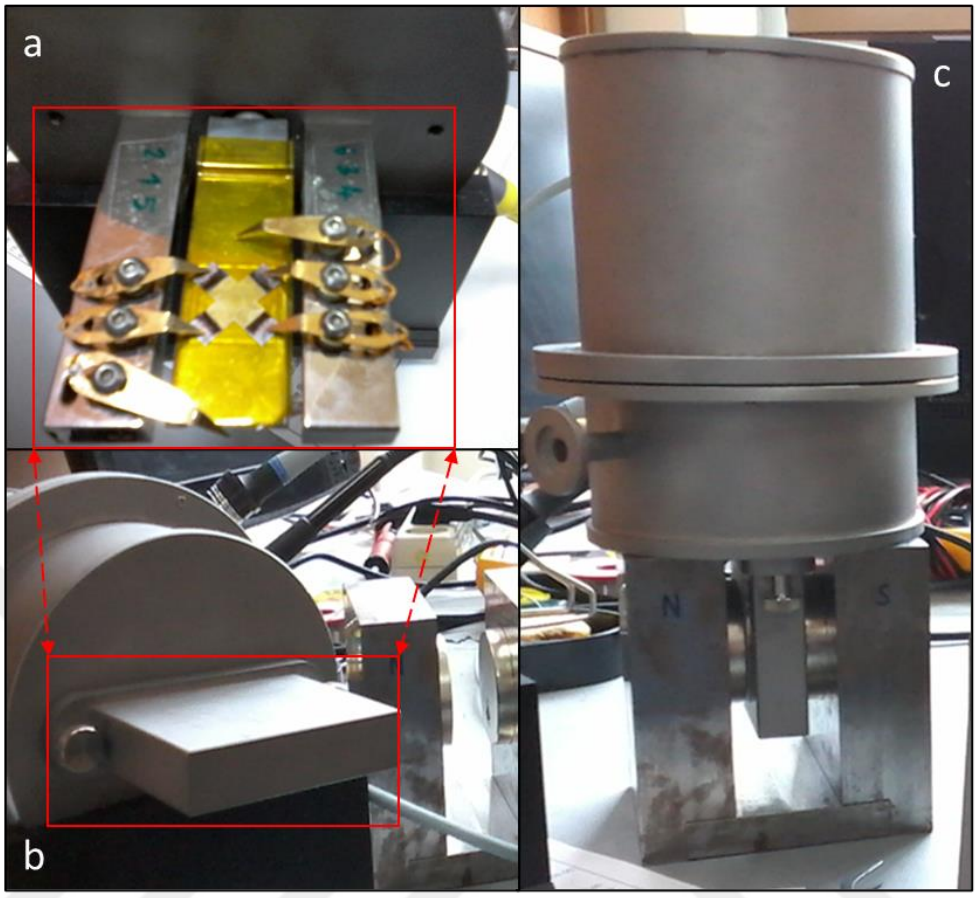

Figure 5.8. Setup for characterizing the devices in Set 2. (a) The sample holder of the ezHEMS loaded with one of the devices. Electrical connection was maintained by 4 of the 6 spring-loaded copper probes of the sample holder, which is a part of ezHEMS head. Each probe is associated with a number written above in green. 1&3 and 2&4 were selected as the current contacts and sense contacts, respectively. (b) The sample holder loaded with the device encased and ready for the Hall-effect measurement. (c) The sample holder inserted between the poles of the permanent magnet, where a uniform magnetic field with the intensity of 5300 G exists. In this configuration, V_{42} was measured with respect to I_{13}. To eliminate the offset voltage in the Hall voltage, we measured V_{42} for both directions of the magnetic field. To this end, after having completed the measurement for this orientation, we reversed the direction of the magnetic field relative to the sample holder by reinserting the ezHEMS head after rotating it by 180°.

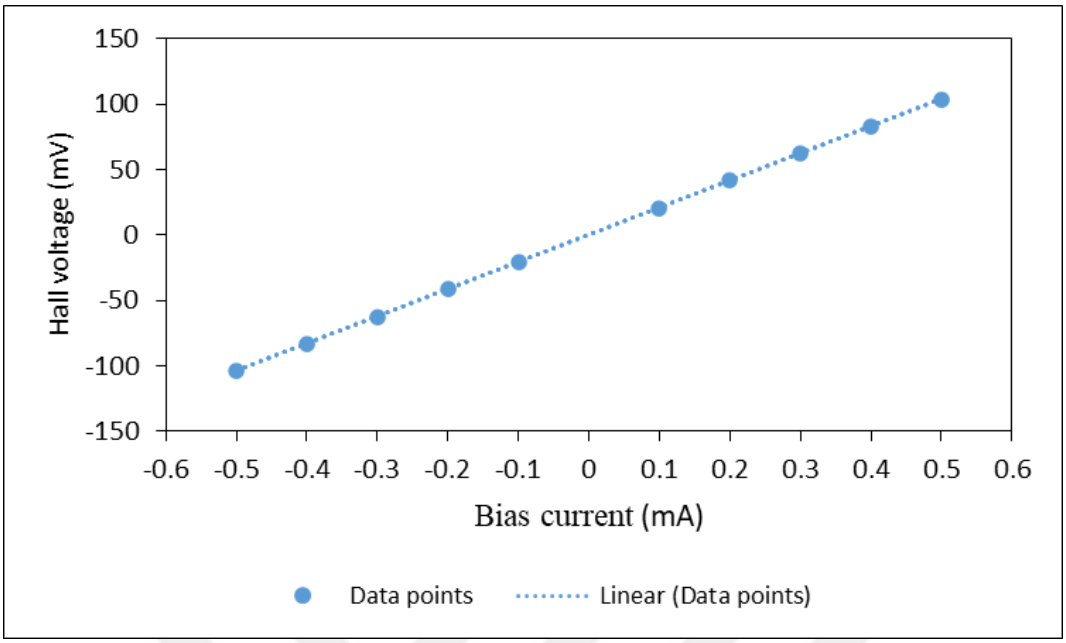

Figure 5.9. Plotted data resulted from the Hall-effect measurement of one of the devices in Set 2. The linear fit can be represented by the equation V_H = (207 Ω) I_C. Since the intensity of the uniform magnetic field used for the measurement is 5300 G (= 0.53 T), the Hall sensitivity of the device ≈ 391 Ω/T. The device was manufactured by transfer-printing graphene once.

The van der Pauw and Hall-effect measurements of the 4-contact square-shaped samples produced the mobility, charge carrier type, sheet charge carrier density, and sheet Hall coefficient values of the thin films for each number of laminations done for the manufacture (Figure 5.11).

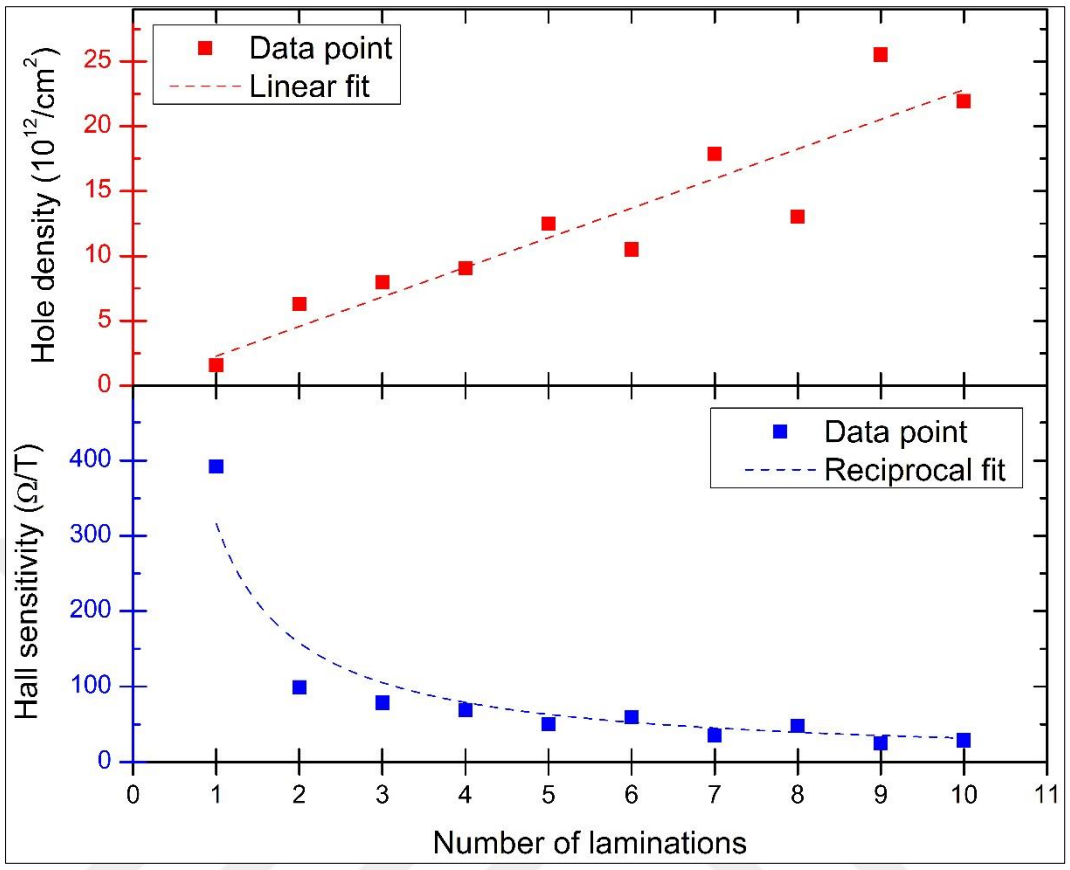

Figure 5.10. Dependence of the Hall sensitivity and the sheet hole concentration p on the number of layers N. The equation of the linear fit is $p = (2.28 \times 10^{12}\ \text{cm}^{-2})\ N$, with R^2 value 0.96.

The characterizations of the thin films by utilizing the cross-shaped devices and the square-shaped samples both revealed that the charge carriers were holes independent of the number of laminations and resulted in similar trends in the sheet Hall coefficient and hole density with respect to the number of laminations. Van der Pauw and Hall-effect measurements involving the square-shaped samples showed that the mobilities were around 1000 cm^2/(V·s) and showed no drastic change, whereas the hole density increased almost linearly with respect to the number of laminations. Consistently, the measurements yielded the sheet resistance and Hall-coefficient values almost inversely proportional to the number of laminations (Figure 5.11).

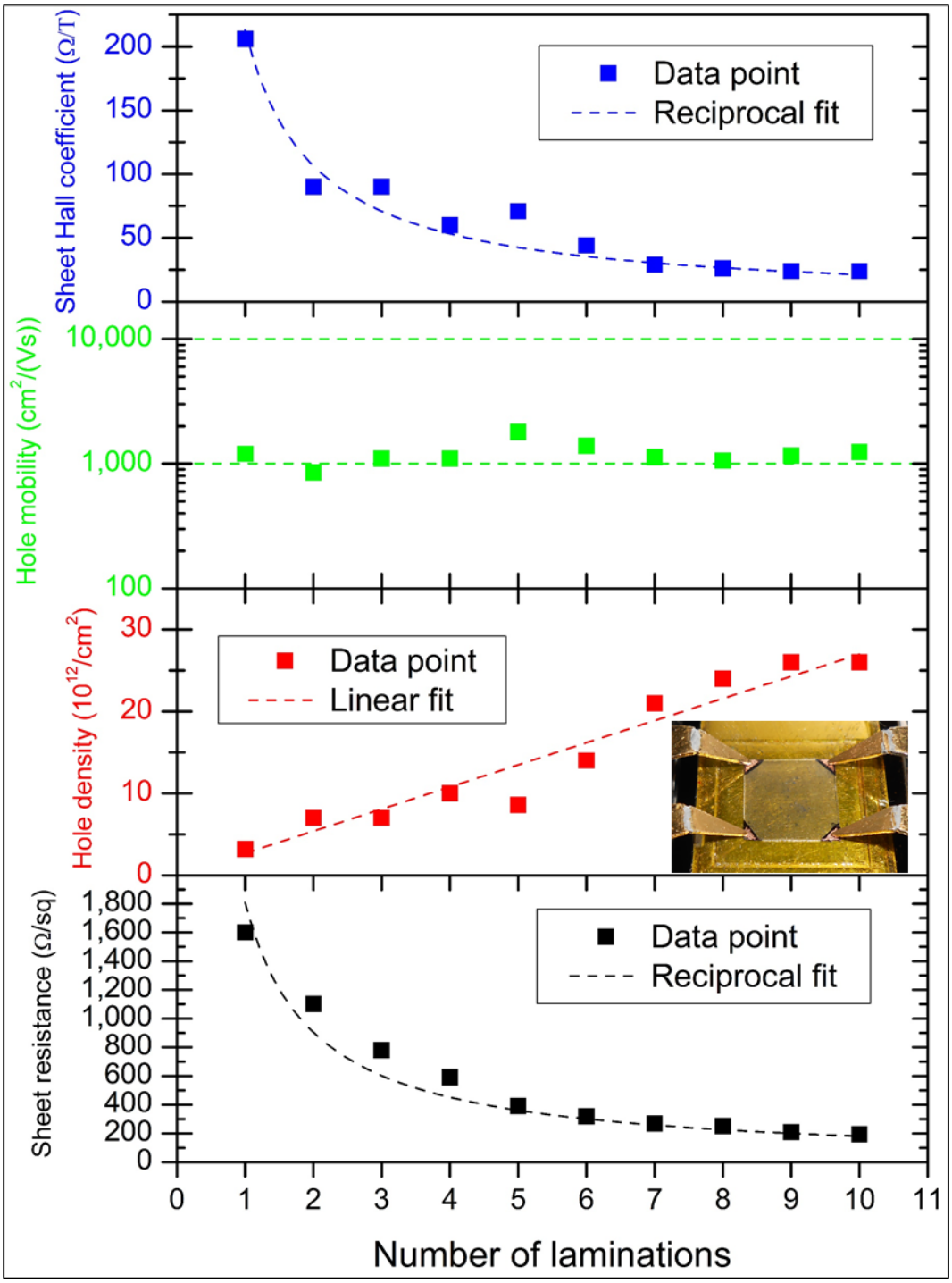

Figure 5.11. Electronic properties of the graphene-based thin films with respect to the number of laminations. Inset photo shows of one of the square-shaped van der Pauw samples used for the characterization of the thin films.

5.3 Resistors

Furthermore, by using the scheme depicted in Section 5.1, we manufactured resistors with the length and width of 1 and 0.5 cm (Figure 5.12 a) to estimate the maximum current densities that the thin films could withstand and assess the performance of the thin films as heaters, which could be utilized for fabricating graphene-based transparent defoggers.

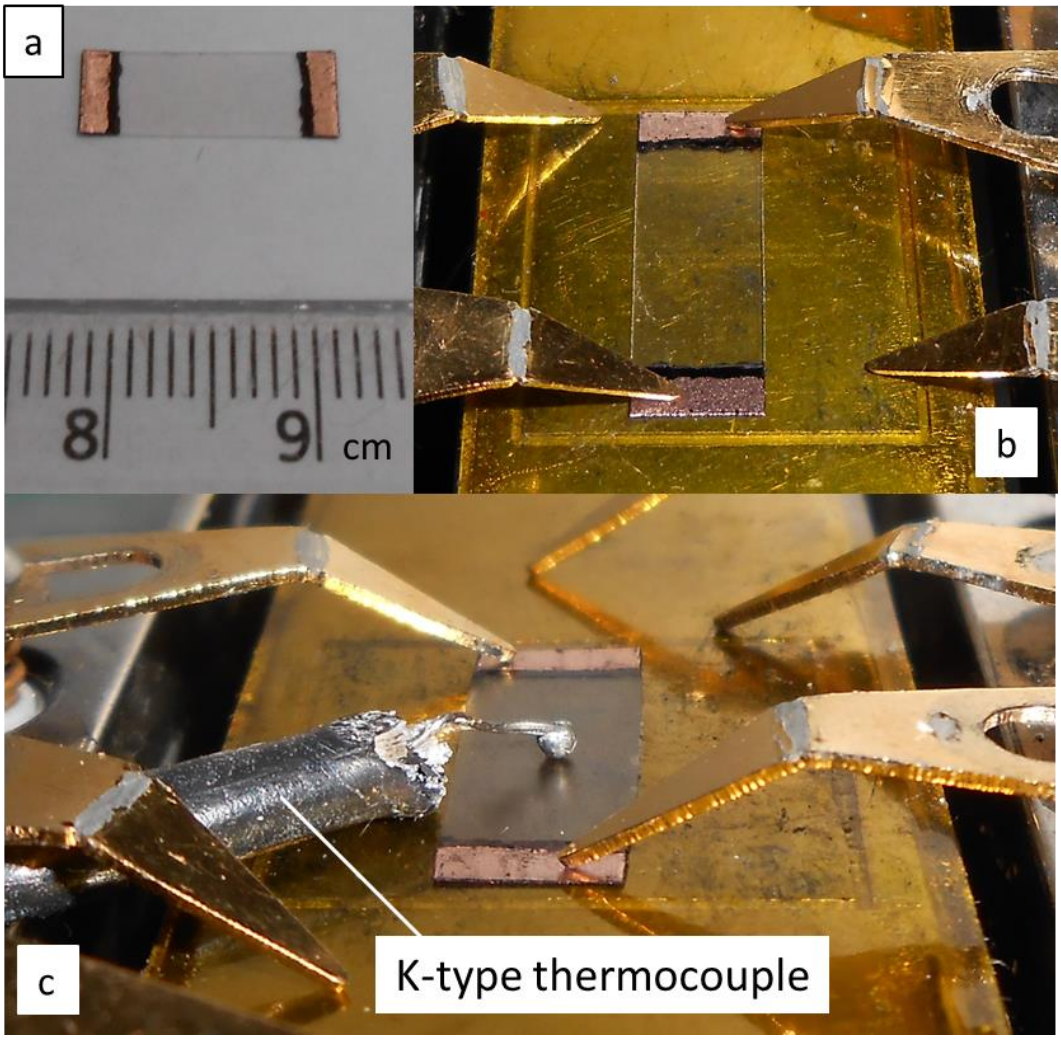

Figure 5.12. (a) A resistor manufactured by transfer-printing graphene once. (b) One of the resistors placed onto the sample holder of an ezHEMS head to test its current-carrying capacity. (c) Setup for joule heating measurements of the resistors.

The resistors were characterized by measuring the resistance, the maximum temperature at the surface of the thin film and the maximum current passing through the thin film at the maximum temperature before the electrical conductance ceased, for each number of laminations. The measurements were carried out by using ezHEMS head (Figure 5.12 b) connected to a source-meter and a K-type thermocouple in contact with the surface of the thin film (Figure 5.12 c).

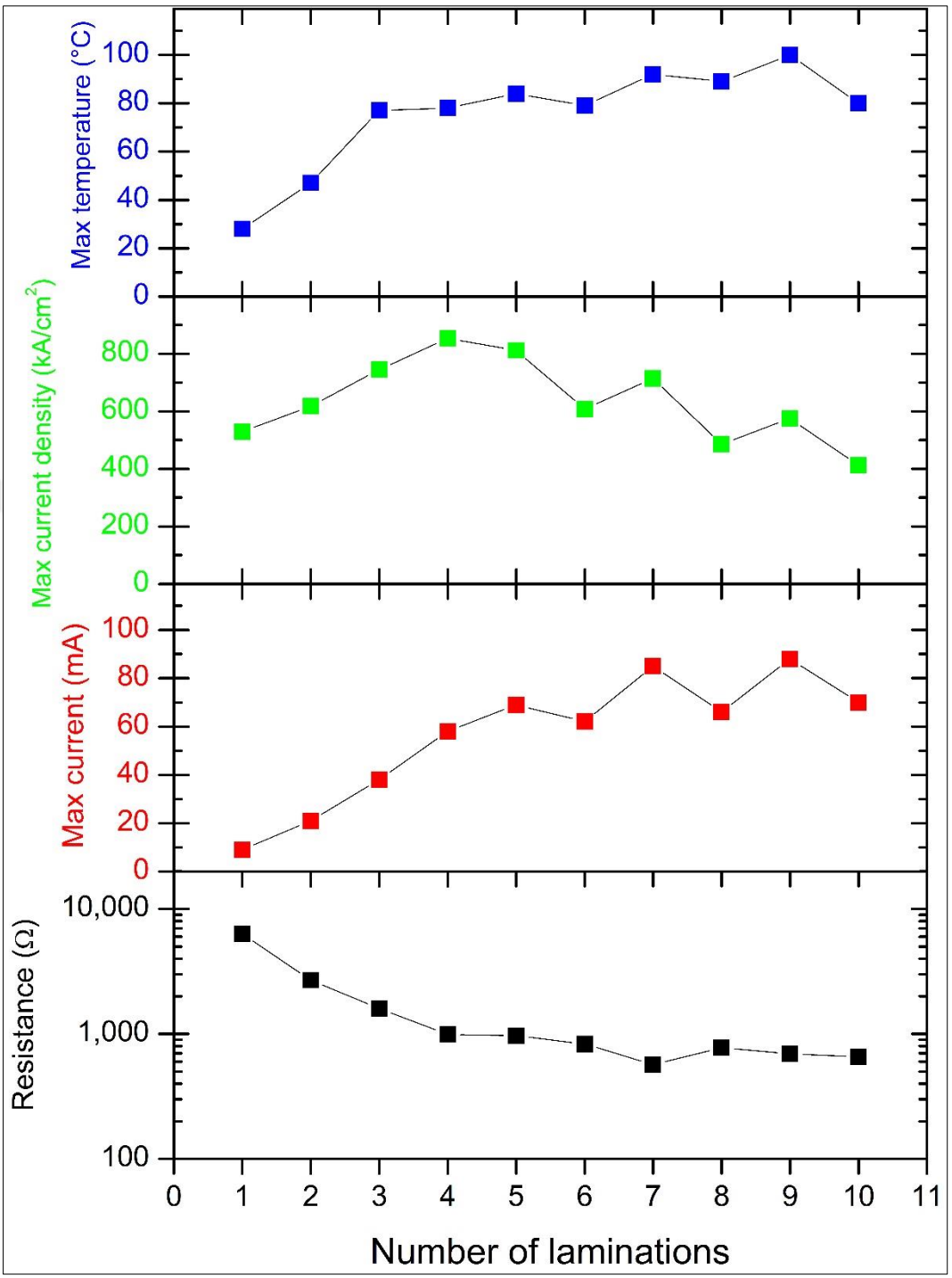

Figure 5.13. Change in the resistance, current-carrying and ohmic heating capacity of the resistors with respect to the number of laminations.

Table 5.1 Comparison of the resistance values of the resistors and the sheet resistance values of the graphene-based multilayered conductive films with respect to the number of laminations. Note that the reduction in the resistance is larger than that in the sheet resistance. This can be attributed to a large reduction in the contact resistance of the resistors.

Number of laminations	Resistance (Ω)	Sheet resistance (Ω/□)
1	6300	1600
2	2700	1100
3	1600	780
4	990	590
5	970	390
6	830	320
7	570	270
8	774	250
9	694	210
10	656	195

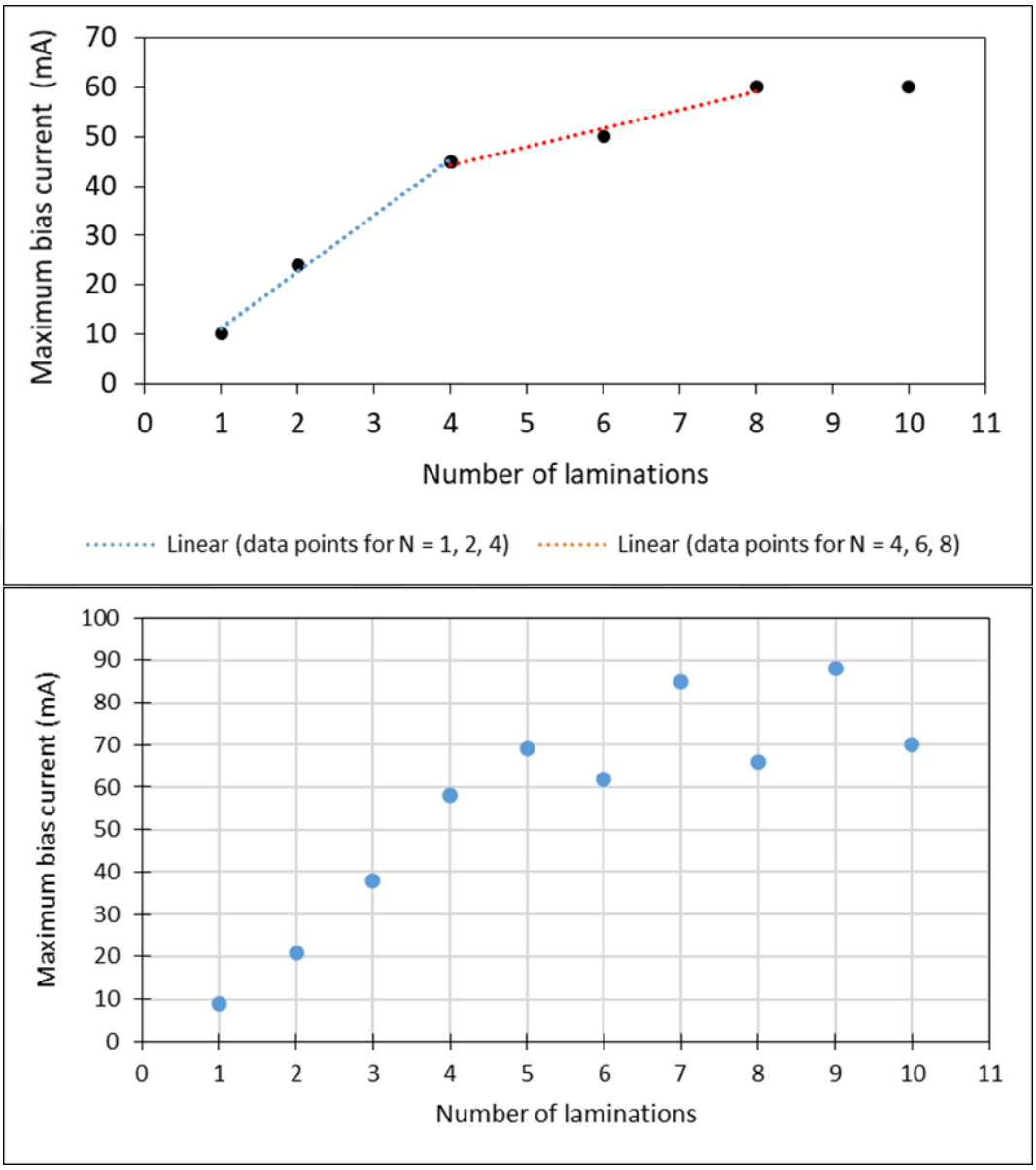

Figure 5.14. Comparison of maximum bias current for the cross-shaped Hall devices (top) and for the rectangular resistors (bottom). Inspite of the difference in geometry, their data show similar trends. As can be seen from Table 5.1, this can be attributed to the large reduction in the contact resistances of the devices up to N = 4.

CHAPTER 6

CONCLUSIONS

We conducted experiments for exploring the potential of graphene as a conductive film on flexible substrate. We synthesized graphene on 20μm-thick copper foil via atmospheric pressure chemical vapor deposition. Commercially-available EVA-coated PET (EVA/PET) lamination film was chosen as the flexible substrate. The graphene was directly transferred onto EVA/PET film via lamination at ~125°C, followed by the etching of the copper layer with aqueous ferric chloride [$FeCl_3$(aq)] solution and subsequent rinsing of the graphene-coated surface with deionized (DI) water. As a result, graphene/EVA/PET laminate was obtained.

By using the laminate, first we manufactured cross-shaped Hall devices by modifying the graphene transfer process so that the copper can be used as natural electrical contact pads. To this end, we painted the parts of the copper layer to be used as contact pads with permanent marker before the etching. Since the ink of the marker is water-proof and the copper etchant is $FeCl_3$(aq), it acted as an etch resist during the copper etching. By using this manufacture scheme, we manufactured two sets of cross-shaped Hall devices with different active areas: 28 large devices and 5 small devices. The devices have perfectly linear I-V curves and linear sensor responses except for small magnetic inductions, which can be attributed to the off-set voltage of the device. Average and standard deviation of the Hall sensitivities of the set of large devices are 586 and 224 Ω/T. The maximum Hall sensitivity is 1200 Ω/T. Small devices have the sensitivity values between 400 and 700 Ω/T, with average value 540 Ω/T.

By laminating a piece of graphene/EVA/PET laminate with a larger piece of graphene-carrying copper after having formed the stack graphene/copper/graphene/graphene/EVA/PET, we demonstrated that graphene-coated EVA layer is available for another transfer of graphene. By repeating this up

to ten times, we manufactured graphene-based multilayered conductive films on EVA/PET film. Also, cross-shaped Hall devices were made from these new laminates. In addition, we manufactured 1x1cm^2 square-shaped van der Pauw samples with copper contact pads at their corners. Hole density measurements performed by using both cross- and square-shaped devices show the same trend with respect to the number of laminations: hole density changed almost linearly with the number of laminations. Moreover, by using the square-shaped samples, we measured sheet resistance and mobility. There is no observable trend in mobility with respect to the number of layers. There are some fluctuations around 1000 cm^2/(Vs), but most of them are small. As a result, the sheet resistance is almost inversely proportional to the number of layers. Therefore, repeated layer-by-layer lamination yielded graphene-based multilayered conductive film on EVA/PET. Additionally, the surfaces of these films were characterized via atomic force microscopy in tapping mode. Scan areas were 2x2, 5x5, and 10x10 μm^2. AFM images shows that the RMS roughness of the surface appears to converge a value below 50 nm as the number of layers increases.

Finally, we studied the Joule heating in these graphene-based films by manufacturing rectangular resistors. Their surface temperature were measured by using a K-type thermocouple. Maximum current is the largest current that the device can carry before its conductance ceases and maximum temperature is the temperature measured when the device carries maximum current. Maximum current increases almost linearly with the number of laminations N up to N = 4. At that point the slope remarkably changed. Comparison between the change of the sheet resistance and the resistance of the resistor indicates a large decrease in the contact resistance up to 4, which can explain the observation.

In conclusion, CVD-graphene can be used to make Hall devices with sensitivities up to 1200 Ω/T on flexible substrate, by using a facile manufacturing scheme. Furthermore, by applying repeated layer-by-layer transfer onto the flexible substrate, it is possible to form a multilayered conductive film with mobility of ~1000 cm^2/(Vs). Nevertheless, it is evident that there is room for improvement. First,

lamination can be optimized to minimize the damage possibly caused by the pressure exerted by the rollers. Also, enhancement in graphene quality must be taken into consideration. The precision of the manufacturing process is another important issue: by increasing the precision of the manufacture, variation in the device properties and the off-set voltage can be minimized.

REFERENCES

1. Novoselov, K. S. *et al.* Electric field in atomically thin carbon films. *Science (80-.).* **306**, 666–669 (2004).
2. Popovic, R. S. *Hall Effect Devices: Magnetic Sensors and Characterization of Semiconductors*. (CRC Press, 1991).
3. Lee, C., Wei, X., Kysar, J. W. & Hone, J. Measurement of the elastic properties and intrinsic strength of monolayer graphene. *Science (80-.).* **321**, 385–388 (2008).
4. Ramsden, E. *Hall-Effect Sensors*. *Hall-Effect Sensors* (Elsevier Inc., 2006). doi:10.1016/B978-0-7506-7934-3.X5000-5.
5. Bando, M. *et al.* High sensitivity and multifunctional micro-Hall sensors fabricated using InAlSb/InAsSb/InAlSb heterostructures. *J. Appl. Phys.* **105**, 07E909 (2009).
6. Hall, E. H. On a New Action of the Magnet on Electric Currents. *Am. J. Math.* **2**, 287–292 (1879).
7. Hall, E. H. On the new action of magnetism on a permanent electric current. *Am. J. Sci.* **s3-20**, 161 LP – 186 (1880).
8. *Springer Handbook of Materials Measurement Methods*. *Springer Handbook of Materials Measurement Methods* (Springer Berlin Heidelberg, 2006). doi:10.1007/978-3-540-30300-8.
9. Warner, J. H., Schäffel, F., Bachmatiuk, A. & Rümmeli, M. H. Properties of Graphene. in *Graphene* 61–127 (Elsevier, 2013). doi:10.1016/b978-0-12-394593-8.00003-5.
10. Wallace, P. R. The band theory of graphite. *Phys. Rev.* **71**, 622–634 (1947).
11. Bolotin, K. I. *et al.* Ultrahigh electron mobility in suspended graphene. *Solid*

State Commun. **146**, 351–355 (2008).

12. Novoselov, K. S. *et al.* Two-dimensional gas of massless Dirac fermions in graphene. *Nature* **438**, 197–200 (2005).

13. Castro Neto, A. H., Guinea, F., Peres, N. M. R., Novoselov, K. S. & Geim, A. K. The electronic properties of graphene. *Rev. Mod. Phys.* **81**, 109–162 (2009).

14. Androulidakis, C., Koukaras, E. N., Pastore Carbone, M. G., Hadjinicolaou, M. & Galiotis, C. Wrinkling formation in simply-supported graphenes under tension and compression loadings. *Nanoscale* **9**, 18180–18188 (2017).

15. Balandin, A. A. *et al.* Superior thermal conductivity of single-layer graphene. *Nano Lett.* **8**, 902–907 (2008).

16. Novoselov, K. S. *et al.* Two-dimensional gas of massless Dirac fermions in graphene. *Nature* **438**, 197–200 (2005).

17. Morozov, S. V. *et al.* Giant intrinsic carrier mobilities in graphene and its bilayer. *Phys. Rev. Lett.* **100**, 016602 (2008).

18. Balandin, A. A. *et al.* Superior thermal conductivity of single-layer graphene. *Nano Lett.* **8**, 902–907 (2008).

19. Chen, J. H., Jang, C., Xiao, S., Ishigami, M. & Fuhrer, M. S. Intrinsic and extrinsic performance limits of graphene devices on SiO 2. *Nat. Nanotechnol.* **3**, 206–209 (2008).

20. Lee, C., Wei, X., Kysar, J. W. & Hone, J. Measurement of the elastic properties and intrinsic strength of monolayer graphene. *Science (80-.).* **321**, 385–388 (2008).

21. Kumar, N. *et al.* Top-down synthesis of graphene: A comprehensive review. *FlatChem* vol. 27 100224 (2021).

22. Huang, H., Chen, S., Wee, A. T. S. & Chen, W. Epitaxial growth of

graphene on silicon carbide (SiC). in *Graphene: Properties, Preparation, Characterisation and Devices* 3–26 (Woodhead Publishing, 2014). doi:10.1533/9780857099334.1.3.

23. Li, X. *et al.* Large-area synthesis of high-quality and uniform graphene films on copper foils. *Science (80-.).* **324**, 1312–1314 (2009).

24. Edwards, R. S. & Coleman, K. S. Graphene film growth on polycrystalline metals. *Acc. Chem. Res.* **46**, 23–30 (2013).

25. Guermoune, A. *et al.* Chemical vapor deposition synthesis of graphene on copper with methanol, ethanol, and propanol precursors. *Carbon N. Y.* **49**, 4204–4210 (2011).

26. Li, X., Cai, W., Colombo, L. & Ruoff, R. S. Evolution of graphene growth on Ni and Cu by carbon isotope labeling. *Nano Lett.* **9**, 4268–4272 (2009).

27. Huang, L. *et al.* Synthesis of high-quality graphene films on nickel foils by rapid thermal chemical vapor deposition. *Carbon N. Y.* **50**, 551–556 (2012).

28. Mogera, U., Kurra, N., Radhakrishnan, D., Narayana, C. & Kulkarni, G. U. Low cost, rapid synthesis of graphene on Ni: An efficient barrier for corrosion and thermal oxidation. *Carbon N. Y.* **78**, 384–391 (2014).

29. Tu, R. *et al.* Fast synthesis of high-quality large-area graphene by laser CVD. *Appl. Surf. Sci.* **445**, 204–210 (2018).

30. Seifert, M., Drieschner, S., Blaschke, B. M., Hess, L. H. & Garrido, J. A. Induction heating-assisted repeated growth and electrochemical transfer of graphene on millimeter-thick metal substrates. *Diam. Relat. Mater.* **47**, 46–52 (2014).

31. Riikonen, J. *et al.* Photo-thermal chemical vapor deposition of graphene on copper. *Carbon N. Y.* **62**, 43–50 (2013).

32. Reckinger, N., Felten, A., Santos, C. N., Hackens, B. & Colomer, J. F. The

influence of residual oxidizing impurities on the synthesis of graphene by atmospheric pressure chemical vapor deposition. *Carbon N. Y.* **63**, 84–91 (2013).

33. Li, C., Zhang, P., Wang, J., Boscoboinik, J. A. & Zhou, G. Tuning the Deoxygenation of Bulk-Dissolved Oxygen in Copper. *J. Phys. Chem. C* **122**, 8254–8261 (2018).

34. Taira, T., Obata, S. & Saiki, K. Nucleation site in CVD graphene growth investigated by radiation-mode optical microscopy. *Appl. Phys. Express* **10**, 055502 (2017).

35. Zeng, M. *et al.* Liquid metal: An innovative solution to uniform graphene films. *Chem. Mater.* **26**, 3637–3643 (2014).

36. Ishihara, M., Koga, Y., Kim, J., Tsugawa, K. & Hasegawa, M. Direct evidence of advantage of Cu(111) for graphene synthesis by using Raman mapping and electron backscatter diffraction. *Mater. Lett.* **65**, 2864–2867 (2011).

37. Mi, X., Meunier, V., Koratkar, N. & Shi, Y. Facet-insensitive graphene growth on copper. *Phys. Rev. B - Condens. Matter Mater. Phys.* **85**, 155436 (2012).

38. Wang, Y. *et al.* Chemical Vapor Deposition Growth of Graphene Domains Across the Cu Grain Boundaries. *Nano* **13**, (2018).

39. Dong, J., Zhang, L., Zhang, K. & Ding, F. How graphene crosses a grain boundary on the catalyst surface during chemical vapour deposition growth. *Nanoscale* **10**, 6878–6883 (2018).

40. Wu, T. *et al.* Fast growth of inch-sized single-crystalline graphene from a controlled single nucleus on Cu-Ni alloys. *Nat. Mater.* **15**, 43–47 (2016).

41. Vlassiouk, I. V. *et al.* Evolutionary selection growth of two-dimensional materials on polycrystalline substrates. *Nat. Mater.* **17**, 318–322 (2018).

42. Xu, X. *et al.* Ultrafast epitaxial growth of metre-sized single-crystal graphene on industrial Cu foil. *Sci. Bull.* **62**, 1074–1080 (2017).

43. Pakhnevich, A. A., Golod, S. V & Prinz, V. Y. Surface melting of copper during graphene growth by chemical vapour deposition. *J. Phys. D. Appl. Phys.* **48**, 435303 (2015).

44. Baek, J., Kim, J., Kim, J., Shin, B. & Jeon, S. Growth of graphene on non-catalytic substrate by controlling the vapor pressure of catalytic nickel. *Carbon N. Y.* **143**, 294–299 (2019).

45. Pang, J. *et al.* Self-Terminating Confinement Approach for Large-Area Uniform Monolayer Graphene Directly over Si/SiOx by Chemical Vapor Deposition. *ACS Nano* **11**, 1946–1956 (2017).

46. Zhang, C. *et al.* Facile synthesis of graphene on dielectric surfaces using a two-temperature reactor CVD system. *Nanotechnology* **24**, 395603 (2013).

47. Baek, J., Lee, M., Kim, J., Lee, J. & Jeon, S. Transfer-free growth of polymer-derived graphene on dielectric substrate from mobile hot-wire-assisted dual heating system. *Carbon N. Y.* **127**, 41–46 (2018).

48. Liu, B. *et al.* Oxygen-assisted direct growth of large-domain and high-quality graphene on glass targeting advanced optical filter applications. *Nano Res.* **14**, 260–267 (2021).

49. Mishra, N. *et al.* Wafer-Scale Synthesis of Graphene on Sapphire: Toward Fab-Compatible Graphene. *Small* **15**, 1904906 (2019).

50. Wei, D. *et al.* Critical Crystal Growth of Graphene on Dielectric Substrates at Low Temperature for Electronic Devices. *Angew. Chemie* **125**, 14371–14376 (2013).

51. Banszerus, L. *et al.* Ballistic Transport Exceeding 28 μm in CVD Grown Graphene. *Nano Lett.* **16**, 1387–1391 (2016).

52. Xu, J. *et al.* Enhancing the Strength of Graphene by a Denser Grain Boundary. *ACS Nano* **12**, 4529–4535 (2018).

53. Cai, W. *et al.* Thermal transport in suspended and supported monolayer graphene grown by chemical vapor deposition. *Nano Lett.* **10**, 1645–1651 (2010).

54. Li, X. *et al.* Transfer of large-area graphene films for high-performance transparent conductive electrodes. *Nano Lett.* **9**, 4359–4363 (2009).

55. Lee, J., Lee, S. & Yu, H. K. Contamination-free graphene transfer from Cu-foil and cu-thin-film/sapphire. *Coatings* **7**, 218 (2017).

56. Leong, W. S. *et al.* Paraffin-enabled graphene transfer. *Nat. Commun.* **10**, 1–8 (2019).

57. Qi, P. *et al.* Wax-assisted crack-free transfer of monolayer CVD graphene: Extending from standalone to supported copper substrates. *Appl. Surf. Sci.* **493**, 81–86 (2019).

58. Grebel, H. *et al.* Transfer of graphene with protective oxide layers. *ChemEngineering* **2**, 1–11 (2018).

59. Lee, J. *et al.* Clean transfer of graphene and its effect on contact resistance. *Appl. Phys. Lett.* **103**, 103104 (2013).

60. Choi, J. *et al.* Enhanced performance of graphene by using gold film for transfer and masking process. *Curr. Appl. Phys.* **14**, 1045–1050 (2014).

61. Kang, J. *et al.* Efficient transfer of large-area graphene films onto rigid substrates by hot pressing. *ACS Nano* **6**, 5360–5365 (2012).

62. Kim, M., Li, C., Susoma, J., Riikonen, J. & Lipsanen, H. Versatile Water-Based Transfer of Large-Area Graphene Films onto Flexible Substrates. in *MRS Advances* vol. 2 3749–3754 (Springer, 2017).

63. Marchena, M. *et al.* Dry transfer of graphene to dielectrics and flexible

substrates using polyimide as a transparent and stable intermediate layer. *2D Mater*. **5**, 035022 (2018).

64. Martins, L. G. P. *et al.* Direct transfer of graphene onto flexible substrates. *Proc. Natl. Acad. Sci. U. S. A.* **110**, 17762–17767 (2013).

65. Timofeev, V. B., Popov, V. I., Nikolaev, D. V., Timofeeva, T. E. & Smagulova, S. A. Preparation of transparent conducting films from CVD graphene by lamination and their characterization. *Nanotechnologies Russ.* **12**, 62–65 (2017).

66. Guo, C., Kong, X. & Ji, H. Hot-Roll-Pressing Mediated Transfer of Chemical Vapor Deposition Graphene for Transparent and Flexible Touch Screen with Low Sheet-Resistance. *J. Nanosci. Nanotechnol.* **18**, 4337–4342 (2017).

67. Du, F., Duan, H. L., Xiong, C. Y. & Wang, J. X. Substrate wettability requirement for the direct transfer of graphene. *Appl. Phys. Lett.* **107**, 143109 (2015).

68. Campos, N., Perez-Mas, A. M., Alvarez, P., Menéndez, R. & Gómez, D. Surface treatment of polyimide substrates for the transfer and multitransfer of graphene films. *Appl. Surf. Sci.* **349**, 101–107 (2015).

69. Wang, B. *et al.* Support-free transfer of ultrasmooth graphene films facilitated by self-Assembled monolayers for electronic devices and patterns. *ACS Nano* **10**, 1404–1410 (2016).

70. Lin, W. H. *et al.* A direct and polymer-free method for transferring graphene grown by chemical vapor deposition to any substrate. *ACS Nano* **8**, 1784–1791 (2014).

71. Wang, M., Yang, E. H., Vajtai, R., Kono, J. & Ajayan, P. M. Effects of etchants in the transfer of chemical vapor deposited graphene. *J. Appl. Phys.* **123**, 195103 (2018).

72. Sun, D., Wang, W. & Liu, Z. Establishment of a reliable transfer process for fabricating chemical vapor deposition-grown graphene films with advanced and repeatable electrical properties. *RSC Adv.* **8**, 19846–19851 (2018).

73. Wang, Y. *et al.* Electrochemical delamination of CVD-grown graphene film: Toward the recyclable use of copper catalyst. *ACS Nano* **5**, 9927–9933 (2011).

74. Wang, X. *et al.* Direct delamination of graphene for high-performance plastic electronics. *Small* **10**, 694–698 (2014).

75. Gupta, P. *et al.* A facile process for soak-and-peel delamination of CVD graphene from substrates using water. *Sci. Rep.* **4**, 1–6 (2014).

76. Ishigami, M., Chen, J. H., Cullen, W. G., Fuhrer, M. S. & Williams, E. D. Atomic structure of graphene on SiO 2. *Nano Lett.* **7**, 1643–1648 (2007).

77. Huang, P. Y. *et al.* Grains and grain boundaries in single-layer graphene atomic patchwork quilts. *Nature* **469**, 389–392 (2011).

78. Lim, Y. J. *et al.* Monitoring defects on monolayer graphene using nematic liquid crystals. *Opt. Express* **23**, 14162 (2015).

79. Sempere, B., Herrero, J., Bermúdez, J., Agea, B. & Colominas, C. Statistically meaningful grain size analysis of CVD graphene based on the photocatalytic oxidation of copper. *Graphene Technol.* **2**, 13–20 (2017).

80. Lee, J. Y. *et al.* Direct observation of grain boundaries in chemical vapor deposited graphene. *Carbon N. Y.* **115**, 147–153 (2017).

81. Fan, X. *et al.* Direct observation of grain boundaries in graphene through vapor hydrofluoric acid (VHF) exposure. *Sci. Adv.* **4**, (2018).

82. Ferrari, A. C. *et al.* Raman spectrum of graphene and graphene layers. *Phys. Rev. Lett.* **97**, 187401 (2006).

83. Yoon, D. *et al.* Variations in the Raman spectrum as a function of the

number of graphene layers. *J. Korean Phys. Soc.* **55**, 1299–1303 (2009).

84. Casiraghi, C., Pisana, S., Novoselov, K. S., Geim, A. K. & Ferrari, A. C. Raman fingerprint of charged impurities in graphene. *Appl. Phys. Lett.* **91**, 233108 (2007).

85. Das, A. *et al.* Monitoring dopants by Raman scattering in an electrochemically top-gated graphene transistor. *Nat. Nanotechnol.* **3**, 210–215 (2008).

86. Kalbac, M. *et al.* The influence of strong electron and hole doping on the Raman intensity of chemical vapor-deposition graphene. *ACS Nano* **4**, 6055–6063 (2010).

87. Sul, O. *et al.* Reduction of hole doping of chemical vapor deposition grown graphene by photoresist selection and thermal treatment. *Nanotechnology* **27**, 505205 (2016).

88. Piazza, A. *et al.* Substrate and atmosphere influence on oxygen p-doped graphene. *Carbon N. Y.* **107**, 696–704 (2016).

89. Lee, T., Mas'Ud, F. A., Kim, M. J. & Rho, H. Spatially resolved Raman spectroscopy of defects, strains, and strain fluctuations in domain structures of monolayer graphene. *Sci. Rep.* **7**, 1–8 (2017).

90. Ferrari, A. C. & Basko, D. M. Raman spectroscopy as a versatile tool for studying the properties of graphene. *Nature Nanotechnology* vol. 8 235–246 (2013).

91. Lin, H. *et al.* Contactless graphene conductivity mapping on a wide range of substrates with terahertz time-domain reflection spectroscopy. *Sci. Rep.* **7**, 1–9 (2017).

92. Whelan, P. R. *et al.* Conductivity mapping of graphene on polymeric films by terahertz time-domain spectroscopy. *Opt. Express* **26**, 17748 (2018).

93. Li, Z. *et al.* Copper substrate as a catalyst for the oxidation of chemical vapor deposition-grown graphene. *J. Solid State Chem.* **224**, 14–20 (2015).

94. Polat, E. O. & Kocabas, C. Broadband optical modulators based on graphene supercapacitors. *Nano Lett.* **13**, 5851–5857 (2013).

95. Tang, C. C., Li, M. Y., Li, L. J., Chi, C. C. & Chen, J. C. Characteristics of a sensitive micro-Hall probe fabricated on chemical vapor deposited graphene over the temperature range from liquid-helium to room temperature. *Appl. Phys. Lett.* **99**, 112107 (2011).

96. Sonusen, S., Karci, O., Dede, M., Aksoy, S. & Oral, A. Single layer graphene Hall sensors for scanning Hall probe microscopy (SHPM) in 3-300 K temperature range. *Appl. Surf. Sci.* **308**, 414–418 (2014).

97. Chen, B. *et al.* Exploration of sensitivity limit for graphene magnetic sensors. *Carbon N. Y.* **94**, 585–589 (2015).

98. Panchal, V. *et al.* Small epitaxial graphene devices for magnetosensing applications. in *Journal of Applied Physics* vol. 111 07E509 (American Institute of PhysicsAIP, 2012).

99. Xu, H. *et al.* Batch-fabricated high-performance graphene Hall elements. *Sci. Rep.* **3**, 1–8 (2013).

100. Huang, L. *et al.* Ultra-sensitive graphene Hall elements. *Appl. Phys. Lett.* **104**, 183106 (2014).

101. Alexandrou, K., Petrone, N., Hone, J. & Kymissis, I. Encapsulated graphene field-effect transistors for air stable operation. *Appl. Phys. Lett.* **106**, 113104 (2015).

102. Heller, I. *et al.* Charge noise in graphene transistors. *Nano Lett.* **10**, 1563–1567 (2010).

103. Kochat, V. *et al.* Origin of 1/f noise in graphene produced for largescale

applications in electronics. *IET Circuits, Devices Syst.* **9**, 52–58 (2015).

104. Dauber, J. *et al.* Ultra-sensitive Hall sensors based on graphene encapsulated in hexagonal boron nitride. *Appl. Phys. Lett.* **106**, 193501 (2015).

105. Loan, P. T. K. *et al.* Hall effect biosensors with ultraclean graphene film for improved sensitivity of label-free DNA detection. *Biosens. Bioelectron.* **99**, 85–91 (2018).

106. Liu, X. *et al.* Highly sensitive and selective potassium ion detection based on graphene hall effect biosensors. *Materials (Basel).* **11**, 399 (2018).

107. Lee, C., Wei, X., Kysar, J. W. & Hone, J. Measurement of the elastic properties and intrinsic strength of monolayer graphene. *Science (80-.).* **321**, 385–388 (2008).

108. Qing, F., Shen, C., Jia, R., Zhan, L. & Li, X. Catalytic substrates for graphene growth. *MRS Bull.* **42**, 819–824 (2017).

109. Edwards, R. S. & Coleman, K. S. Graphene film growth on polycrystalline metals. *Acc. Chem. Res.* **46**, 23–30 (2013).